Modelling the Effects and Responses of DNA Damage Response Inhibitor Drugs

Swansea University
Prifysgol Abertawe

Kira Pugh

Submitted in fulfilment of the requirements

for the Degree of Doctor of Philosophy

Department of Mathematics

Faculty of Science and Engineering

Swansea University

2024

"Live as if you were to die tomorrow. Learn as if you were to live forever." — Mahatma Gandhi

Abstract

The increasing complexity of clinical and biological effects of multimodality therapies often results in substantial challenges to the clinical and preclinical development of novel therapeutic drugs. Mathematical modelling that is informed by experimental data can aid in understanding and studying the multiple (nonlinear) therapeutic effects and responses of these drugs, which can assist in the preclinical design and development, and its clinical implementation. The multiscale complexity of cancer necessitates the adoption of a multiscale approach, incorporating appropriate mechanisms to obtain meaningful and predictive mathematical models to study the therapeutic effects and outcomes.

DNA damage occurs thousands of times per cell per day. The DNA damage response (DDR) is responsible for detecting and repairing DNA damage. The DDR pathways can be exploited for anti-cancer treatments. DDR inhibitor drugs can be used to cause certain pathways to stop working, which enhances cancer growth inhibition and/or death. The ataxia-telangiectasia and Rad3-related (ATR) inhibitor ceralasertib and the poly (ADP-ribose) polymerase (PARP) inhibitor olaparib have shown synergistic activity, in vitro, in the FaDu ATM-KO cell line. Experimental data has shown that when combined, lower doses of the drugs for shorter treatment times can induce greater toxicity in cancer cells compared to using either drug as a monotherapy.

Here, we develop biologically-motivated mathematical models that include the cell cycle-specific interactions of both ceralasertib and olaparib to: (1) explore the prominence of each cell cycle-specific drug interaction, (2) find optimal doses of ceralasertib and olaparib in combination, and (3) study the competition for space between drug-sensitive and drug-resistant cancer cells that are subjected to DDR inhibitor drugs. These models are implemented using both deterministic ordinary differential equation (ODE) models and a stochastic agent-based model (ABM) and are parameterised and evaluated against in vitro data.

Acknowledgements

I would like to thank everybody who has helped and supported me throughout my PhD journey. I would first like to thank my supervisor Professor Gibin Powathil, thank you for always guiding and encouraging me, and for always giving me advice. I would also like to thank my collaborator Doctor Sara Hamis for her continuous support and help throughout my entire PhD.

Thank you to EPSRC for fully funding this PhD, and to everyone in AstraZeneca who helped us with the development of the mathematical models, in particular Michael Davies, and to those who worked on the in vitro experiments that provided us with the experimental data.

I would also like to thank my mother, father, and sister for always being there for me and encouraging me along the way. Thank you to all of my friends and colleagues at Swansea University who made me look forward to coming to work each day and for helping me if I was ever stuck - I cannot express how grateful I am to every single one of you in CoFo! In no particular order, thank you to Nora Almania, Sarah Alhouli, Hassan Eshkiki, Sadeer Beden, Gavin Bailey, Carlos Baptista De Lima, Harry Bryant, Damiano Greco, Kévin Spinicci, Leonardo Lonati, Andrew Pulsipher, Harry Bevan, Connor Blake Hurley, Jamie Duell, Vittorio Cipriani, Victor Cai, Vianney Domenech, Osian Smith, and William Bean. A special thank you to Samuel Oliver, whom I have travelled with on each conference, who has been my notepad when I couldn't figure something out, and for always helping me with anything and everything.

Declaration of Authorship

This work has not been previously accepted in substance for any degree and is not being concurrently submitted in candidature for any degree. The work in this thesis has, however, undergone peer review and has been presented at major international venues. The publications noted below were prepared for submission during my candidature. The work in chapters 2 and 3 has been published. The work in Chapters 4 and 6 is to be submitted for publication. Details of the paper are documented below.

(P1) Kira Pugh, *Michael Davies and Gibin Powathil. Journal of Pharmacology and Experimental Therapeutics. 2024. A Mathematical Model to Investigate the Effects of Ceralasertib and Olaparib in Targeting the Cellular DNA Damage Response Pathway. DOI:https://doi.org/10.1124/jpet.122.001558*

DECLARATION - This work has not previously been accepted in substance for any degree and is not being concurrently submitted in candidature for any degree.

Signed [redacted] _____ (candidate)

Date _____

Statement 1 - This thesis is the result of my own investigations, except where otherwise stated. Other sources are acknowledged by footnotes giving explicit references. A bibliography is appended.

Signed [redacted] _____ (candidate)

Date _____

Statement 2 - I hereby give consent for my thesis, if accepted, to be available for electronic sharing after expiry of a bar on access approved by the Swansea University.

Signed [redacted] _____ (candidate)

Date _____

Statement 3 - The University's ethical procedures have been followed and, where appropriate, that ethical approval has been granted.

Signed [redacted] _____ (candidate)

Date _____

Contents

List of Figures

List of Tables

List of Abbreviations

2-D	**2**-**D**imensional
3-D	**3**-**D**imensional
ABM	**A**gent-**B**ased **M**odel
ATM	**A**taxia-**T**elangiectasia **M**utated
ATR	**A**taxia-**T**elangiectasia and **R**ad3-related
ATRi	**ATR I**nhibitor
BRCA	**Br**east **Ca**ncer gene
CI	**C**ombination **I**ndex
DDR	**D**NA **D**amage **R**esponse
DMSO	**Dim**ethyl **S**ulf**o**xide
DNA	**D**eoxyribo**n**ucleic **A**cid
DSB	**D**ouble-**S**trand **B**reak
FaDu ATM-KO	**FaDu ATM-K**nock**o**ut
G0	**Q**uiescence
G1	**G**ap **1**
G2	**G**ap **2**
G2D	**G2/M** Phase **D**amage
HC	**H**igh **C**omplexity
HRR	**H**omologous **R**ecombination **R**epair
HSA	**H**ighest-**S**ingle **A**gent
LHS	**L**atin **H**ypercube **S**ample
LSD	**L**owest-**S**ingle **D**ose
M	**M**itosis
MC	**M**edium **C**omplexity
MOOCS-DS	**M**ulti-**O**bjective **O**ptimization of **C**ombination **S**ynergy - **D**ose **S**election
MTD	**M**aximum **T**olerated **D**ose
NC	**N**on-**C**ycling
NHEJ	**N**on-**H**omologous **E**nd **J**oining
O.N.	**O**rder **N**eighbourhood
ODE	**O**rdinary **D**ifferential **E**quation
PARP	**P**oly (**A**DP-**R**ibose) **P**olymerase
PARPi	**PARP I**nhibitor
PI	**P**ercent **I**nhibition
PI3K	**P**hospho**i**nositide **3**-**K**inase
RMSE	**R**oot **M**ean **S**quare **E**rror
S	**S**ynthesis

SA	**S**ensitivity **A**nalysis
SD	**S** Phase **D**amage
seDSB	**S**ingle-**E**nded **DSB**
SoE	**S**ynergy **o**f **E**fficacy
SoP	**S**ynergy **o**f **P**otency
SSB	**S**ingle-**S**trand **B**reak
ssDNA	**S**ingle-**S**tranded **DNA**

List of Nomenclature

A_1	The time-dependent rate constant that represents delayed cell death caused by ceralasertib in Model HC.
C_{ABM}	The carrying capacity in the ABMs.
C_{HC}	The carrying capacity in Model HC.
C_{MC}	The carrying capacity in Model MC.
d	The distribution sizes in the consistency analysis, i.e., the number of in silico simulations needed to be run per experiment that mitigated uncertainty originating from intrinsic model stochasticity in the ABM.
d_1	The dose of a drug, drug 1, given in combination with another drug, drug 2.
d_2	The dose of a drug, drug 2, given in combination with another drug, drug 1.
D_0	The fraction of cells in state D at the start of the simulation in Model HC.
D_1	The dose of a drug, drug 1, given as a monotherapy.
D_2	The dose of a drug, drug 2, given as a monotherapy.
E	The effect of the drugs to calculate drug synergy.
E_1	The sigmoid Emax model equation for ceralasertib in Model MC.
E_2	The sigmoid Emax model equation for olaparib in Model MC.
$E_{1,2}$	The combined effect of ceralasertib and olaparib using the Bliss independence synergy model in Model MC.
$E_{50,1}$	The concentration of ceralasertib that results in half the maximal effect in Model MC and the ABMs.
$E_{50,2}$	The concentration of olaparib that results in half the maximal effect in Model MC and the ABMs.
$E_{\max,1}$	The maximal drug effect of ceralasertib in Model MC and the ABMs.
$E_{\max,2}$	The maximal drug effect of olaparib in Model MC and the ABMs.
$E_{\max,O}$	The maximal drug effect of olaparib increasing p in Model HC.
$EC_{50,O}$	The concentration of olaparib that results in half of $E_{\max,O}$ in Model HC.
$f_j(t_k)$	The simulation cell confluency at time t_k for drug treatment j.

$f_j(t_k, p_i^l)$	The simulation cell confluency at time t_k for drug treatment j when changing the value of parameter p_i to each of the investigated values p_i^l, $l = 1, \ldots, 10$.
g_d	The distribution groups used in the consistency analysis in the ABM.
$G0_0$	The fraction of cells in state G0 at the start of the simulation in the ABMs.
$G1_0$	The fraction of cells in state G1 at the start of the simulation in Model HC, Model MC, and the ABMs.
$G2D_0$	The fraction of cells in state G2D at the start of the simulation in Model HC.
$G2/M_0$	The fraction of cells in state G2/M at the start of the simulation in Model HC, Model MC, and the ABMs.
h_1	The Hill coefficient of ceralasertib in Model MC and the ABMs.
h_2	The Hill coefficient of olaparib in Model MC and the ABMs.
$h_{C,1}$	The Hill coefficient of ceralasertib inhibiting the repair of cells in state SD in Model HC.
$h_{C,2}$	The Hill coefficient of ceralasertib-related cell death in Model HC.
$h_{O,1}$	The Hill coefficient of olaparib increasing p in Model HC.
$h_{O,2}$	The Hill coefficient of olaparib inhibiting repair of cells in state G2D in Model HC.
$I_{\max,C}$	The maximal drug effect of ceralasertib inhibiting the repair of cells in state SD in Model HC.
$I_{\max,O}$	The maximal drug effect of olaparib inhibiting repair of cells in state G2D in Model HC.
$IC_{50,C}$	The concentration of ceralasertib that results in half of $I_{\max,C}$ in Model HC.
$IC_{50,O}$	The concentration of olaparib that results in half of $I_{\max,O}$ in Model HC.
k_1	The rate at which cells leave state G1 in Model HC and Model MC.
k_2	The rate at which cells leave state S in Model HC and Model MC.
k_3	The rate at which cells leave state SD and enter state S in Model HC and the rate at which cells leave state S in Model MC.
k_4	The rate at which cells leave state SD and enter state D in Model HC and the rate at which cells leave state G2/M in Model MC.
k_5	The rate at which cells leave state G2/M and enter state G1 in Model HC.
k_6	The rate at which cells leave state SD and enter state G2D in Model HC.
k_7	The rate at which cells leave state G2D and enter state G2/M in Model HC.

k_8	The rate at which cells leave state G2D and enter state D in Model HC.
k'	The k'^{th} distribution in the consistency analysis in the ABM.
k'_1	The rate at which cells leave state G1 in the absence of cell crowding in Model MC.
k'_2	The rate at which cells leave state S in the absence of cell crowding in Model MC.
k'_3	The rate at which cells leave state SD in the absence of cell crowding in Model MC.
k'_4	The rate at which cells leave state G2/M in the absence of cell crowding in Model MC.
$K_{\text{max},C}$	The maximal drug effect of ceralasertib killing cells from state G2D in Model HC.
$KC_{50,C}$	The concentration of ceralasertib that results in half of $K_{\text{max.C}}$, i.e. the sensitivity constant in Model HC.
l	The number of values we investigate for each parameter in the robustness analysis, $l = 1, 2, \ldots, 10$.
m	The number of transit compartments used for death delay in Model HC.
μ_{P*}	The number of cells when the drugs are administered in the ABMs is picked from a uniform distribution with mean μ_{P*}.
μM	Drug concentration in micromolar.
n	The number of cells per seeded cluster in the ABMs.
N	The number of seeded clusters in the ABMs.
$N(0)$	The total number of initial cells in Model MC.
$N(t)$	The total number of cells in the system at time t in the compartment models.
$N_j(t_{\text{end}})$	The total number of cells in the system in Model MC at the end time t_{end} for drug treatment j.
NC_0	The fraction of cells in state NC at the start of the simulation in Model HC, Model MC, and the ABMs.
η	The number of experimental data time points.
p	The probability that cells transition from state G1 to SD in Model HC and the drug-dependent probability that cells will transition from state G1 to S in Model MC and the ABMs.
p_0	The probability that cells transition from state G1 to state S in Model MC and the ABMs.
p_i	The input parameters from Model HC used in the sensitivity analysis, $i = 1, 2, \ldots, 24$.
p_i^j	The appropriate parameter values we get from the Latin hypercube sample using equation 3.2, where $i = 1, 2, \ldots, 24$ and $j = 1, 2, \ldots, w$.
p_i^l	The value of parameter p_i for each of the investigated values, $l = 1, \ldots, 10$.
p_i^L	The lower bound of parameter p_i.
p_i^U	The upper bound of parameter p_i.

$P(t)$	The cell population at time t in the ABMs.
P_0	The number of seeded cells in the ABMs.
P^*	The number of cells when the drugs are administered in the ABMs.
PI^i_{50}	The percent inhibition of drug i that achieves 50% of the desired effect compared to the control case.
q	The probability that cells transition from state S to G2D in Model HC and the drug-dependent probability that cells will transition from state SD to S in Model MC and the ABMs.
q_0	The probability that cells transition from state SD to state S in Model MC and the ABMs.
s	The scaling parameter that adjusts for cell cycle arrest.
S_0	The fraction of cells in state S at the start of the simulation in Model HC, Model MC, and the ABMs.
SD_0	The fraction of cells in state SD at the start of the simulation in Model HC, Model MC, and the ABMs.
σ	The doubling time of cells in the ABMs is picked from a normal distribution with mean σ.
σ_{P*}	The number of cells when the drugs are administered in the ABMs is picked from a uniform distribution with standard deviation σ_{P*}.
t_d	The time at which the drugs are administered in the ABMs.
T_j	The doubling time of cell$_j$ in the ABMs.
τ	The doubling time of cells in the ABMs is picked from a normal distribution with mean τ.
τ_{G1}	The fraction of a cell's doubling time spent in state G1 in the ABMs.
$\tau_{G2/M}$	The fraction of a cell's doubling time spent in state G2/M in the ABMs.
τ_R	The doubling time of resistant cells in the ABMs is picked from a normal distribution with mean τ_R.
τ_S	The fraction of a cell's doubling time spent in state S in the ABMs.
τ_{SD}	The fraction of a cell's doubling time spent in state SD in the ABMs.
θ	The transit step time in Model HC.
v_B	The neighbourhood-order in which daughter cells can be placed in the baseline ABM.
v_C	The neighbourhood-order in which daughter cells can be placed in the cell crowding limited ABM.
w	The number of values we investigate for each parameter in Latin hypercube analysis.
X_1	The cell confluency with 0.3 μM ceralasertib and 0.2 μM olaparib halfway through the simulations.
X_2	The cell confluency with 0.3 μM ceralasertib and 0.2 μM olaparib at the end of the simulations.

X_i^j	The values we get from the Latin hypercube sample, where $i = 1, 2, \ldots, 24$ and $j = 1, 2, \ldots, w$.
$y_{j,k}$	The experimental cell confluency data points where j is the drug treatment and k is each experimental time point.

Dedicated to my family and

friends.

Chapter 1

Introduction

Cancer remains a leading cause of death worldwide [17, 184]. It is estimated that half of the people born in the United Kingdom will be diagnosed with cancer at some point in their lives [27]. Due to the heterogeneous and complex nature of cancer, which makes certain treatments ineffective [17], only around half of those diagnosed with cancer in England and Wales will survive for 10 or more years after diagnosis [27]. Thus, there is a desperate need for further cancer research to be conducted to improve treatment strategies and increase cancer survival. In vitro and in vivo experiments have become crucial in cancer research, studying cell growth, metastasis, drug resistance, and anti-cancer treatments [120]. However, these studies can be costly and time-consuming. Mathematical oncology is a growing field of research that uses mathematical and computational models to study cancer that offers an ethical, quick, and easily adaptable way to complement and supplement conventional experimental studies [120, 73]. These models have been widely adopted to gain more understanding of biological cancer systems, study optimal treatment strategies, and produce predictions on cancer progression [73, 119, 153, 17]. They can also be used to test theories developed in laboratories and/or clinics that are unfeasible to test in experimental settings, or even to validate or guide experimental studies [73].

1.1 Biological Background

To proliferate, cells must progress through the cell cycle, a process where cells replicate and duplicate their deoxyribonucleic acid (DNA) to create two daughter cells [91]. The cell cycle is controlled by protein kinases known as cyclin-dependent kinases and consists of four main phases: gap 1 (G1), synthesis (S), gap 2 (G2), and mitosis (M) [91]. Cells in the G1 phase grow and prepare for DNA replication, which occurs in the S phase, and cells in the subsequent G2 phase prepare for cell division, which occurs in the M phase [91] (Figure 1.1).

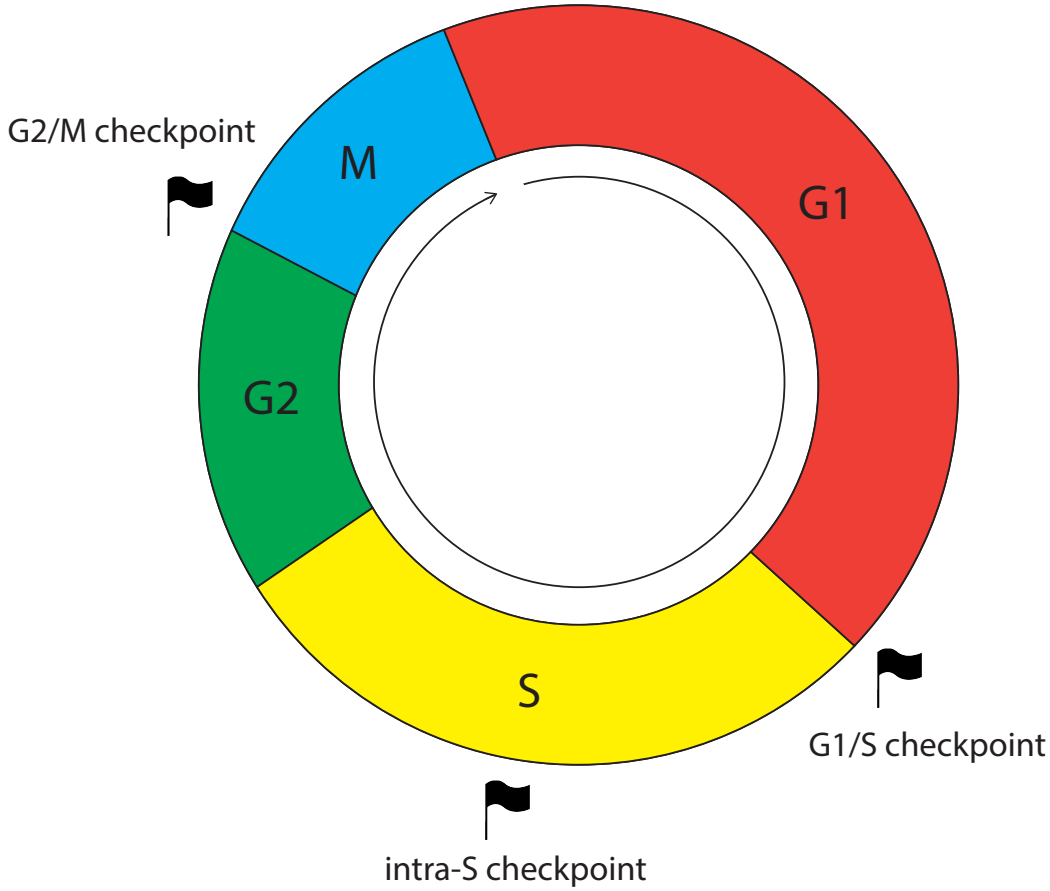

FIGURE 1.1: **The cell cycle process based on work by O'Connor (2015).** Cells progress through the gap 1 (G1), synthesis (S), gap 2 (G2), and mitosis (M) phases. Cells must pass the cell cycle checkpoints to progress through the cell cycle. If a damaged cell encounters a checkpoint, it should be arrested to allow time for repair.

1.1.1 DNA Damage

Every day, each cell in the human body faces roughly 70,000 lesions of DNA damage [173]. DNA damage could be due to endogenous damage such as DNA replication errors [13], oxidation damage [37], and hydrolysis [41]. Furthermore, DNA damage could be due to exogenous damage such as sunlight [13], cigarette smoking [85], and ionising radiation [137]. The most common form of DNA damage is single-strand breaks (SSBs), which occur approximately 10,000-55,000 times to each cell per day [137, 173, 84]. SSBs occur when one strand in the DNA double helix is broken [84]. The repair of SSBs relies heavily on the family of enzymes poly (ADP-ribose) polymerase (PARP) [129]. PARP is responsible for detecting the break, binding to the break to avoid further damage, and then dissociating from the break to allow for repair [83, 113, 137, 78, 162].

The most cytotoxic and difficult DNA damage to repair is double-strand breaks (DSBs) [137], which occur around 25 times per cell, per day [173]. DSBs occur when both strands in the DNA double helix are broken [118]. These commonly arise during the replication process from replication errors [13]. For example, a SSB can collide with the replication fork if not repaired before DNA replication (Figure 1.2). This can cause the replication fork to stall or collapse, which can form single-ended DSBs (seDSBs) [113, 83, 137, 130, 78, 12]. The homologous recombination repair (HRR) pathway is the only pathway to accurately repair seDSBs [12, 95]. HRR works by using the identical sister chromatid as a template for repair [44]. This means

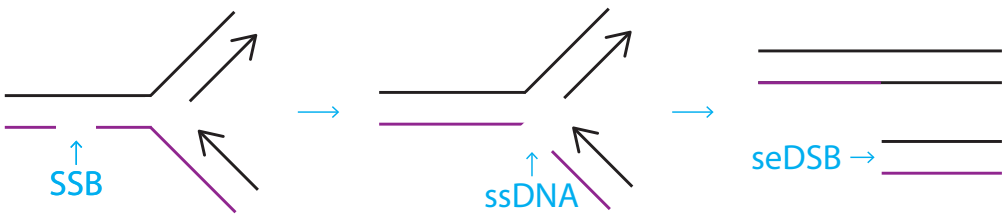

FIGURE 1.2: **Unrepaired DNA lesions can lead to further DNA damage based on work by Helleday *et al.* [79].** SSBs can collide with the replication fork if left unrepaired, which results in seDSBs.

that HRR is restricted to the S and G2 phases when the sister chromatid is available [44, 18]. During the end resection stage in HRR, single-stranded DNA (ssDNA) overhangs are formed [103, 93], which activates ataxia telangiectasia and Rad3-related (ATR) [18, 34, 76]. Therefore, ATR is a key protein involved in the repair of replication stress. Another common DSB repair pathway is non-homologous end-joining (NHEJ), which operates throughout the cell cycle and works by ligating the broken ends of the DSB without the need for a homologous template [118]. This means that NHEJ is suitable for double-ended DSBs where the two broken ends can easily be joined together [50]. However, since seDSBs only have one distal end, the repair of seDSBs via NHEJ can lead to genetic rearrangements and genomic instability [32, 40, 44].

1.1.2 DNA Damage Response

In response to DNA damage, many intracellular events are triggered to detect and repair the damage. These cellular responses are associated with the DNA damage response (DDR). The DDR is regulated by proteins which are responsible for detecting DNA damage, arresting damaged cells to allow time for repair, activating the repair mechanisms, and inducing apoptosis if the damage is too severe for repair [76]. The DDR consists of cell cycle checkpoints, which cells must pass through to continue through the cell cycle. The main checkpoints are the G1/S checkpoint, the intra-S checkpoint, and the G2/M checkpoint [137] (Figure 1.1). The activation of the cell cycle checkpoints relies heavily on the ATR and ataxia-telangiectasia-mutated (ATM) proteins, both of which are members of the phosphoinositide 3-kinase (PI3K) family [76, 29]. If a damaged cell encounters a checkpoint, it should be arrested to allow time for repair [137, 157]. In cancer cells, certain aspects of the DDR tend to be faulty [6]. For example, the proteins responsible for activating the checkpoints may be defective, which allows DNA damaged cells to pass the checkpoints and potentially cause deleterious mutations during replication and division, which could cause cancer [13].

1.1.3 DNA Damage Response Inhibitor Drugs

Many anti-cancer treatments target cells in specific phases of the cell cycle [68]. Examples of cell cycle-specific drugs are DDR inhibitor drugs, which can inhibit specific pathways in the DDR [188]. DDR inhibitor drugs can take advantage of cancer cells with certain DDR defects, by simultaneously deactivating their relevant DDR pathways to maximise DNA damage [20]. These DDR deficiencies in cancer cells can be exploited by DDR inhibitor drugs through synthetic lethality [20]. The concept of synthetic lethality is that the loss/inhibition of two functions in the DDR is lethal to the cell, whereas the cell can function with the loss/inhibition of either one alone [137, 139]. One example of synthetic lethality is PARP inhibitor (PARPi) drugs in cells with breast cancer gene (BRCA) mutations. BRCA1/2 are important in HRR, hence, when a PARPi (such as olaparib) is given in a HRR-deficient cancer, the PARPi generated seDSBs, which need HRR to be accurately repaired, will cause genomic instability because other repair pathways (such as NHEJ) will repair the damage inaccurately [22, 78, 113].

In this study, we focus on two DDR inhibitor drugs: ceralasertib and olaparib. Ceralasertib is an ATR inhibitor (ATRi) drug that inhibits the activity of ATR. This causes a greater reliance on other mechanisms of the DDR, such as ATM [113, 34, 76, 29]. Treatment with ceralasertib can inhibit cell cycle checkpoint activation and the repair of DNA replication damage [113, 137, 34, 76]. This is because ATR is important for activating the G2/M checkpoint, which prevents damaged cells from progressing to mitosis [113, 34]. Therefore, treatment with ceralasertib can cause genomic instability which can lead to mitotic catastrophe [113, 34, 29]. Currently, ceralasertib is used in clinical Phase I and II trials for treating advanced solid tumours, advanced solid malignancies, and melanomas that are resistant to programmed death-ligand 1 inhibitors [180, 9, 10]. Olaparib is a PARPi drug that inhibits the enzymatic activity of PARP1/2. Treatment with olaparib has been shown to trap PARP1 onto SSBs, which inhibits their repair [113, 109]. If not repaired before

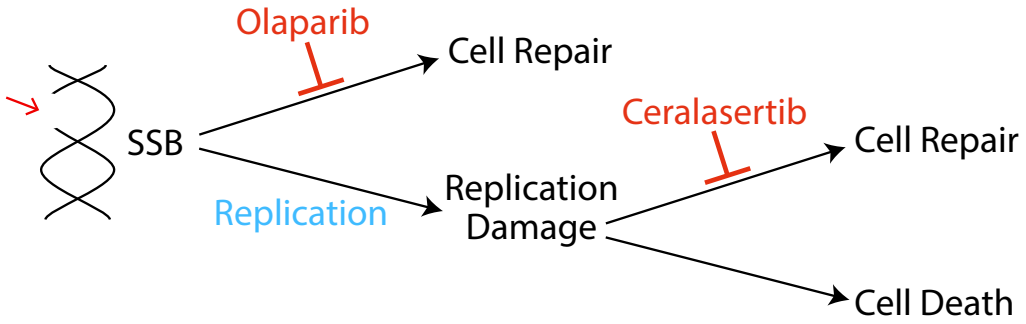

FIGURE 1.3: **The synergy between PARP and ATR inhibitor drugs.** Olaparib can inhibit the repair of SSBs. If SSBs are not repaired before the replication process, they can collide with the replication fork and cause replication damage. Ceralasertib can inhibit the repair of DNA replication damage. When given in combination, ceralasertib and olaparib can reduce the number of cancer cells that are repaired, thus increasing the amount of cell death.

DNA replication, DNA SSBs can lead to DNA replication stress, which may cause cell death. PARP has also been shown to contribute to DNA replication fork reversal and stability, thus, PARP inhibition can lead to increased genomic instability [151]. Olaparib is FDA-approved for the treatment of ovarian, breast, pancreatic, and prostate cancer [54, 53, 52, 55].

Combining ceralasertib and olaparib has demonstrated synergistic activity both in vitro and in vivo [113]. Their combination is currently being used in Phase II clinical trials [92, 1]. The synergy between PARP and ATR inhibitors is described in Figure 1.3 and could also be explained by them being the primary regulators of the cell cycle checkpoints [76]. It is fairly common for diseases to have mutations in ATM [34], which causes a greater reliance on ATR for checkpoint signalling and DNA repair [113]. Using an ATRi in ATM-deficient cancers targets only the cancer cells which lack ATM for signalling, while sparing the non-cancerous cells with intact ATM function [178, 128, 113].

1.2 Mathematical Modelling

Recently, mathematical and computational modelling approaches have been considered an effective and complementary way to study cancer progression and anti-cancer treatments [24]. These models are able to incorporate and investigate details such as cell proliferation, cell death, and drug interactions. By intertwining biological data from in vitro studies, in vivo studies, or clinical trials with mathematical models, we may help limit the need for animal studies [94, 153, 154]. There exists many databases and software for building models of cancer cell populations, some of which are mentioned by Edelma *et al.* [46]. Mathematical models of cancer cell populations provide a quick, cheap, and ethical way to investigate hypotheses that are unfeasible to test in experimental settings [73, 153]. For example, in silico models have been developed to study how the spatial architecture of cancer cells affects drug treatment [168]. In silico models can also be used to study optimal dosage, sequencing, and scheduling of anti-cancer drug treatments as monotherapies or in combination [165]. Mathematical models have previously been used to inform experimental and clinical studies [34, 189]. For example, Checkley *et al.* [34] developed a mechanistic cell cycle model that has been used in Phase I clinical trials to help predict efficacious starting doses of ATRi and ironising radiation alone and in combination. Furthermore, a game theory model developed by Zhang *et al.* [189] has also been used in clinical trials of prostate cancer to predict personalised treatment strategies.

Many anti-cancer drugs are cell cycle-specific [68], which means that cells in particular phases of the cell cycle can be more sensitive to certain treatments compared to cells in other phases. Cell cycle-specific drugs include DDR inhibitor drugs such as ceralasertib and olaparib, which we study in this thesis. The distribution of cells can be studied in vitro using flow cytometry, a technology that allows us to track cell cycle progression and determine the cell cycle phases [125, 142]. In this thesis, inspired by in vitro data, we aim to implement cell cycle dynamics into the

mathematical models we develop and study the cell cycle phase-specific interactions of the drugs.

There exist many modelling approaches to study cell cycle-specific drug interactions. For example, multiscale modelling is a popular approach for modelling tumour growth and drug effects [25, 110, 182, 42, 49]. Models that study cancer growth include deterministic models which produce the same output each time (e.g., ordinary differential equation and partial differential models) and stochastic models which produce a different output each time (e.g., agent-based models) [158, 24]. Among the various modelling approaches that exist, we focus on two: ordinary differential equation (ODE)-based models and agent-based models (ABMs). In this thesis, we aim to develop a data-informed ODE-based model to study temporal dynamics and a data-informed multiscale mathematical model to incorporate multiple scales of information in space and/or time [73].

1.2.1 ODE-Based Models

ODE-based models describe the temporal evolution of cancer cell populations [33, 24]. For example, compartment models comprise a set of compartments (i.e., variables) that are represented by a system of ODEs. They provide a fairly straightforward way to implement cancer cell populations and drug interactions as each compartment can represent the number of cells in a certain cell cycle state. For instance, compartments can represent the cell cycle phases (G1, S, G2, M), where cells can move between compartments via rate constants. These types of models have been used to study the responses of cancer cell populations to monotherapies and combinations of radiation [34], chemotherapy drugs [70, 127, 126, 114, 155, 190], and DDR inhibitor drugs [147, 34, 155, 190].

In the early 1990s, Béla Novák and John J. Tyson started their journey of modelling the cell cycle, now with over 40 papers on cell cycle regulation in mammalian cells and yeast cells [38]. To control progression through the cell cycle, each cell has its

own mechanisms [134]. Therefore, they developed a six-variable model governed by a set of ODEs, where five variables represent protein concentrations, and one variable represents cell mass [174, 133, 72, 145]. To determine the phase of a cell, the authors assess the values of the proteins, and when a daughter cell is produced, the cell mass is halved. The model developed by Tyson and Novák [174] has been extended by Alarcón *et al.*, who included the effects of p27, a protein which is upregulated under hypoxic regions [3].

1.2.2 Agent-Based Models

ABMs can be utilised to describe the spatio-temporal dynamics of cancer cell populations, which can include multiple different agents that can interact with each other and their environment [73, 24]. For instance, an agent could represent a cancer cell. One may create a heterogeneous population if cells exhibit different phenotypes [77]. To control cell cycle progression, the system of ODEs presented by Tyson and Novák [174] and Alarcón *et al.* [3] have been implemented into various ABMs such as those developed by Powathil *et al.* [145] who studied the effects of chemotherapy on the cell cycle and Hamis *et al.* [72] who studied chemotherapeutic drug resistance in cancer. Another common way to implement the cell cycle in ABMs is to assign each cell with a cell cycle clock where each cell spends an allotted amount of time in each phase. ABMs that incorporate the cell cycle in this manner can, and have been used to study treatment responses to radiation [23, 100, 152, 5], chemotherapy drugs [143], DDR inhibitor drugs [76], and hypoxia-activated prodrugs [75] in simulated cancer cells.

Furthermore, modelling frameworks such as PhysiCell and CompuCell3D have become a popular tool for studying the proliferation of cancer cells. PhysiCell is an open-source physics-based cell simulator that simulates cells in 3D tissues [64, 63]. Similarly, CompuCell3D is another modelling environment that produces a multiscale environment that uses the Cellular Potts Model to model cell behaviour [169].

In this thesis, we aim to develop both compartment models and ABMs which incorporate the cell cycle-specific interactions of DDR inhibitor drugs and study their effects on cell proliferation.

1.3 Experimental Data

In an in vitro study, Lloyd *et al.* [113] proposed synergy between ATR and PARP inhibitor drugs in ATM-deficient cancer cell lines. In this thesis, we study this synergy and investigate optimal doses of the drugs. To do so, we develop, train, and test our mathematical models using experimental data performed by the global pharmaceutical company AstraZeneca [113]. The data is from in vitro experiments in which cells from the FaDu ATM-knockout (ATM-KO) cell line, an epithelial morphology cell line derived from a human with squamous cell carcinoma, were subjected to two DDR inhibitor drugs, namely ceralasertib and olaparib. FaDu ATM-KO cells are ATM-deficient. Two independent repeats of the in vitro experiments were conducted, which we will refer to as experimental data 1 (Figure 1.4) and experimental data 2 (Figure 1.5). In the experiments, cells were plated in wells (Figure 1.6) and exposed to different doses of ceralasertib and olaparib either alone or in combination with one another. Cells were treated with dimethyl sulfoxide (DMSO), a solvent commonly used as a vehicle in cell culture experiments, for the control case when there was no drug treatment.

Cell confluency (Figures 1.4 (a) and 1.5 (a)), apoptosis activity (Figures 1.4 (b) and 1.5 (b)), and cell death activity (Figures 1.4 (c) and 1.5 (c)) were measured approximately every 3 hours for 310 hours. Cells were co-stained with caspase 3/7 and cytotox to measure apoptosis and cell death activity respectively. Cell confluency and fluorescence intensities were measured using incucyte ZOOM 2016A software developed by Essen BioScience [87]. This software allows for real-time analysis of live cells plated in wells, enabling the measurement of cell morphology and phenotype [87]. Cell growth was measured by the percentage of phase confluency, i.e., how much

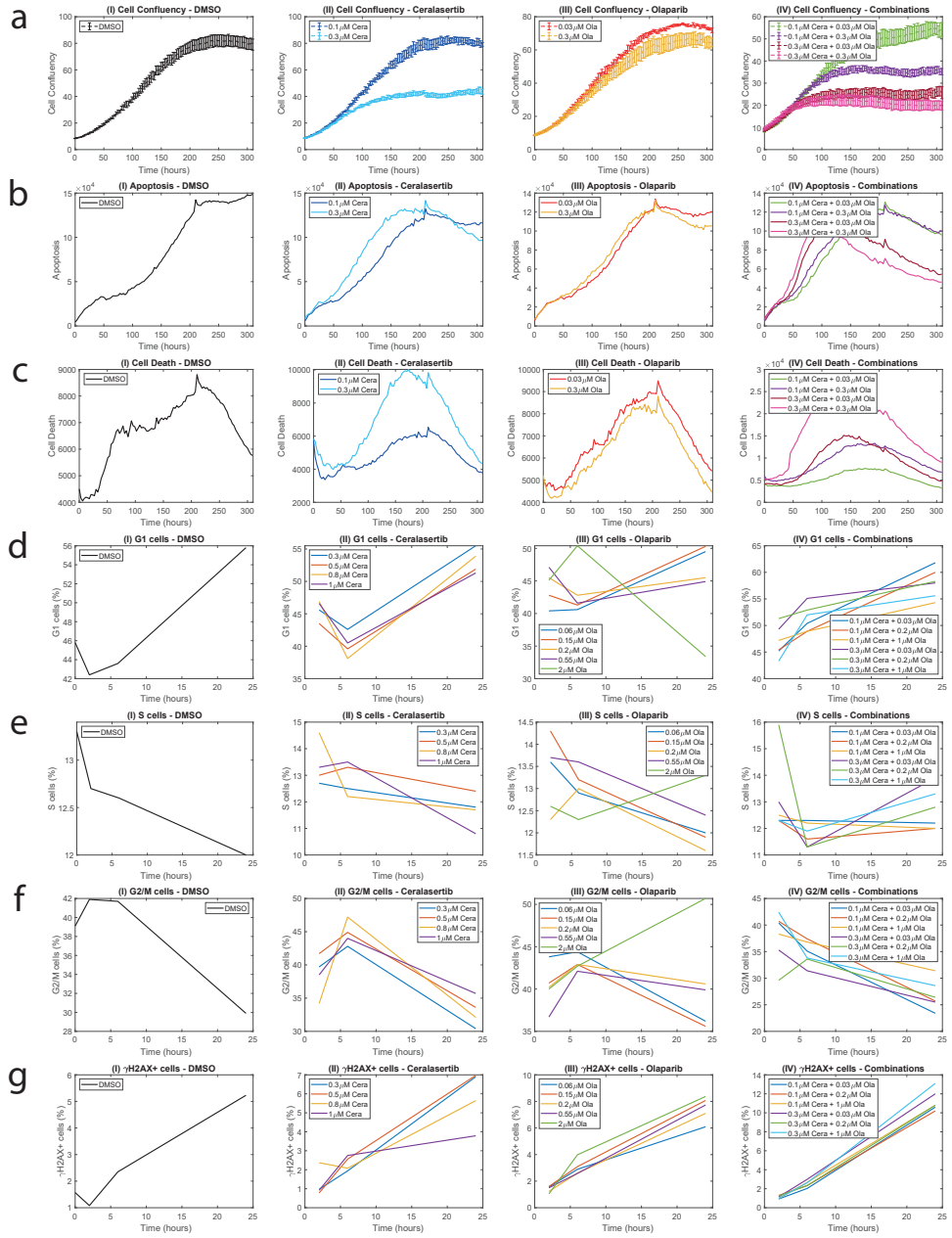

FIGURE 1.4: **Experimental data 1.** The in vitro experiments measured (a) cell confluency (%), (b) apoptosis activity, (c) cell death activity, (d) the percentage of cells in the G1 phase, (e) the percentage of cells in the S phase, (f) the percentage of cells in the G2/M phase, and (g) the percentage of cells in that are γH2AX positive. In (a)-(g), plots (I) represent no drug treatment, plots (II) represent ceralasertib monotherapy, plots (III) represent olaparib monotherapy, and plots (IV) represent combination therapy. The cell confluency displays the mean with standard error of the mean for 3 experiments indicated with error bars. The mean fluorescence levels of caspase 3/7 and cytotox were normalised to total cell confluency to measure apoptosis and cell death activity respectively.

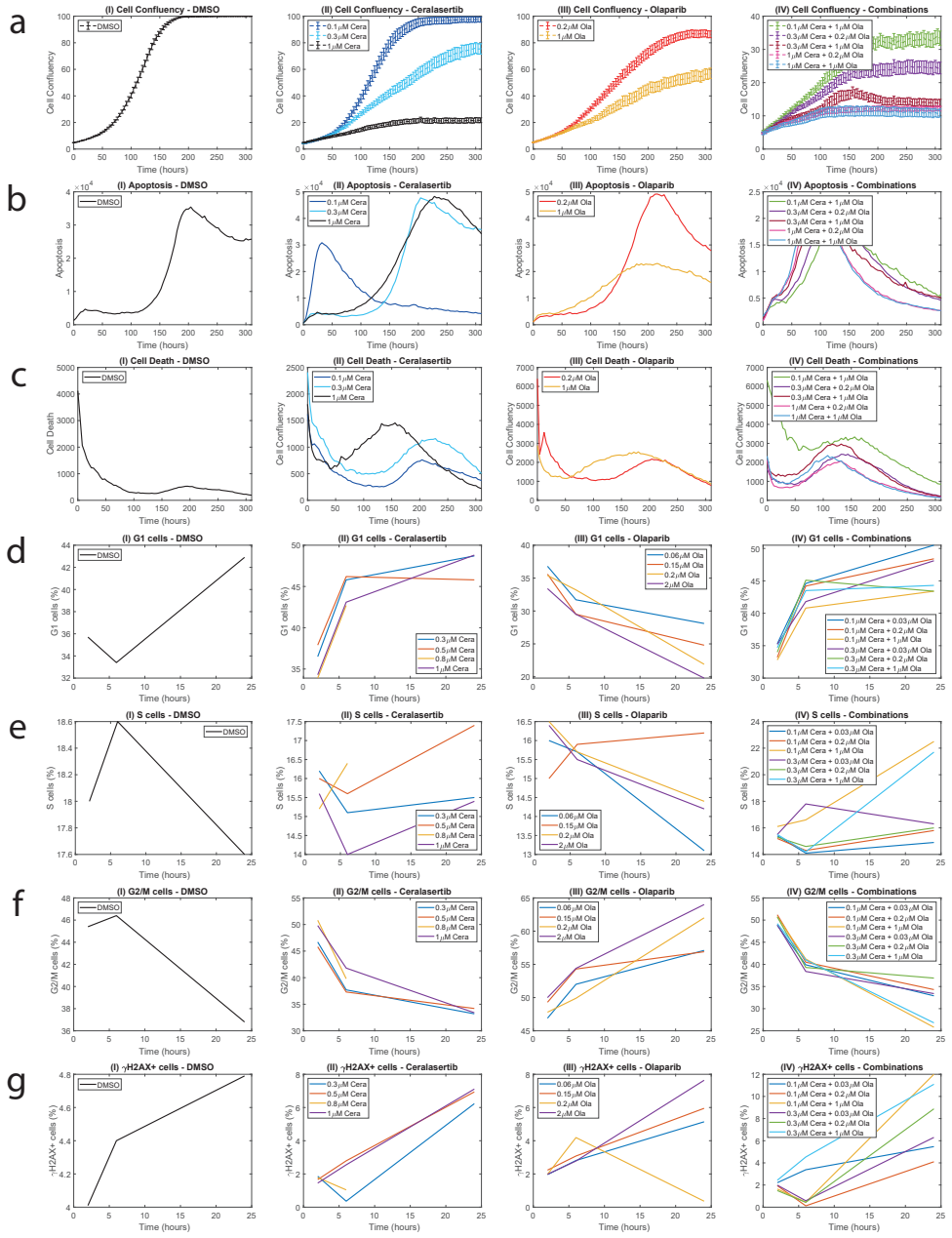

FIGURE 1.5: **Experimental data 2.** The in vitro experiments measured (a) cell confluency (%), (b) apoptosis activity, (c) cell death activity, (d) the percentage of cells in the G1 phase, (e) the percentage of cells in the S phase, (f) the percentage of cells in the G2/M phase, and (g) the percentage of cells in that are γH2AX positive. In (a)-(g), plots (I) represent no drug treatment, plots (II) represent ceralasertib monotherapy, plots (III) represent olaparib monotherapy, and plots (IV) represent combination therapy. The cell confluency displays the mean with standard error of the mean for 3 experiments indicated with error bars. The mean fluorescence levels of caspase 3/7 and cytotox were normalised to total cell confluency to measure apoptosis and cell death activity respectively.

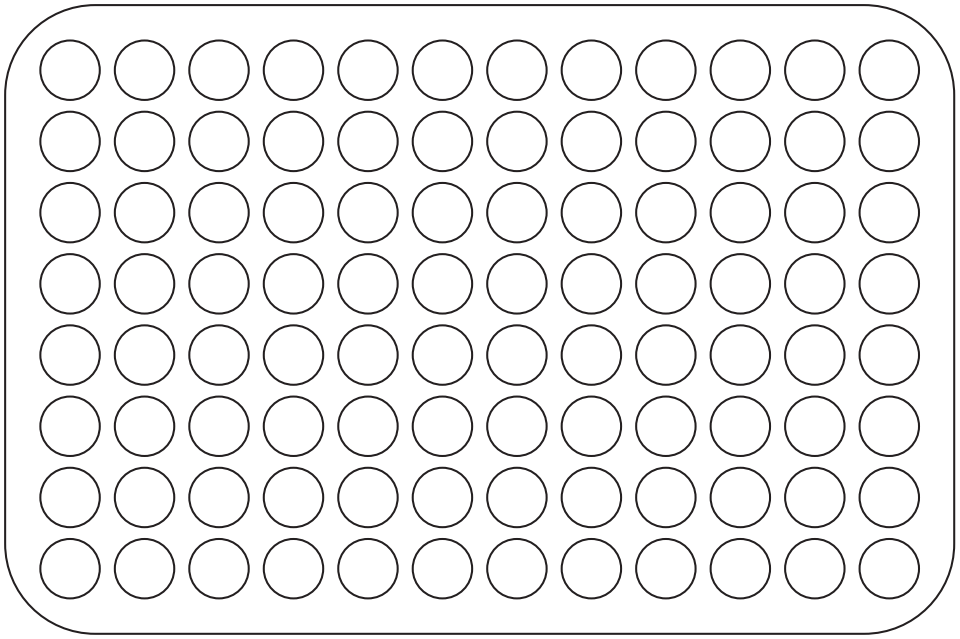

FIGURE 1.6: **Cells are plated in wells in the in vitro experiments.** An example of a 96-well plate.

area is covered with cells. Apoptosis was measured by mean fluorescence levels of active caspase 3/7 and the total number of dead cells in the well was measured by mean fluorescence levels of cytotox. This means that cells stained with caspase 3/7 and cytotox are undergoing apoptosis or cell death respectively, and cells not stained with these markers are not. Measuring apoptosis and cell death via fluorescence intensities means that the values correspond to the number of apoptotic cells/dead cells at the specific measurement point. Consequently, these values may not be cumulative. Experimental data 1 and 2 show significant variability. For instance, cells reach 100% cell confluence in experimental data 2 with no drug treatment (Figure 1.5 (a)), but they only reach 80% cell confluence with no drug treatment in experimental data 1 (Figure 1.4 (a)).

The experimental data also includes two independent repeats of EdU pulse-chase experiments, which track the progression of cells through the cell cycle phases over 24 hours. This data measured the percentage of cells in G1 (Figures 1.4 (d) and 1.5 (d)), S (Figures 1.4 (e) and 1.5 (e)), and G2/M (Figures 1.4 (f) and 1.5 (f)). It also

measured how many cells are γH2AX positive (Figures 1.4 (g) and 1.5 (g)), a marker of DNA damage [163, 113].

1.4 Thesis Outline

This thesis aims to develop mathematical models to:

1. Investigate the prominence of each cell cycle-specific drug interaction of ceralasertib and olaparib.
2. Find their potential optimal doses in combination.
3. Study the competition for space between drug-sensitive and drug-resistant cancer cells that are subjected to DDR inhibitor drugs.

To do so, we parameterise and evaluate our mathematical models against in vitro data (Section 1.3) [113].

In this thesis, we develop two compartment models, which we name high-complexity (Model HC) and medium-complexity (Model MC). We have chosen the term complexity to compare the mathematical models in terms of intricacy, number of compartments, and number of parameters. We first develop a compartment model with, Model HC, that is discussed in Chapter 2. This model is calibrated and evaluated against experimental data 1 (Section 1.3) and is used to investigate the temporal dynamics of a cancer cell population. We study the interactions of ceralasertib and olaparib and how the omission of each drug effect impacts the proliferation of the simulated cancer cell population. We also use this model to explore new combinations of the DDR inhibitor drugs to maximise cytotoxicity. In Chapter 3, we conduct a local and global sensitivity analysis to study how sensitive the output of Model HC is to perturbations in the parameter values.

To study the spatial competition and the interplay between drug-sensitive and drug-resistant cancer cells, we map a compartment model onto an ABM which can

investigate the spatial and temporal dynamics of cancer cell populations. Moreover, informed by the results of the sensitivity analyses and the need for a simplified model to map to the ABM, we simplify Model HC to Model MC to reduce the number of parameters. Details of the model simplification can be found in Chapter 4. This model is calibrated and evaluated against experimental data 2 (Section 1.3). In Chapter 5, Model MC is used to investigate the synergy between ceralasertib and olaparib using four reference models for synergy (Bliss, Highest-single agent (HSA), Loewe, and Lowest-single dose (LSD)) that determine if a drug combination dose is synergistic or not. We then use four criterion spaces that pair the reference models (Loewe-Bliss, LSD-Bliss, Loewe- HSA, and LSD-HS), which we use to investigate Pareto optimal doses that are deemed optimal on all four criterion spaces.

Lastly, in Chapter 6, we map Model MC onto a 2-D on-lattice ABM and introduce drug-resistant cancer cell populations. This model is calibrated and evaluated against experimental data 2 (Section 1.3) and is used to investigate the temporal and spatial dynamics of cancer cell populations. We study how treatment responses are impacted by: (i) differently seeded spatial configurations of the cells on the lattice, (ii) the initial fraction of drug-resistant cells, (iii) the drugs to which the cells are resistant, (iv) drug treatments (i.e., monotherapies and combinations of the drugs), (v) drug doses, and (vi) the doubling time of drug-resistant cells in relation to the doubling time of drug-sensitive cells.

Overall, our objective is to study treatment responses to combinations of ceralasertib and olaparib, considering scenarios both with and without the involvement of drug resistance and spatial competition.

Chapter 2

Compartment Model: Investigating Temporal Dynamics

2.1 Introduction

The ATR inhibitor drug ceralasertib and the PARP inhibitor drug olaparib are both cell cycle-specific drugs that target cells in specific phases of the cell cycle [113, 137, 109, 151]. Experimental studies have observed synergy between ceralasertib and olaparib [113]. Indeed, in vitro studies observed that these drugs can be combined with lower doses and for shorter treatment periods to induce greater or equal toxicity in cancer cells compared to using either drug as a single agent [113]. In this work, our focus is to explore the effects of these drugs in combination. We investigate which drug effects exert the most significant growth inhibition of cancer cell populations to gain a better understanding of the drugs. Furthermore, we study new combination doses of ceralasertib and olaparib which could potentially optimise cytotoxicity.

One way to study drug interactions and to explore new drug combinations is through mathematical modelling. Recently, Checkley *et al.* [34] developed a mathematical model of the cell cycle to study the effects of ceralasertib alone and in combination with ionising radiation. The authors calibrated their model to a

human colon carcinoma cell line and then translated the model into a tumour growth model developed by Evans *et al.* [51]. The translated model simulated time series tumour growth following treatment and was compared to in vivo mouse xenografts. The model was used to inform clinicians of the efficacious starting doses for Phase I clinical trials of ceralasertib monotherapy and in combination with ionising radiation. Similarly, Miao *et al.* [126] developed mathematical models of the cell cycle which were used to study the chemotherapy drugs gemcitabine and trabectedin as monotherapies and in combination. The model was fitted to multiple in vitro cell lines and was able to capture the different cell line-specific drug interactions. They used these models to study the effects of the drugs on the cell cycle and identified that gemcitabine targets cells in the S phase, whereas trabectedin targets cells in the S and G2/M phases.

Motivated by these previous mathematical models, we develop a biologically motivated compartment model with high complexity (HC), which we call Model HC. The mathematical model considers the cell cycle-specific interactions of the DDR inhibitor drugs, ceralasertib and olaparib (Section 2.2.1). In the model, each drug targets cells in multiple cell cycle phases. We explore the model with and without these drug effects to investigate which effects have the most effect on the total growth inhibition of simulated cancer cells (Section 2.3.1). After careful model selection, the model is calibrated (Section 2.3.2) and compared (Section 2.3.3) to experimental data 1 (Section 1.3) obtained from our collaborators AstraZeneca. Furthermore, we use this model to investigate new doses of ceralasertib and olaparib in combination, which have not been studied in vitro (Section 2.3.4). This can be potentially helpful in exploring optimised drug dosage and delivery.

2.2 Model and Method

Inspired by the models developed by Checkley *et al.* [34] and Miao *et al.* [126] and the need for an updated model to study the effects of ceralasertib and olaparib as

monotherapies and in combination, we develop an extended model by considering relevant biological interactions of ceralasertib and olaparib. The simulations of the model are implemented in MATLAB and the parameters have been estimated using a non-linear least squares method [108], which calibrates the mathematical model to experimental data 1 (Section 1.3) provided by AstraZeneca [113]. We use the model to study the changes in cancer cell populations over time in response to ceralasertib and olaparib.

2.2.1 Temporal Cell Population Dynamics: A Compartment Model

2.2.1.1 Modelling the Cell Cycle

The compartment model describes a population of asynchronous cancer cells progressing through the cell cycle. We study the growth of cancer cells in response to the DDR inhibitor drugs ceralasertib and olaparib, both of which are cell cycle-specific drugs. Hence, the model compartments represent cell cycle phase states. A schematic representation of the model is shown in Figure 2.1. The green nodes in Figure 2.1 represent undamaged cell cycle states, namely, the gap 1 (G1) state, the synthesis (S) state, and the combined gap 2/mitosis (G2/M) state. These states are taken from the biological cell cycle, where cells in the G1 phase prepare for DNA replication, which occurs in the S phase, and cells in the G2 phase prepare for cell division, which occurs in the M phase [91]. The red nodes in Figure 2.1 represent cells with DNA damage, which can occur during the S phase (SD) and the G2/M phase (G2D). Cells are at high risk of becoming DNA damaged during the DNA replication process (e.g., from DNA replication errors [13]). In the model, state SD represents cells with DNA replication stress [34], which is assumed to be mainly single-ended DSBs (seDSBs) from unrepaired SSBs. State G2D does not represent a specific type of DNA damage, but we assume that it will be mainly attributed to errors after DNA replication and unrepaired/incorrectly repaired DNA damage from state SD. The red cross in Figure 2.1 represents cell death via apoptosis, which

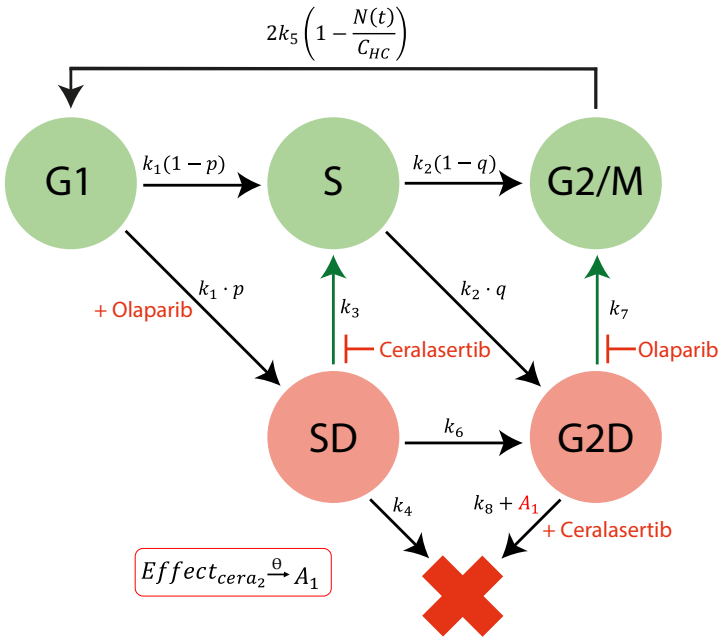

FIGURE 2.1: **The high-complexity compartment model (Model HC).** In Model HC, cells can be in undamaged and cycling cell cycle states (green nodes), damaged and non-cycling cell cycle states (red nodes), or a dead state (red cross). Cells can progress through the undamaged states (G1, S, and G2/M) and damaged states (SD and G2D). Cells in state SD experience DNA replication stress and cells in state G2D are cells with damage in the G2/M phase. Cells can die via apoptosis and progress to state D (red cross). The paths show the transitions between states where k_i, $i = 1, \ldots, 8$ are rate constants. p and q represent probabilities that a particular path will be chosen at a fork. $N(t) = [G1](t) + [S](t) + [SD](t) + [G2/M](t) + [G2D](t) + [D](t)$ is the total number of cells in the system (alive and dead) and C_{HC} is the carrying capacity. The green paths represent DNA damage repair, where ceralasertib inhibits repair of cells in state SD and olaparib inhibits the repair of cells in state G2D. Also, olaparib increases the number of cells that progress to state SD from state G1 and ceralasertib releases cells from state G2D to state D. A_1 is a time-dependent rate constant that represents delayed cell death caused by ceralasertib, where θ represents the delay time.

we call state D. Cells in state D remain there for the duration of the simulation and can no longer progress through the cell cycle [34].

Cells in the model progress through the compartments (i.e., the cell cycle states) via paths that are associated with rates. Cells leave state G1 at a rate of k_1 and enter the S phase with DNA damage (state SD) at a rate proportional to the probability p or without damage (state S) at a rate that is proportional to $1 - p$. Cells in state SD can be repaired at a rate k_3, which is represented by the transition from state SD to S. We assume that cells in state SD can directly enter state G2D at a rate k_6

because cells highly depend on the G2/M checkpoint after exposure to increased DNA damage during replication [137]. Ataxia-telangiectasia-mutated (ATM) is needed for homologous recombination repair (HRR) signalling and counteracting seDSB repair via non-homologous end-joining (NHEJ). When HRR is delayed due to ATM deficiency, more cells with seDSBs will be repaired via NHEJ, which can cause aberrant chromatid fusions and cell death [12, 113]. We assume that cells in the model are ATM-deficient and cells in state SD are cells with seDSBs. Hence, cells can transition from state SD to G2D because cells in state SD are likely to be repaired via NHEJ. If cells are not repaired from the SD state, they can be removed from the cell cycle and enter state D at a rate of k_4.

Cells leave the undamaged S state at a rate of k_2. However, damage can occur at any stage in the cell cycle, so we assume that cells can directly enter state G2D from the state S at a rate that is proportional to the probability q. Similarly, cells can transition from state S to G2/M at a rate that is proportional to $1-q$. Cells in state G2D can be repaired at a rate of k_7. The G2/M checkpoint is responsible for repairing any damaged cells before they enter mitosis [137, 166]. Therefore, in the model, the repair of cells in state G2D is represented by the transition from state G2D to G2/M. If cells in state G2D are not repaired, we assume that cells can die via mitotic catastrophe [113, 34, 29]. Hence, in the absence of drugs, cells in the model can be removed from the system and progress to state D at a rate of k_8.

To incorporate the in vitro scenario where the growth is limited by space availability, the cells in the model divide at a rate k_5 that is proportional to a logistic growth rate, $\left(1-\frac{N(t)}{C_{HC}}\right)$. Here, k_5 is the rate of cells leaving state G2/M, $N(t) = [G1](t) + [S](t) + [SD](t) + [G2/M](t) + [G2D](t) + [D](t)$ is the total number of cells in the system (alive and dead), and C_{HC} is the carrying capacity [126]. We assume that dead cells are not removed from the system in the time frame of interest so they still take up space. Also, we assume that dead cells represent cell debris from cells that are dying and therefore do not contribute to the cell confluency.

Following Figure 2.1, the mathematical model is described by a system of ODEs, where each dependent variable $[y]$ represents the number of cells in compartment y. The mathematical model for the case with no drug treatment can be written as equations (2.1a)-(2.1f):

$$\frac{d[G1](t)}{dt} = 2k_5\left(1 - \frac{N(t)}{C_{HC}}\right)[G2/M](t) - k_1[G1](t), \tag{2.1a}$$

$$\frac{d[S](t)}{dt} = k_1(1-p)[G1](t) - k_2[S](t) + k_3[SD](t), \tag{2.1b}$$

$$\frac{d[G2/M](t)}{dt} = k_2(1-q)[S](t) - k_5\left(1 - \frac{N(t)}{C_{HC}}\right)[G2/M](t) + k_7[G2D](t), \tag{2.1c}$$

$$\frac{d[SD](t)}{dt} = k_1 p[G1](t) - k_3[SD](t) - k_6[SD](t) - k_4[SD](t), \tag{2.1d}$$

$$\frac{d[G2D](t)}{dt} = k_2 q[S](t) + k_6[SD](t) - k_7[G2D](t) - k_8[G2D](t), \tag{2.1e}$$

$$\frac{d[D](t)}{dt} = k_4[SD](t) + k_8[G2D](t). \tag{2.1f}$$

2.2.1.2 Modelling the Effects of Ceralasertib

ATR is involved in promoting the repair of seDSBs via homologous recombination repair (HRR) and for stabilising and restarting stalled replication forks [113]. Furthermore, ATR is significant for activating the intra-S checkpoint which is responsible for arresting damaged cells in the S phase and delaying the replication process [113, 137]. Ceralasertib is an ATR inhibitor drug that dose-dependently inhibits the repair of replication damage. In the model, this repair is represented by the transition to state S from state SD, thus, increasing doses of ceralasertib decreases the value of k_3 [34].

In the in vitro experiments, treatment with ceralasertib resulted in abrogation of the G2/M checkpoint, which is responsible for preventing damaged cells from entering mitosis [69]. Thus, ceralasertib releases cells from G2 arrest, which forces them to undergo mitotic catastrophe [34, 113]. However, drug effects are not always instantaneous. The combination of ceralasertib and olaparib could allow for shorter

treatment times as it induces cell death in ATM-deficient cell lines within one to two cell divisions [113]. Here, we assume that ceralasertib induces cell death from state G2D. Furthermore, to incorporate the delay observed in the drug-induced cell death, we introduce a transit compartment into the model to represent death delay [126, 114, 127]. A_1 represents a time-dependent rate at which cells leave state G2D (equation 2.3e), where θ represents the time spent in the delay. The value of A_1 increases over time to represent delayed death, as can be observed in Figure 2.2. Although more than one transit compartment can be used without adding any extra parameters, experimental data only warrants one transit compartment which is implemented in this model (See Appendix A.1.1 for more details).

In the model, we include the drug effects using the sigmoid Emax equation which is a modification of the Hill equation [80] and can be used to describe the relationship between drug dose and effect over time, i.e., the concentration-effect relationship [146, 66]. This equation illustrates that the drug effect increases with higher drug

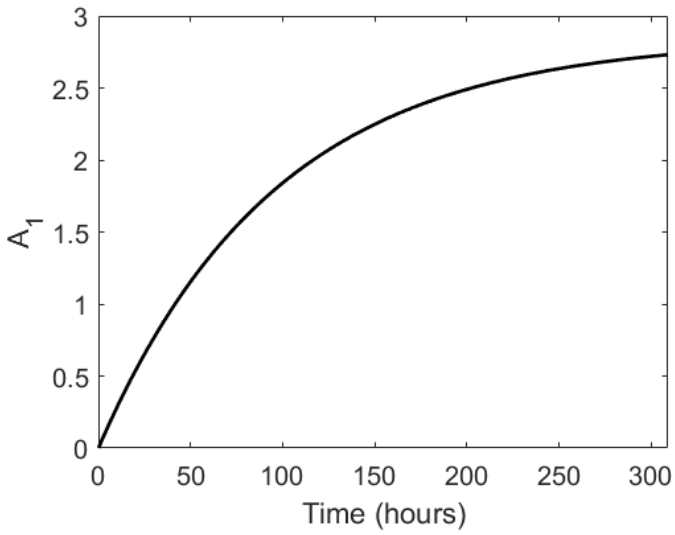

FIGURE 2.2: **Drug-related cell death is not always instantaneous, thus, we introduce a transit compartment into the compartment model to represent death delay.** A_1 is a time-dependent rate at which cells transition from state G2D to state D (vertical axis). The value of A_1 increases over the time course of the experiment (horizontal axis). This represents ceralasertib-related death delay. In this example, A_1 is calculated via equation 2.3e with 0.3 μM ceralasertib.

concentrations, as shown in Figure 2.3. Ceralasertib drug effects are included using the sigmoid Emax equation [67] and are given by:

$$\text{Effect}_{\text{Cera},1} = I_{\text{max,C}} \cdot \left(\frac{ATRi^{h_{C,1}}}{IC_{50,\text{C}}^{h_{C,1}} + ATRi^{h_{C,1}}} \right), \tag{2.2a}$$

$$\text{Effect}_{\text{Cera},2} = K_{\text{max,C}} \cdot \left(\frac{ATRi^{h_{C,2}}}{KC_{50,\text{C}}^{h_{C,2}} + ATRi^{h_{C,2}}} \right). \tag{2.2b}$$

$ATRi$ represents the concentration of the ATR inhibitor drug, ceralasertib. $I_{\text{max,C}}$ and $K_{\text{max,C}}$ represent the maximal inhibitory effect and the maximal killing effect of ceralasertib respectively. $IC_{50,\text{C}}$ and $KC_{50,\text{C}}$ represent the concentration of ceralasertib resulting in half the maximal inhibitory effect and half the maximal killing effect respectively, and lastly $h_{C,1}$ and $h_{C,2}$ represent the Hill coefficients.

The updated equations, incorporating the effects of ceralasertib are given by:

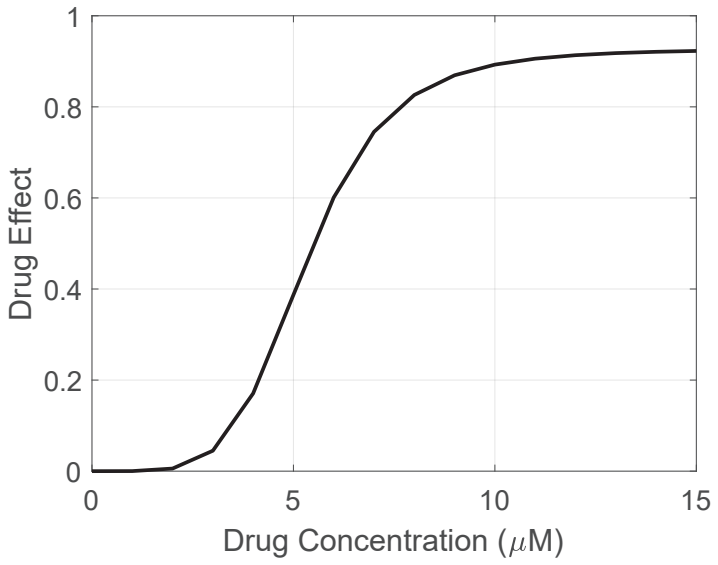

FIGURE 2.3: **The concentration-effect relationship illustrated by the sigmoid Emax Equation.** Here, we use the parameter values from Equation 2.2a given in Table 2.3.

$$\frac{d[S](t)}{dt} = k_1(1-p)[G1](t) - k_2[S](t) + k_3(1 - \text{Effect}_{\text{Cera},1})[SD](t), \tag{2.3a}$$

$$\frac{d[SD](t)}{dt} = k_1 p[G1](t) - k_3(1 - \text{Effect}_{\text{Cera},1})[SD](t) - k_6[SD](t) - k_4[SD](t), \tag{2.3b}$$

$$\frac{d[G2D](t)}{dt} = k_2 q[S](t) + k_6[SD](t) - k_7[G2D](t) - k_8[G2D](t) - [A_1](t)[G2D](t), \tag{2.3c}$$

$$\frac{d[D](t)}{dt} = k_4[SD](t) + k_8[G2D](t) + [A_1](t)[G2D](t), \tag{2.3d}$$

$$\frac{d[A_1](t)}{dt} = \frac{1}{\theta}(\text{Effect}_{\text{Cera},2} - [A_1](t)). \tag{2.3e}$$

2.2.1.3 Modelling the Effects of Olaparib

Olaparib is an S phase-dependent drug [113]. Olaparib treatment inhibits the repair of SSBs, which can collide with the replication fork and generate seDSBs [113, 83, 137, 130, 12]. Hence, when olaparib treatment is added to the model, we assume that more cells will enter state SD rather than state S. Thus, olaparib dose-dependently increases the value of the probability p.

It has been observed that when olaparib is given, there is an increased accumulation of cells in the G2 phase due to cell cycle arrest [113]. Note that G2 accumulation after olaparib treatment was also found in other cell lines [95]. We have incorporated this into the model by assuming that the repair of cells in state G2D will be dose-dependently inhibited by olaparib treatment.

Here, these olaparib drug effects are modelled using the sigmoid Emax equation [67] and are given by:

$$\text{Effect}_{\text{Ola},1} = E_{\max,\text{O}} \cdot \left(\frac{PARPi^{h_{O,1}}}{EC_{50,\text{O}}^{h_{O,1}} + PARPi^{h_{O,1}}} \right), \tag{2.4a}$$

$$\text{Effect}_{\text{Ola},2} = I_{\max,\text{O}} \cdot \left(\frac{PARPi^{h_{O,2}}}{IC_{50,\text{O}}^{h_{O,2}} + PARPi^{h_{O,2}}} \right). \tag{2.4b}$$

$PARPi$ represents the concentration of the PARP inhibitor drug, olaparib. $E_{\max,\text{O}}$ and $I_{\max,\text{O}}$ represent the maximal effect and the maximal inhibitory effect of olaparib respectively. $EC_{50,\text{O}}$ and $IC_{50,\text{O}}$ represent the concentration of olaparib resulting in half the maximal effect and half the maximal inhibitory effect respectively, and lastly $h_{O,1}$ and $h_{O,2}$ represent the Hill coefficients.

The updated equations, incorporating the effects of olaparib are given by:

$$\frac{d[S](t)}{dt} = k_1(1 - p(1 + \text{Effect}_{\text{Ola},1}))[G1](t) - k_2[S](t) + k_3[SD](t), \tag{2.5a}$$

$$\begin{aligned}\frac{d[G2/M](t)}{dt} =& k_2(1-q)[S](t) - k_5\left(1 - \frac{N(t)}{C_{HC}}\right)[G2/M](t) \\ &+ k_7(1 - \text{Effect}_{\text{Ola},2})[G2D](t),\end{aligned} \tag{2.5b}$$

$$\begin{aligned}\frac{d[SD](t)}{dt} =& k_1 p(1 + \text{Effect}_{\text{Ola},1})[G1](t) - k_3[SD](t) - k_6[SD](t) \\ &- k_4[SD](t),\end{aligned} \tag{2.5c}$$

$$\begin{aligned}\frac{d[G2D](t)}{dt} =& k_2 q[S](t) + k_6[SD](t) - k_7(1 - \text{Effect}_{\text{Ola},2})[G2D](t) \\ &- k_8[G2D](t).\end{aligned} \tag{2.5d}$$

2.2.1.4 Modelling the Effects of Both Ceralasertib and Olaparib

The drug effects are modelled by:

$$\text{Effect}_{\text{Cera},1} = I_{\max,\text{C}} \cdot \left(\frac{ATRi^{h_{C,1}}}{IC_{50,\text{C}}^{h_{C,1}} + ATRi^{h_{C,1}}} \right), \tag{2.6a}$$

$$\text{Effect}_{\text{Cera},2} = K_{\max,\text{C}} \cdot \left(\frac{ATRi^{h_{C,2}}}{KC_{50,\text{C}}^{h_{C,2}} + ATRi^{h_{C,2}}} \right), \tag{2.6b}$$

$$\text{Effect}_{\text{Ola},1} = E_{\max,\text{O}} \cdot \left(\frac{PARPi^{h_{O,1}}}{EC_{50,\text{O}}^{h_{O,1}} + PARPi^{h_{O,1}}} \right), \tag{2.6c}$$

$$\text{Effect}_{\text{Ola},2} = I_{\max,\text{O}} \cdot \left(\frac{PARPi^{h_{O,2}}}{IC_{50,\text{O}}^{h_{O,2}} + PARPi^{h_{O,2}}} \right). \tag{2.6d}$$

Combining the effects of ceralasertib and olaparib, the mathematical model can be written as:

$$\frac{d[G1](t)}{dt} = 2k_5 \left(1 - \frac{N(t)}{C_{HC}}\right)[G2/M](t) - k_1[G1](t), \tag{2.7a}$$

$$\begin{aligned}\frac{d[S](t)}{dt} =& k_1(1 - p(1 + \text{Effect}_{\text{Ola},1}))[G1](t) - k_2[S](t) \\ &+ k_3(1 - \text{Effect}_{\text{Cera},1})[SD](t),\end{aligned} \tag{2.7b}$$

$$\begin{aligned}\frac{d[G2/M](t)}{dt} =& k_2(1-q)[S](t) - k_5\left(1 - \frac{N(t)}{C_{HC}}\right)[G2/M](t) \\ &+ k_7(1 - \text{Effect}_{\text{Ola},2})[G2D](t),\end{aligned} \tag{2.7c}$$

$$\begin{aligned}\frac{d[SD](t)}{dt} =& k_1 p(1 + \text{Effect}_{\text{Ola},1})[G1](t) - k_3(1 - \text{Effect}_{\text{Cera},1})[SD](t) \\ &- k_6[SD](t) - k_4[SD](t),\end{aligned} \tag{2.7d}$$

$$\begin{aligned}\frac{d[G2D](t)}{dt} =& k_2 q[S](t) + k_6[SD](t) - k_7(1 - \text{Effect}_{\text{Ola},2})[G2D](t) \\ &- k_8[G2D](t) - [A_1](t)[G2D](t),\end{aligned} \tag{2.7e}$$

$$\frac{d[D](t)}{dt} = k_4[SD](t) + k_8[G2D](t) + [A_1](t)[G2D](t), \tag{2.7f}$$

$$\frac{d[A_1](t)}{dt} = \frac{1}{\theta}(\text{Effect}_{\text{Cera},2} - [A_1](t)). \tag{2.7g}$$

We also define the total number of cells that are:

$$\text{in S phase} : [S_{\text{tot}}](t) = [S](t) + [SD](t), \tag{2.8a}$$

$$\text{in G2/M phase} : [G2/M_{\text{tot}}](t) = [G2/M](t) + [G2D](t), \tag{2.8b}$$

$$\text{damaged} = [SD](t) + [G2D](t), \tag{2.8c}$$

$$\text{alive} = [G1](t) + [S](t) + [SD](t) + [G2/M](t) + [G2D](t). \tag{2.8d}$$

2.2.2 Model Parameterisation

Here, we assume that all cells are ATM-deficient and that they do not change in size/volume throughout the duration of the in silcio experiments. In line with the experimental data, the model simulations start with an initial cell population of 1500 cells, and the full dose of the drugs are given at the start of the in silico experiments. Since we are studying the case of in vitro cells, we assume that the drug concentration is constant throughout the time course of our simulations (up to 310 hours) and no drug elimination or decay happens during this time [76].

2.2.2.1 Initial Conditions

The initial conditions of the compartments are obtained from EdU pulse-chase experiments (Section 1.3) [113]. These experiments measure the percentage of cells in phases G1, S, and G2/M, as well as cells that are γH2AX positive, a marker of DNA damage [163]. We assume that cells in state SD are γH2AX positive because cells in state SD have DNA replication stress. The initial fraction of cells in state G2D is approximated to be the remaining fraction. We start with zero cells in the death compartment [34]. Note that the initial concentration in the transit compartment is $A_1(0) = 0$. The initial fraction of cells in G1, S, G2/M, SD and G2D are given in Table 2.1.

2.2.2.2 Model Parameters

The model parameters are estimated using the lsqnonlin function, a local non-linear least squares method in MATLAB [108]. Using this method, we minimise the sum of squares of the residuals between the model output, i.e., the total number of cells in the system, and the in vitro mean cell confluency data, which was measured

Parameter Name	Parameter Value	Parameter Description
$G1_0$	0.458	The fraction of cells in state G1 at the start of the simulation.
S_0	0.133	The fraction of cells in state S at the start of the simulation.
SD_0	0.0157	The fraction of cells in state SD at the start of the simulation.
$G2/M_0$	0.0023	The fraction of cells in state G2/M at the start of the simulation.
$G2D_0$	0.391	The fraction of cells in state G2D at the start of the simulation.
D_0	0	The fraction of cells in state D at the start of the simulation.

TABLE 2.1: **Initial conditions are estimated from in vitro experimental data 1.** The initial fraction of cells in states G1, S, SD, G2D, and G2/M are estimated from pulse-chase data. At the start of the simulations, no cells are in the dead state (D).

approximately every 3 hours for 310 hours. Note that the in vitro data may be noisy, however, we use the mean from three experimental repeats to measure the residuals as a single value for each time point. In the in vitro data, we also have the standard error of the mean (SEM) given by [107]:

$$\text{SEM} = \frac{\text{standard deviation}}{\sqrt{\text{sample size}}}. \tag{2.9}$$

Here, estimations are done using a part of the data (namely, all data except mono- and combination therapies including 0.3 μM olaparib). The estimated parameters (given in Tables 2.2 and 2.3) are then used to compare the results of other combinations that are not used in the calibration process. Appropriate sensitivity analyses are performed to study these estimated parameters in Chapter 3.

To ensure a positive number of cells, we set the lower bounds of all parameters to be zero and the upper bounds of $I_{\max,C}$ and $I_{\max,O}$ to be one. Both probability constants p and q are bounded between zero and one. Following the experimental data and the assumption that cells stay the same size throughout the experiment, the carrying capacity, C_{HC}, was estimated to be less than 100,000. To avoid cells staying in the death delay for a prolonged amount of time, θ was bounded at 4 days. Consistent with the upper bounds used in the model by Checkley *et al.* [34], all rate constants

k_i, $i = 1, 2, \ldots, 8$ are bounded at 1.0e+06 and all hill coefficients ($h_{O,1}$, $h_{O,2}$, $h_{C,1}$, and $h_{C,2}$) are bounded at 100. To ensure a biologically relevant concentration of each drug, we bounded $EC_{50,O}$, $IC_{50,O}$, $IC_{50,C}$, and $KC_{50,C}$ at 100. $K_{\max,C}$ and $E_{\max,O}$ are bounded between zero and infinity.

Parameter Name	**Parameter Value**	**Parameter Description**
k_1	0.050779 (1/hour)	The rate at which cells leave state G1.
k_2	0.17906 (1/hour)	The rate at which cells leave state S.
k_3	0.39181 (1/hour)	The rate at which cells leave state SD and enter state S.
k_4	1.1443 (1/hour)	The rate at which cells leave state SD and enter state D.
k_5	0.060188 (1/hour)	The rate at which cells leave state G2/M.
k_6	0.32358 (1/hour)	The rate at which cells leave state SD and enter state G2D.
k_7	2.1526 (1/hour)	The rate at which cells leave state G2D and enter G2/M.
k_8	0.0010523 (1/hour)	The rate at which cells leave state G2D and enter state D.
p	0.14826	The probability that cells transition from state G1 to SD.
q	0.45458	The probability that cells transition from state S to G2D.
C_{HC}	13727.7261 (cells/A)	The carrying capacity in the compartment model (Model HC).
θ	95.9914 hours	The transit step time.

TABLE 2.2: **Parameter values are estimated from in vitro experimental data 1.** The table displays the parameter values that are used in the compartment model (Model HC). A denotes the area of the spatial domain in the in vitro experiment

Parameter Name	Parameter Value	Parameter Description
$I_{\max,C}$	0.92714	The maximal drug effect of ceralasertib inhibiting the repair of cells in state SD.
$IC_{50,C}$	5.3318 μM	The concentration of ceralasertib that results in half of $I_{\max,C}$.
$h_{C,1}$	5.1795	The Hill coefficient of ceralasertib inhibiting the repair of cells in state SD.
$K_{\max,C}$	2.8866	The maximal drug effect of ceralasertib killing cells from state G2D.
$KC_{50,C}$	0.14143 μM	The concentration of ceralasertib that results in half of $K_{\max.C}$, i.e., the sensitivity constant.
$h_{C,2}$	5.6103	The Hill coefficient of ceralasertib-related cell death.
$E_{\max,O}$	1.9721	The maximal drug effect of olaparib increasing p.
$EC_{50,O}$	0.15942 μM	The concentration of olaparib that results in half of $E_{\max,O}$.
$h_{O,1}$	0.40941	The Hill coefficient of olaparib increasing p.
$I_{\max,O}$	1	The maximal drug effect of olaparib inhibiting repair of cells in state G2D.
$IC_{50,O}$	0.041212 μM	The concentration of olaparib that results in half of $I_{\max,O}$.
$h_{O,2}$	0.10945	The Hill coefficient of olaparib inhibiting repair of cells in state G2D.

TABLE 2.3: **Drug-related parameter values are estimated from in vitro experimental data 1.** The table displays the drug-related parameter values that are used in the compartment model (Model HC).

2.3 Results

2.3.1 Model Analysis: Insight Into Drug Interactions

The synergy between ATR and PARP inhibitor drugs in ATM-deficient cancers was proposed by Lloyd *et al.* [113]. Both ceralasertib and olaparib exert their effects in targeting DDR pathways at multiple points of the cell cycle [113]. Motivated by this, the developed model incorporates the effects of these drugs at multiple points. By removing each drug effect one at a time, we can investigate which drug effects have the greatest impact on the growth of the cancer cell population.

We studied Model HC described in Section 2.2.1 against four alternative model versions (labelled Version 1-4, Figure 2.4), each without an individual drug effect. To compare the models, the model goodness of fit is assessed for each drug treatment j using the root mean square error (RMSE), which is given by

$$\text{RMSE}_j = \sqrt{\frac{\sum_{k=1}^{\eta} (y_{j,k} - f_j(t_k))^2}{\eta}}. \tag{2.10}$$

Here, the RMSE is calculated at each of the η experimental data time points, where $y_{j,k}$ are the experimental cell confluency data points for treatment j at the corresponding time points t_k and $f_j(t_k)$ are the simulation cell confluency values at times t_k for treatment j, calculated by:

$$f_j(t_k) = 100 \cdot \frac{[G1](t_k) + [S](t_k) + [G2/M](t_k) + [SD](t_k) + [G2D](t_k)}{C_{HC}}. \tag{2.11}$$

Note that the in vitro data may be noisy and $y_{j,k}$ is equal to the mean from three experimental repeats, so we measure the RMSE as a single value for each time point. Further, the total RMSE of each model is calculated for all drug treatments together is calculated by:

$$\text{Total RMSE} = \sqrt{\frac{\sum_{j=1}^{9}\sum_{k=1}^{\eta}(y_{j,k} - f_j(t_k))^2}{\eta}}. \tag{2.12}$$

Figure 2.4 shows Model HC and the four model variations that we test to estimate the cell confluency data. Columns 1-5 in Figure 2.4 show: (1) Model HC which includes all of the drug effects, (2) Model version 1, which is Model HC without olaparib increasing the number of cells that progress to state SD, (3) Model version 2, which is Model HC without olaparib inhibiting the repair of cells from state G2D, (4) Model version 3, which is Model HC without ceralasertib inhibiting the repair of cells from state SD, and (5) Model version 4, which is Model HC without ceralasertib-related cell death. Each model is parameterised using the non-linear least squares function lsqnonlin on MATLAB using a part of the data with the parameter bounds given in Section 2.2.2 [108]. The parameter values of each of these models are given in Table 2.4.

By observing the middle and bottom rows in Figure 2.4, we see that for different sets of parameter values, each of the model versions provides a qualitatively good comparison with the experimental data. This shows that one could further simplify the developed model (Model HC) by omitting some of the detailed drug actions. This will potentially leave the other actions more prominent. Version 2 and Version 4 of the model have the highest RMSE (the value underneath each schematic in Figure 2.4), which means that omitting these drug effects significantly impacts the growth of the simulated cancer cell population. This illustrates the importance of both the influence of olaparib inhibiting the repair of cells in state G2D and the transit compartment introduced for ceralasertib-specific death delay.

For each of the five models, the model goodness of fit is assessed for each drug treatment separately using the RMSE (equation 2.10; Figure 2.5). In this figure, the values on the y axis refer to the normalised cell confluency percentages that are summed over all of the data time points. A normalised RMSE value close to zero

means that the model provides a better fit to the in vitro data at each time point, whereas, an RMSE value close to one means the model provides a worse fit to the in vitro data over the time course of the experiments. By comparing the individual treatment RMSE values for each of the five models (Figure 2.5), it is hard to deduce which model best fits the data since different models fit different treatments better.

In summary, all five models are able to satisfactorily predict the unseen time series data. However, since Model HC gives the lowest total RMSE among all the models (12.2405), we argue that Model HC is the most appropriate model to study cell population dynamics in response to 0.1-0.3 μM ceralasertib and 0.03-0.3 μM olaparib.

Parameter	**Model HC**	**Version 1**	**Version 2**	**Version 3**	**Version 4**
k_1	0.050779	0.050776	0.055148	0.050001	0.08564
k_2	0.17906	0.6567	0.18401	0.17135	0.041513
k_3	0.39181	0.0093758	1.2473	0.41375	1.3673
k_4	1.1443	0.0054583	0.57106	0.21322	0.29128
k_5	0.060188	0.062766	0.097768	0.069557	0.074812
k_6	0.32358	0.43111	1.7469	0.41388	0.49978
k_7	2.1526	1.5779	1.4393	2.3031	1324.0654
k_8	0.0010523	0.25615	0.27765	0.10024	0.00011566
p	0.14826	0.54072	0.41088	0.40579	0.7596
q	0.45458	0.38494	0.30325	0.37705	0.75154
C_{HC}	13727.7261	15830.6007	17010.369	14755.5444	12589.3397
θ	95.9914	95.9161	50.2541	95.9936	n/a
$I_{\max,C}$	0.92714	0.95138	0.9984	n/a	1
$IC_{50,C}$	5.3318	0.71927	2.8783e-05	n/a	0.10004
$h_{C,1}$	5.1795	39.9005	2.1978	n/a	11.7832
$K_{\max,C}$	2.8866	1.2788	0.99065	2.847	n/a
$KC_{50,C}$	0.14143	0.12936	0.20345	0.13427	n/a
$h_{C,2}$	5.6103	6.3084	6.2309	6.2307	n/a
$E_{\max,O}$	1.9721	n/a	1.1057	1.3047	1.4611
$EC_{50,O}$	0.15942	n/a	0.15741	0.099947	0.14802
$h_{O,1}$	0.40941	n/a	0.40721	0.35009	0.39859
$I_{\max,O}$	1	1	n/a	1	0.9635
$IC_{50,O}$	0.041212	0.09522	n/a	0.1044	2.4554
$h_{O,2}$	0.10945	0.25487	n/a	0.27817	4.2192

TABLE 2.4: **Parameter values for all model variations are estimated from in vitro experimental data 1.** The table displays the parameter values that are used in the compartment models (Model HC and Versions 1-4).

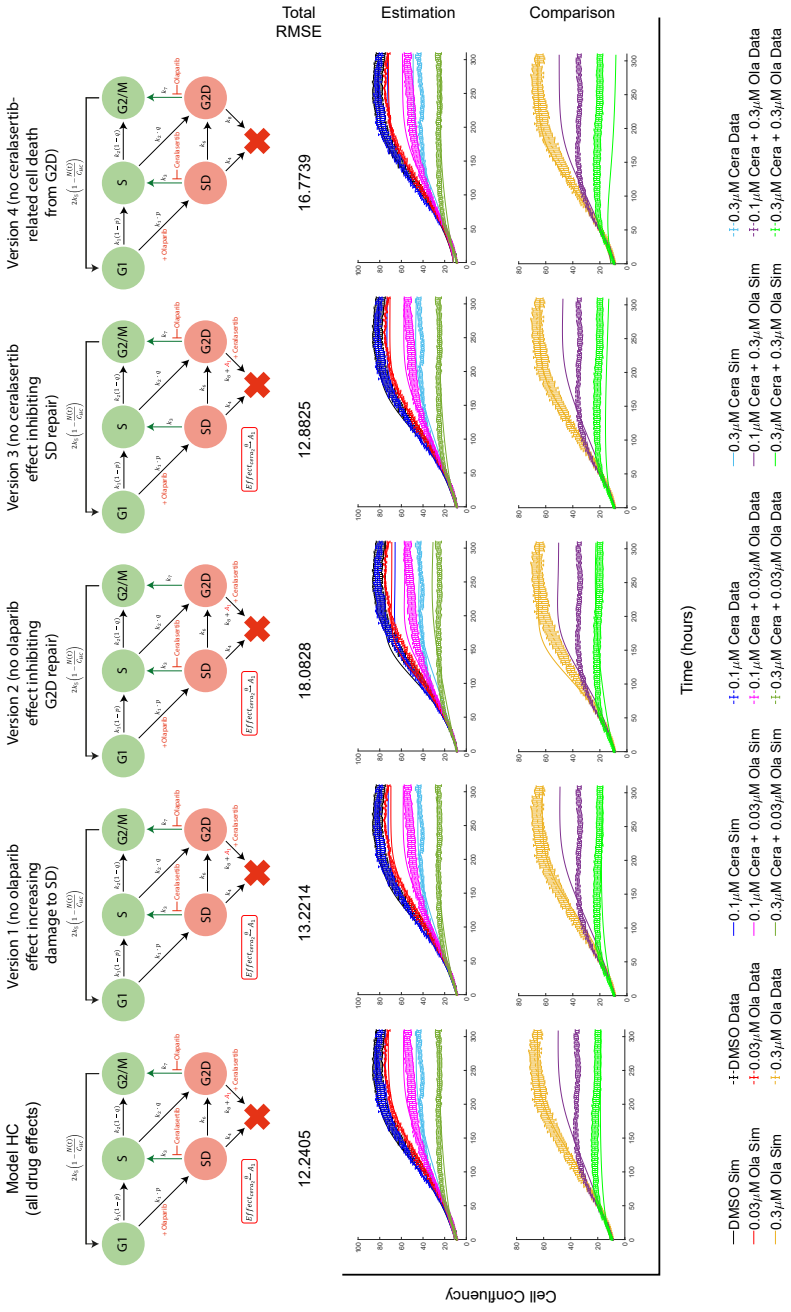

FIGURE 2.4: **Mathematical models can give insight into drug interactions.** The figure shows five variations of Model HC to study the role of ceralasertib and olaparib at multiple points of action. The plots show the model schematic (top row) and the simulated and experimental cell confluency over 310 hours for various dose combinations of ceralasertib and olaparib. The five models are parameterised and evaluated against experimental data 1. Training data is used to estimate model parameters (middle row) and test data is used to evaluate the model (bottom row). The solid curves represent the simulation results from the compartment models. The dashed curves represent the mean in vitro data, with the standard error of the mean for 3 experiments indicated with error bars. The total RMSE value is given underneath the model schematic for each model version calculated via equation 2.12.

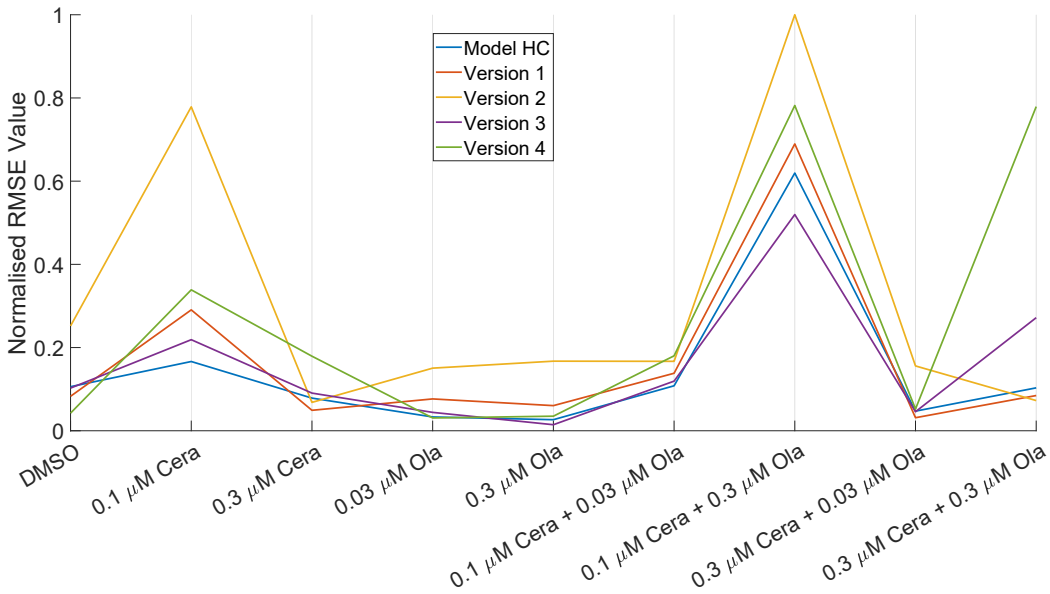

FIGURE 2.5: **The RMSE value calculates how well the mathematical models fit experimental data 1.** For each of the model variations (with and without certain drug effects), the RMSE values for each drug treatment are calculated via equation 2.10 for each of the nine treatments. Here, the horizontal axis represents different treatment combinations and the vertical axis represents the corresponding RMSE value normalised by dividing each by the maximum RMSE value.

2.3.2 Model Calibration and Parameter Estimation

The model is first calibrated using a part of the in vitro experimental data provided by AstraZeneca (Section 1.3) [113] using the non-linear least squares method on MATLAB (Section 2.2.2) [108]. Populations of FaDu ATM-KO cells were exposed to both the ATR inhibitor drug ceralasertib and the PARP inhibitor drug olaparib, both as monotherapies and combination therapies.

Both the simulated and experimental cell confluency for the drug treatments used to train the model are shown in Figure 2.6. We can see from this figure that Model HC is capable of capturing the cell confluency data throughout the time course of the experiment. Thus, in agreement with the experimental data, the model indicates that the combination of the drugs requires lower doses and shorter treatment periods to induce growth inhibition and death of cancer cells.

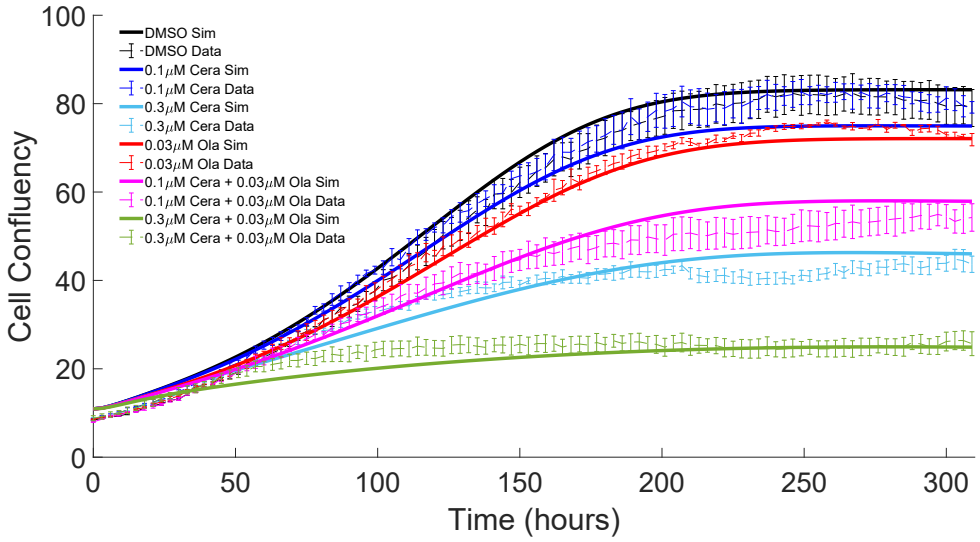

FIGURE 2.6: **The compartment model (Model HC) is parameterised by in vitro experimental data 1.** The plots show simulated and experimental cell confluency over 310 hours for various dose combinations of ceralasertib and olaparib used to parameterise and train the model. The solid curves represent the simulation results from the compartment model (Model HC). The dashed curves represent the mean in vitro data, with the standard error of the mean for 3 experiments indicated with error bars.

2.3.3 Model Analysis: Comparing In Silico and In Vitro Results

2.3.3.1 Model Analysis: Cell Confluency Data

Here, we use the model together with the estimated parameters to simulate the effects of 0.3 μM olaparib and both combinations using this dose (0.1 μM ceralasertib + 0.3 μM olaparib and 0.3 μM ceralasertib + 0.3 μM olaparib). The in silico results are compared with the experimental data to study the performance of the model to simulate the effects of drug combinations that were not previously used in the estimation process. Figure 2.7 shows the in silico and in vitro comparisons of the cell confluency over 310 hours for the doses not included in our parameter optimisation. The model is able to satisfactorily capture the trends of the unseen time series data (Figure 2.7). We note that the fit of the purple curve in Figure 2.7 (0.1 μM ceralasertib + 0.3 μM olaparib) is not as good as other unseen data. As with any biological experiments, we do not expect an accurate prediction for every combination due

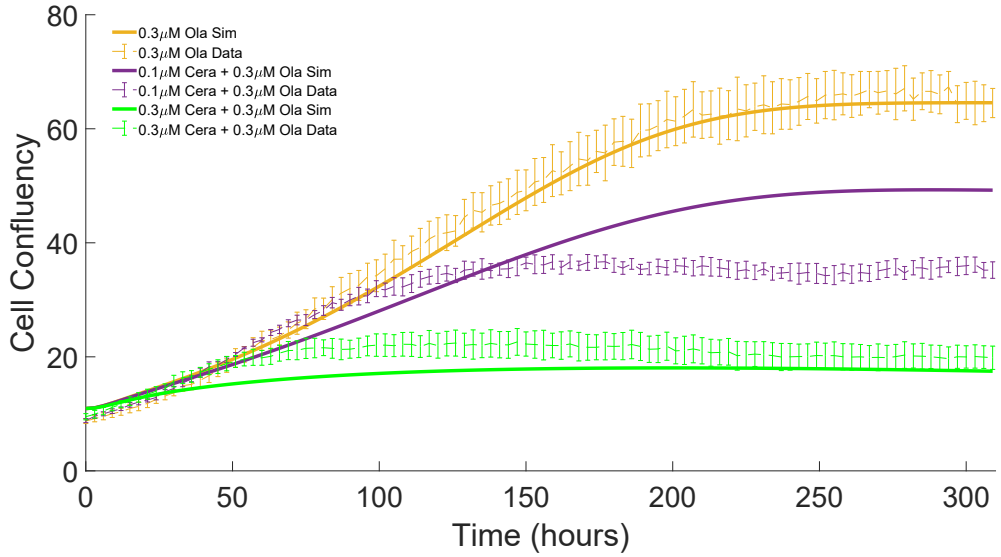

FIGURE 2.7: **The compartment model (Model HC) is evaluated against in vitro experimental data 1.** The plots show simulated and experimental cell confluency over 310 hours for various dose combinations of ceralasertib and olaparib used to evaluate and test the model. The solid curves represent the simulation results from the compartment model (Model HC). The dashed curves represent the mean in vitro data, with the standard error of the mean for 3 experiments indicated with error bars.

to the inherent complexity. It might also be due to the strong synergistic effects of these combinations, which the model failed to capture. However, although we are unable to fit one combination, we believe that the model is able to predict the overall data well.

Overall, from both the estimation and comparison results, we conclude that the combination therapies result in a lower cell confluence throughout the experiments meaning there is more growth inhibition and cell death of cancer cells. Since the compartment model (Figure 2.1) is able to satisfactorily predict unseen time series data, we argue that Model HC is appropriate for our current study which aims at modelling cell population dynamics in response to 0.1-0.3 μM ceralasertib doses and 0.03-0.3 μM olaparib doses.

2.3.3.2 Model Analysis: Cell Death Data

Here, we qualitatively compare the in silico results of cell death to the experimental data provided by AstraZeneca that was measured using caspase 3/7 intensity (Section 1.3) [113]. The experimental data shows how growth inhibition correlates with apoptotic activity. Caspase 3/7 activity was detected earlier (within 36 hours) after combination treatment, which implies that apoptosis is the main reason for growth inhibition. As for single-agent treatment, caspase 3/7 activity was seen at later time points, implying multiple rounds of cell division and/or prolonged drug exposure were needed to produce cancer growth inhibition [113].

The experimental data shows the cells stained with caspase 3/7 at each time point, which means that the experimental data is not cumulative compared to the in silico model. Therefore, both the data and simulation cell death values have been normalised between zero and one for ease of comparison. The details of caspase 3/7 and cytotox markers were not incorporated into the model, so we cannot quantitatively compare our in silico results to the in vitro data. Instead, we show that the mathematical model can qualitatively show the same trend as the experimental data.

The normalised apoptosis activity from the experimental data (left column) and from the in silico simulations (right column) are displayed in Figure 2.8. Although the model slightly underestimates the amount of cell death after treatment with 0.1 μM ceralasertib (the data suggests a value of 0.6, whereas the simulation gives a value of roughly 0.45), overall, the model is capable of capturing the qualitative trends of apoptosis (Figure 2.8).

2.3.4 Model Analysis: Investigating Combination Therapy

Cancer is often targeted with multimodality treatments and here, we study the effects of two DDR inhibitor drugs which are given in combination. When such combinations are used to target cancer cells, it is useful to study their optimal

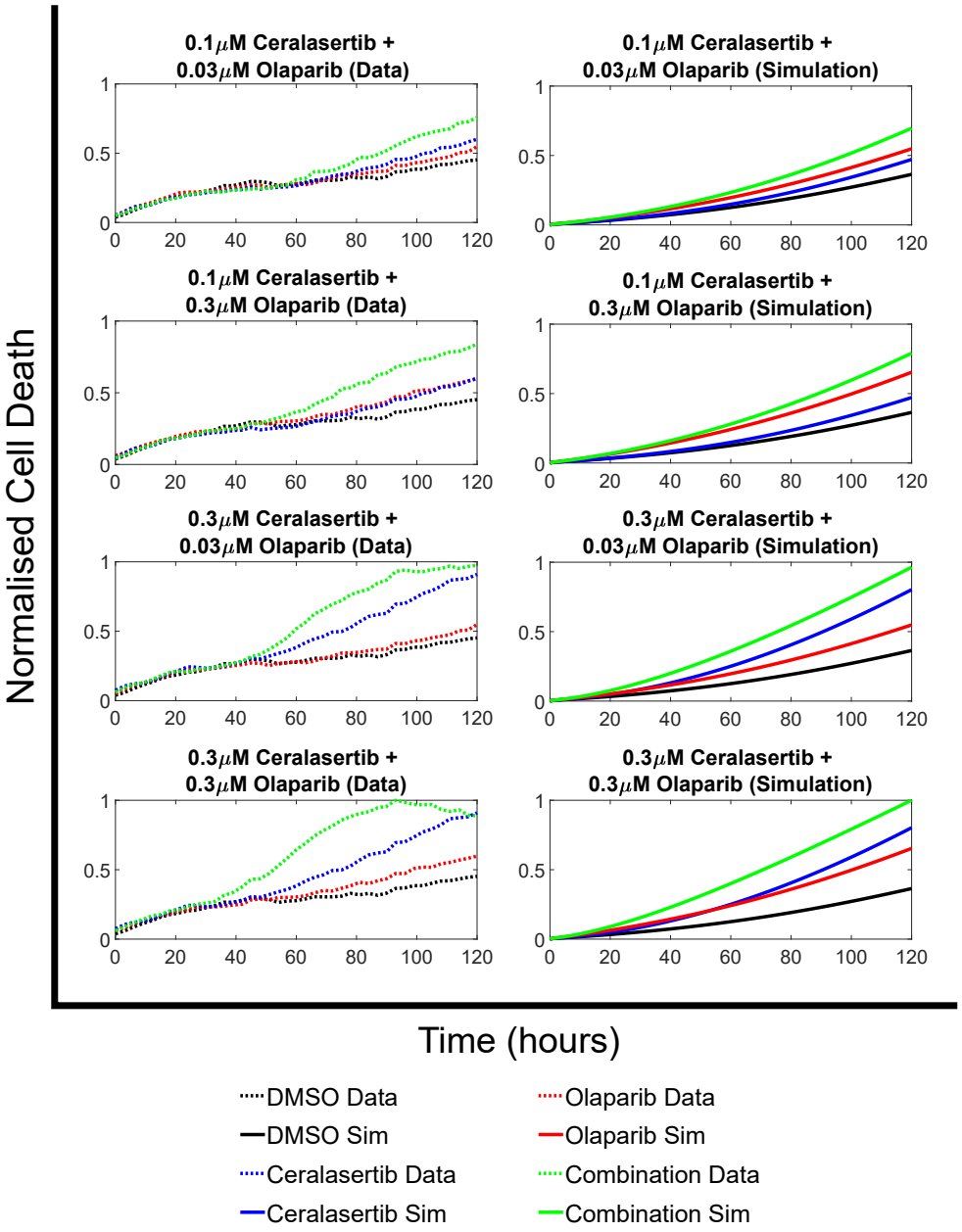

FIGURE 2.8: **The compartment model (Model HC) is evaluated against in vitro cell death data from experimental data 1.** The plots show experimental cell death (left panel) measured by caspase 3/7 intensity and simulated total cell death (right panel) for 310 hours for various dose combinations of ceralasertib and olaparib. All output values are normalised between zero and one for ease of comparison. Each plot shows a different combination dose for each drug treatment: no drug treatment (black), olaparib monotherapy (red), ceralasertib monotherapy (blue), and combination therapy (green).

combinations, dosage, and scheduling to maximise their effects. Here, we use the developed mathematical model, which is calibrated with experimental data

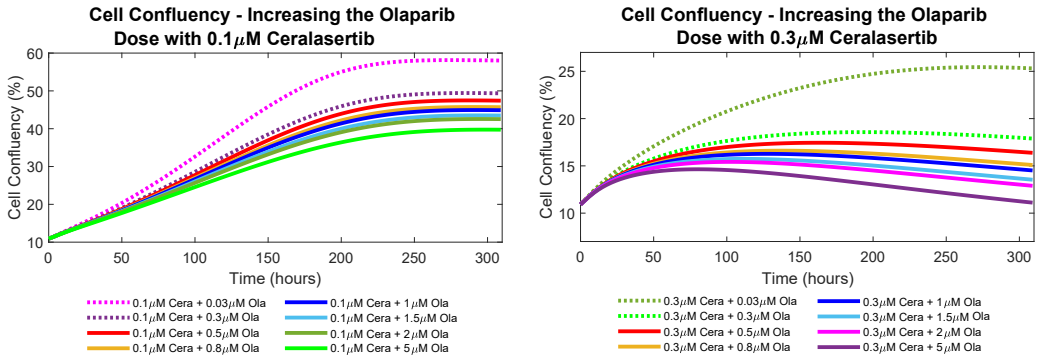

FIGURE 2.9: **Model MC is used to investigate optimal doses of drug combinations.** The plots show the cell confluency of the new doses of olaparib given with 0.1 μM ceralasertib (left) and 0.3 μM ceralasertib (right). The dotted curves show the combination treatments that we have experimental data for.

to investigate other combinations of ceralasertib and olaparib which were not investigated in the in vitro experiments. Although results obtained from the modelling studies can often guide further experimental studies, any conclusions should be substantiated with experiments.

The experimental data shows that using both drugs in combination allowed for lower doses of the drugs to be used for shorter treatment periods to induce growth inhibition and cytotoxicity of cancer cells [113]. We investigate the effects on the cell confluency when we add increasing doses of olaparib (0.5 μM, 0.8 μM, 1μM, 1.5 μM, 2 μM, and 5 μM) to the two studied doses of ceralasertib (0.1 μM and 0.3 μM). We fix the doses of ceralasertib and vary the doses of olaparib because the model is able to predict the three unseen time series data including including doses of 0.3 μM olaparib (Section 2.3.3).

Figure 2.9 shows the effect of combining 0.1 μM (left plot) and 0.3 μM (right plot) of ceralasertib with the new doses of olaparib to the cell confluency over 310 hours. As expected, increasing the olaparib dose lowers the cell confluency significantly. This is particularly significant when we add olaparib to 0.3 μM ceralasertib (right plot of Figure 2.9). Here, we see cell confluency values of approximately 10% (the initial confluency), showing the cytotoxic nature of the drugs.

In summary, the results show that using higher doses of the drugs induced cell death and growth inhibition in a much shorter time frame. This is more significant when olaparib is combined with higher doses of ceralasertib.

2.4 Conclusion

In this study, we develop a mechanistic model that represents cancer cells progressing through the cell cycle. To account for the effects of DDR pathway inhibitor drugs, cells can be DNA damaged or undamaged. Including every drug mechanism into the model and the in-depth nature of the DNA damage is elusive. Therefore, in this model, we incorporate only the main drug interactions and DNA damage. After careful model selection to decide on which drug effects we should include in the model, we can calibrate and validate our model. We compare the in silico results to experimental in vitro data provided by AstraZeneca [113]. Our in silico model results are consistent with the experimental in vitro data, which shows that the combination of ceralasertib and olaparib induces greater or equal cytotoxicity and growth inhibition of cancer cells at lower doses and for shorter treatment times compared to either monotherapy. Although one could better fit the data by calibrating the model to all treatment data at once, we decided to use only part of the data to compare the results of the parameterised model, which allowed us to study the model's usefulness in simulating new drug dose combinations.

The results from well-calibrated and validated models can often guide further experimental investigations into drug doses, effects, and combinations that can result in a maximum effect while keeping to the tolerated levels. Therefore, we could expand this model to investigate different sequencing and schedules of the drugs to better get the optimal treatment strategy for cytotoxic and growth inhibitory effects of cancer cells. However, the results from the models should be experimentally validated before any further application. Given that Model HC includes a high number of parameters, most of which are sought with wide intervals between their

upper and lower bounds, using a global optimiser to find the optimal parameter values is too time-consuming and computationally heavy. A future direction for this model could involve optimising the parameters directly from the data. For parameters that cannot be directly fitted from the data, we could seek narrower bounds to reduce the computational costs and therefore make a global optimiser possible. Furthermore, the parameter values are currently significantly different across the five model variations (see Table 2.4 in Section 2.3.1). In the future, we could consider globally optimising a subset of the parameters instead. This means that certain parameters, such as the drug-specific parameters, would be consistent throughout the five model variations.

To conclude, this deterministic model, which incorporates appropriate biological details, is able to satisfactorily capture the quantitative nature of the cell confluency data and the qualitative trends of the cell death data found in vitro. By doing so, we explore a range of new combinations of ceralasertib and olaparib which increase the growth inhibition and cytotoxicity of cancer cells.

Chapter 3

Sensitivity Analysis

3.1 Introduction

Model HC includes a high number of parameters, which can lead to parameter uncertainty. A higher number of parameters means that minor changes in multiple parameter values can significantly affect the model output. This is because a change in one parameter value can influence how other parameters affect the model output, accentuated when more parameters are incorporated into the model. Also, increasing the number of parameters leads to a higher risk of overfitting to the in vitro data (see Appendix A.3.1 for an example of this). We therefore perform sensitivity analysis (SA) to study how sensitive our model output is to changes in the parameter values (i.e., the model inputs) [71, 159]. In other words, SA allows us to see how parameter uncertainty can cause model output uncertainty. We can investigate which parameters influence the uncertainty in the model output, and which do not [74, 170]. If a parameter has no significant effect on the model output, then the modeller can choose to fix the value of the parameter instead or even sometimes omit the parameter all together [74, 170]. This will reduce the number of parameters to be optimised. In Chapter 2, we studied the output of the compartment model with and without relevant drug effects. Once the SA is performed, if some of the incorporated drug effects show no significant impact on the model output, there is the potential to simplify the compartment model.

One of the simplest approaches to SA is to perform local SA [170]. This entails assessing the model output(s) when perturbing one parameter value at a time, whilst all other parameters remain constant [112, 170]. A more complex form of SA is global SA, which involves assessing the model output(s) when perturbing all parameter values simultaneously [112, 170]. In general, global SA is a lot more computationally heavy compared to local SA. However, it enables us to see relationships between the model parameters, which cannot be studied using local SA [112].

For the compartment model (Model HC) described in Chapter 2, we perform two uncertainty and sensitivity analyses to investigate the uncertainty in the parameters listed in Tables 2.2 and 2.3. We perform robustness analysis (Section 3.2) and Latin hypercube analysis (Section 3.3), which check how sensitive the model is to local and global parameter perturbations respectively.

3.2 Robustness Analysis

3.2.1 Method

Robustness analysis is a method of local SA that involves perturbing one parameter value at a time, whilst keeping all other values fixed at their optimised value, and assessing how it affects the model output [74]. Here, we take the input as each of the 24 model parameters listed in Tables 2.2 and 2.3 and the output as the cell confluency over 310 hours for all nine treatments (no drug, monotherapies, and combination therapies).

For each of the input parameters, p_i, $i = 1, 2, \ldots, 24$, we investigate 10 equally spaced values in the range of $\pm 20\%$ the optimised value, i.e., within the range $[p_i \cdot 0.8, p_i \cdot 1.2]$ [74]. We ensure that all parameter values investigated make biological sense so that the model does not output a negative number of cells. For this reason, the parameter values must never go below zero and parameters $I_{\max,C}$, $I_{\max,O}$, p, and q must not exceed one.

3.2.2 Results

For each parameter p_i, we investigate 10 different values, p_i^l, $l = 1, \ldots, 10$ and assess the model output, $f_j(t_k, p_i^l)$, for each treatment j and each time point $t_k = 0, \ldots, \eta$. Here, the model output is the cell confluency. The results of the robustness analysis are summarised in Figure 3.1 where, for each parameter p_i, we plot the maximum and minimum values of the model output out of the 10 investigated values of p_i at each time point. In other words, for each parameter p_i, treatment j, and time point t_k, we plot the maximum model output $\max_{l=1,\ldots,10}(f_j(t_k, p_i^l))$ and the minimum model output $\min_{l=1,\ldots,10}(f_j(t_k, p_i^l))$.

For ease of comparison, for each treatment j and parameter p_i, we calculate the total difference between the maximum and minimum model output over the time course of the simulation. This is calculated by:

$$\text{Total Difference}(j, p_i) = \sum_{k=1}^{\eta} \left(\max_{l=1,\ldots,10} (f_j(t_k, p_i^l)) - \min_{l=1,\ldots,10} (f_j(t_k, p_i^l)) \right). \tag{3.1}$$

Figure 3.2 displays the total difference for each parameter and each drug treatment.

By observing Figure 3.2, we can see that perturbing the drug parameters which relate to ceralasertib inhibiting repair from state SD to S ($I_{\max,C}$, $IC_{50,C}$, $h_{C,1}$) has little effect on the model output for any of the nine treatments. This is because the maximum dose of ceralasertib in the in silico experiments is 0.3 μM, which results in $\text{Effect}_{\text{Cera},1} = 3.119260196 \cdot 10^{-7}$ with the optimised parameter values. This implies that there is little difference in the number of cells that repair from state SD to S when given ceralasertib treatment compared to giving no drug treatment. Hence, this drug effect is not significantly impacted by perturbing these parameter values by $\pm 20\%$. This coincides with Section 2.3.1, where there is only a little difference between the RMSE of Model HC and model version 3 where we omit this drug effect. Also, perturbing k_8 has little effect on the model, which is unsurprising since the optimised value of $k_8 = 0.0010523$ is very small because most cell death from

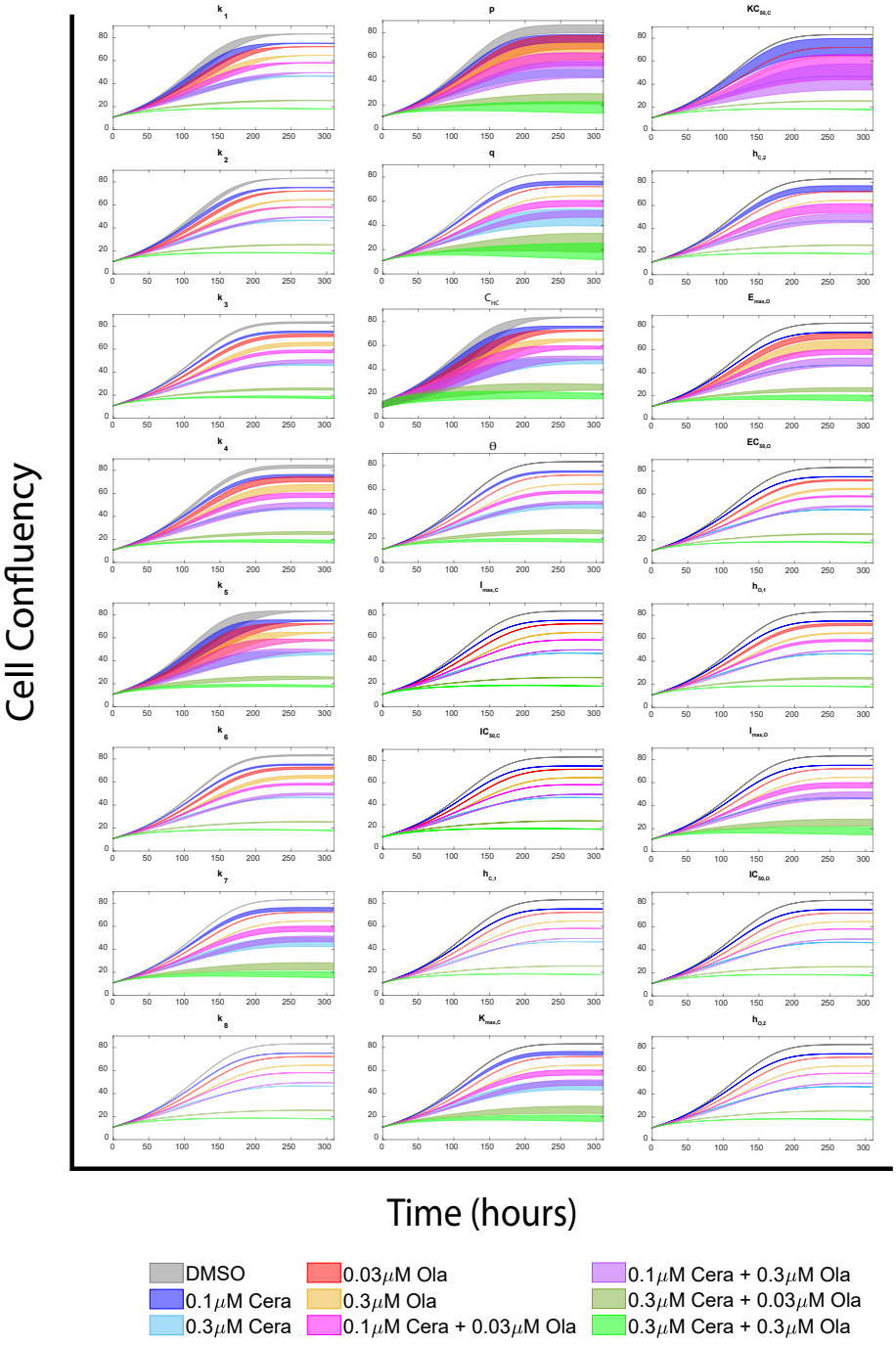

FIGURE 3.1: **Robustness analysis is a method to see how sensitive the model output is to local changes in parameter values.** Each figure represents one parameter, p_i, $i = 1, \ldots, 24$. We investigate 10 equally spaced values of p_i within $\pm 20\%$ of its optimised value. The maximum and minimum values of the cell confluency from the 10 investigated parameter values are displayed for the time course of 310 hours. Each colour represents a different drug treatment.

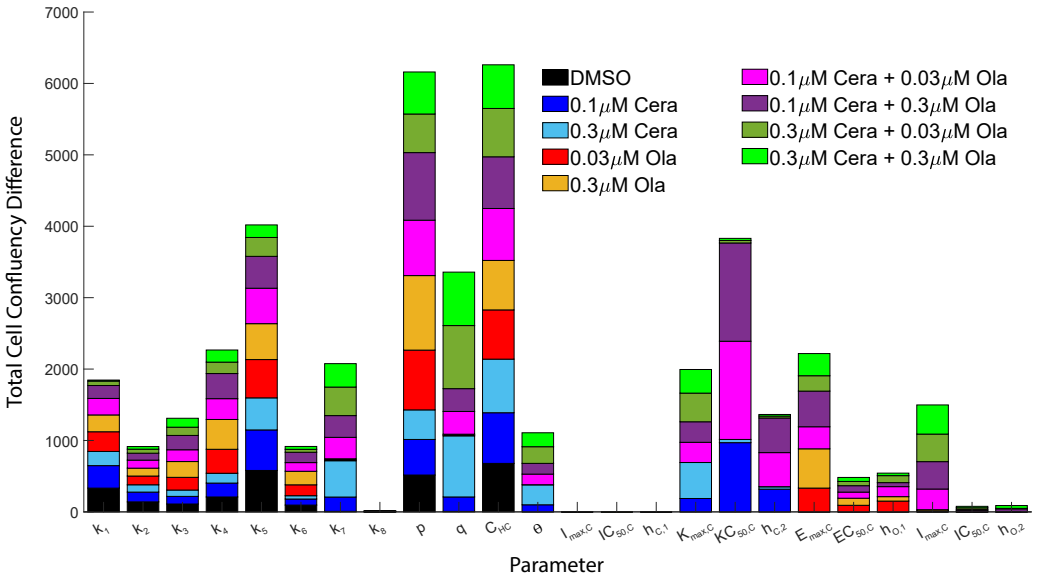

FIGURE 3.2: **Robustness analysis is a method to see how sensitive the model output is to local changes in parameter values.** We investigate 10 equally spaced values of p_i within $\pm 20\%$ of its optimised value. For each treatment (represented by different colours) and each of the 24 parameters (horizontal axis), we plot the total difference between the maximum and minimum cell confluency over the duration of the simulation calculated by equation 3.1 (vertical axis).

state G2D is ceralasertib-related. Thus, perturbing this value by $\pm 20\%$ does not significantly increase the amount of cell death from state G2D.

The parameters that are the most sensitive and have the biggest effect on the model output are k_5, p, q, C_{HC}, and $KC_{50,C}$. k_5 is the rate of cells dividing and re-entering the cell cycle, hence, varying this value means more or fewer cells are progressing through the cell cycle for every treatment. The probabilities p and q represent the probability of cells entering the damaged cell cycle states SD and G2D respectively. Thus, varying these values will cause fewer or more cells to go to states SD and G2D respectively, which affects the amount of cell death. Varying p affects all drug treatments, whereas varying q only affects those treatments including ceralasertib. This is most likely because increasing q causes more cells to enter G2D where they can die from ceralasertib-related cell death. C_{HC} represents the carrying capacity, i.e., the total number of cells allowed in the system. Since this value is also used in the logistic growth term, perturbing this value affects how many cells re-enter the

cell cycle for all drug treatments. Lastly, the value of $KC_{50,C}$ has a significant effect on the model, mainly for those treatments including 0.1 μM of ceralasertib. This is likely because this parameter affects the amount of ceralasertib-related cell death from state G2D. Treatment with 0.1 μM of ceralasertib has no significant effect on the model output compared to no drug treatment. Hence, perturbing values of $KC_{50,C}$ can significantly change the amount of ceralasertib-related cell death from state G2D. All other parameters have an effect on the model output but not as significant as the ones explained.

3.3 Latin Hypercube Analysis

3.3.1 Method

Latin hypercube analysis is a type of global SA that tests how the model output is affected by global parameter perturbations, i.e., after simultaneously varying all 24 model parameters at the same time [74]. We take the input as each of the 24 model parameters listed in Tables 2.2 and 2.3 and the output as the RMSE (equation 2.10) of the cell confluency for each treatment separately. We vary each parameter, p_i, $i = 1,\ldots, 24$ between $\pm 20\%$ of its optimal value, i.e., within the range $[p_i^L, p_i^U] = [p_i \cdot 0.8, p_i \cdot 1.2]$ [74]. Here, L and U denote the lower and upper bounds respectively. For this study, we investigate $w = 100$ different values of each parameter.

First, we use the "lhsdesign" function in MATLAB to generate a Latin hypercube sample (LHS) of w randomly distributed and permuted values between zero and one for each parameter [74]. These w values are randomly sampled from w intervals given by

$$\left(0, \frac{1}{w}\right), \left(\frac{1}{w}, \frac{2}{w}\right), \ldots, \left(1 - \frac{1}{w}, 1\right),$$

where each interval is only sampled from once and chosen from a uniform distribution, in no particular order [111]. For each of the 24 parameters, we repeat this process to obtain w values for parameter 1 $(X_1^1, X_1^2, \ldots, X_1^w)$, w values for parameter 2 $(X_2^1, X_2^2, \ldots, X_2^w)$, and so on until we obtain w values for parameter 24 $(X_{24}^1, X_{24}^2, \ldots, X_{24}^w)$. Hence, we get $24 \cdot w$ values, $X_i^j \in (0,1)$, where $i = 1, 2, \ldots, 24$ and $j = 1, 2, \ldots, w$. To obtain appropriate parameter values p_i^j to investigate, within the upper and lower bounds $[p_i^L, p_i^U]$, we do the following:

$$p_i^j = p_i^L + X_i^j \cdot (p_i^U - p_i^L). \tag{3.2}$$

This process gives us w parameter combinations to perform the Latin hypercube analysis: $(p_1^1, p_2^1, \ldots, p_{24}^1)$, $(p_1^2, p_2^2, \ldots, p_{24}^2)$, $\ldots$, $(p_1^w, p_2^w, \ldots, p_{24}^w)$. In other words, we run the model once where $p_1 = p_1^1$, $p_2 = p_2^1, \ldots, p_{24} = p_{24}^1$, then again where $p_1 = p_1^2$, $p_2 = p_2^2, \ldots, p_{24} = p_{24}^2$, and so on up to where we set $p_1 = p_1^w$, $p_2 = p_2^w, \ldots, p_{24} = p_{24}^w$.

Once we have appropriate parameter values to investigate, we can then assess the correlation between the input and output variables. To determine the strength of the linear correlations, the Pearson Product Moment Correlation Coefficients are calculated for each parameter and drug treatment. Coefficient values in $[0, 0.1)$ are defined as 'negligible', $[0.1, 0.4)$ as 'weak', $[0.4, 0.7)$ as 'moderate', $[0.7, 0.9)$ as 'strong', and $[0.9, 1]$ as 'very strong' [74, 161].

To exemplify the LHS process, let us take a 2-D space, where we are only performing the LHS on 2 parameters $p_1 \in [p_1^L, p_1^U]$ and $p_2 \in [p_2^L, p_2^U]$ and we sample $w = 4$ pairs of parameters (p_1^j, p_2^j), $j = 1, \ldots, w$. To do so, for each parameter, we randomly sample one value from each of the w equally spaced intervals in no particular order:

$$(0, 0.25), (0.25, 0.5), (0.5, 0.75), (0.75, 1).$$

This can be viewed as a $w \times w$ square grid (Figure 3.3 (a)), where there are w^2

potential pairs of intervals we could choose from. In a LHS, we sample w parameter pairs such that each interval is only sampled from exactly once. In other words, we take values once from each row and once from each column [74]. After performing the LHS, we get w sets of coordinates (X_1^j, X_2^j) on the square grid (Figure 3.3 (a)). By using equation 3.2, we obtain w pairs of the two parameters to investigate and perform the Latin hypercube analysis on (Figure 3.3 (b)).

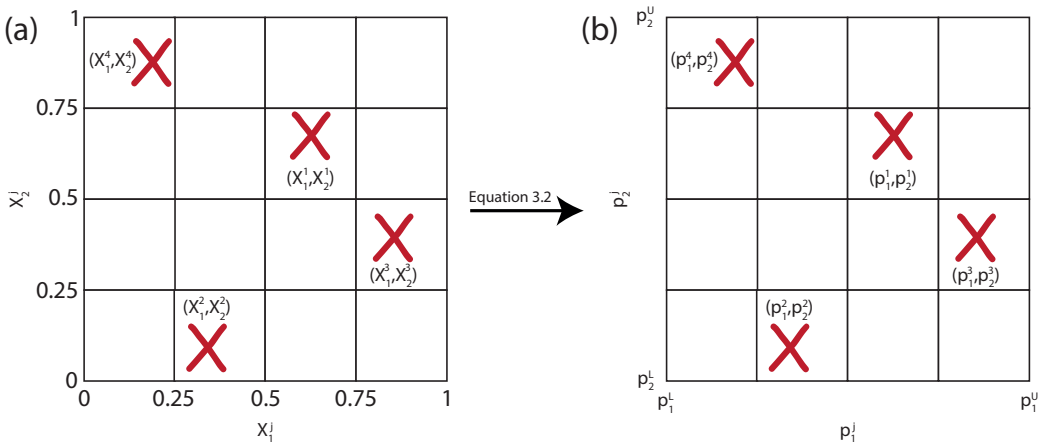

FIGURE 3.3: **A visualisation of LHS performed in a 2-D space.** (a) LHS in a 2-D space can be viewed as a $w \times w$ grid, where each row and each column is uniformly randomly sampled from once to obtain w pairs of values (X_1^j, X_2^j), $j = 1, 2, 3, 4$. (b) By using equation 3.2 to obtain appropriate parameter values p_i^j, this gives us w parameter combinations (p_1^j, p_2^j), $j = 1, 2, 3, 4$ to use for the Latin hypercube analysis. This figure is inspired by the work of Hamis *et al.* [74].

3.3.2 Results

For each parameter and drug treatment, the Pearson Product Moment Correlation Coefficients are displayed in Figure 3.4. We deduce that the majority of parameters have a negligible to weak correlation with the RMSE value for the given parameter range. However, there are a few parameters that do have a strong correlation with the RMSE for certain drug treatments. This means that parameter perturbations could lead to a worse simulation fit to the experimental data. The parameter p has a moderate negative correlation (-0.49466) only for the combination 0.1μM ceralasertib + 0.3μM olaparib. This means that increasing values of p (i.e., more cells enter state

SD) cause decreasing values of the RMSE output. The carrying capacity C_{HC} has a moderate negative correlation (-0.57238) for DMSO. The parameter $KC_{50,C}$ has a moderate positive correlation (0.665229) for the combination 0.1μM ceralasertib + 0.3μM olaparib. However, the parameter $KC_{50,C}$ has a strong negative correlation (-0.71697) for 0.1μM ceralasertib monotherapy. Note that Appendix A.2.1 provides scatter-plots that show the detailed correlations between the model parameters and the model output.

3.4 Conclusion

SA can be a useful tool when developing mathematical models by determining how each parameter contributes to uncertainties in the model output [43]. By performing SA we can see which parameters have the most effect on the model output. These sensitive parameters can then be carefully looked at and parameterised more efficiently [43]. SA also shows us which parameters do not affect the model output. The modeller can choose between fixing these non-sensitive parameters within the parameter range as this will not significantly change the model outputs, or the modeller may omit the parameters from the model all together and create a simplified model [43, 148].

When choosing the parameter values to investigate, we choose to evenly distribute the parameter values in robustness analysis, while in Latin hypercube analysis we use Latin hypercube sampling. We could also choose to randomly sample them. Furthermore, we conduct the SA by investigating parameter values within 20% of their optimised parameters found during the initial model fitting. However, if the parameter values are not identifiable, the sensitivity may be under- or over-estimated if explored only within this region. Therefore, since a parameter identifiability analysis is not conducted in these in silico experiments, in the future, we could conduct the SA by exploring parameter values within the original parameter search space given in Section 2.2.2.2 instead.

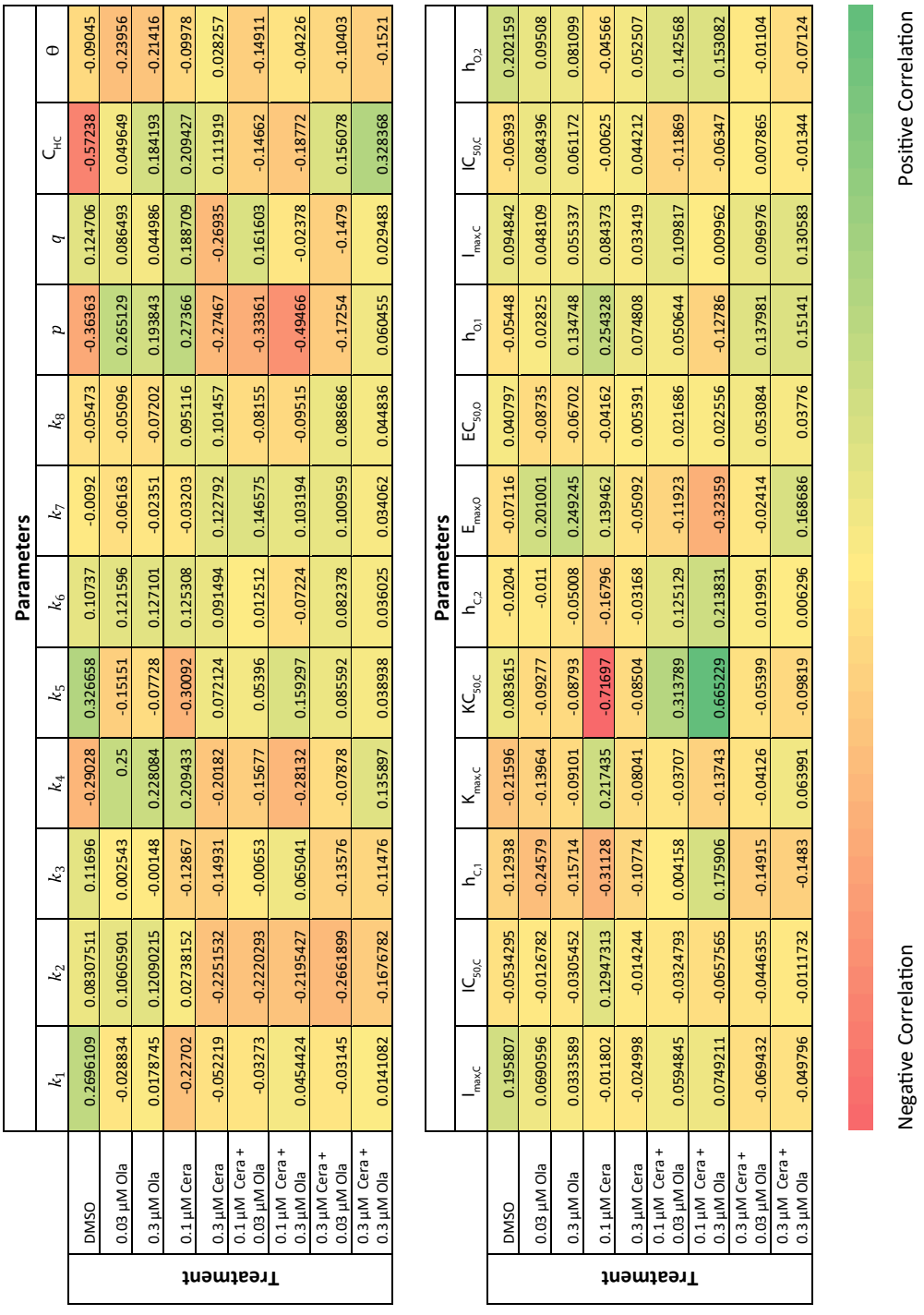

FIGURE 3.4: **Latin hypercube analysis is a method to see how sensitive the model output is to global changes in parameter values.** The figure displays the Pearson Product-Moment Correlation Coefficients relating to the linear correlations between each parameter (columns) and output for each treatment (rows). Here, the model output is the RMSE of the cell confluency throughout the time course of the simulation (equation 2.10) in response to each drug treatment separately.

Also, we chose to perform only two types of SA: robustness analysis and Latin hypercube analysis. There exists a wide range of other SA techniques that can be used on ODE systems. One example is derivative-based local SA which involves calculating the partial derivative with respect to each parameter [45]. Another example is the Morris method which involves calculating the partial derivative using a finite difference scheme [148]. This technique extends the derivative-based local SA into a global SA. A review of other techniques can be found by Qian *et al.* [148].

In our case both the local and global SA agree that the parameters p, C_{HC}, and $KC_{50,C}$ cause the most output sensitivity when perturbed. Hence we may want to look further at the value of these parameters and ensure their values are biologically relevant. Since a lot of the parameters in the model are non-sensitive and do not affect the model output, we could also think about reducing the model described in Chapter 2 and omitting some of the parameters.

Chapter 4

Model Simplification: Minimalistic Approach

4.1 Introduction

Sensitivity analysis explored the sensitivity of some of the parameters used in Model HC (Chapter 3) and indicated that one could reduce the complexity of the model even further. Moreover, we would also like to study the competition for space between drug-sensitive and drug-resistant cancer cells that are subjected to DDR inhibitor drugs. Since temporal compartment models do not consider space, we aim to map a compartment model onto a 2-D agent-based model (ABM), where the growth of the cell population is affected by spatial structure. This does not require a complex model because we are focusing only on the spatial competition between two subpopulations: drug-sensitive cells and drug-resistant cells.

Informed by sensitivity analysis, as a first step toward studying the spatial competition between subpopulations, we simplify the compartment model to reduce the number of parameters (Section 4.2.1). The model is parameterised and evaluated against experimental data 2 (Section 1.3) obtained from our collaborators AstraZeneca (Section 4.2.2). The simplified model is called Model MC because it will have medium complexity (MC). A data-driven model selection that motivates

the choice of the model is included in Appendix A.3.1. Since the model will still include the effects of ceralasertib and olaparib, it may also be used to study the optimal combination doses of the drugs.

4.2 Model and Method

4.2.1 Temporal Cell Population Dynamics: A Simplified Compartment Model

We develop a compartment model that describes how cell populations that are: (a) not spatially structured, and (b) fully drug-sensitive change over time in response to treatments with one or two DDR inhibitor drugs. One of these drugs is an ATRi (ceralasertib), and the other drug is a PARPi (olaparib). For this part of the study, we use experimental data 2 (Section 1.3) to parameterise and evaluate our mathematical model. We choose to use experimental data 2 to see if we can develop a mathematical model to capture the trends in this data set as both experimental data 1 and 2 show significant variability. The simulations of the model are implemented in MATLAB and the parameters are estimated by using a global optimiser on MATLAB, minimising the sum of square residuals between the model output and the in vitro data. In the compartment model, cell division and drug effects are respectively modelled by a cell cycle model (Section 4.2.1.1) and a drug response model (Section 4.2.1.2).

To simplify Model HC (Chapter 2), we keep only the necessary drug effects and compartments to minimise the number of parameters. We first omit the G2D compartment because we do not have data for the number of damaged cells in the G2/M phase. Also, since we cannot quantitatively use the cell death in vitro data because the experiments use fluorescence intensities to measure cell death (Section 1.3) which are not included in our model, we do not include a dead state in the model. Instead, we include a non-cycling (NC) state which represents cells with irreparable DNA damage. Note that cells in the NC state contribute to both the total

number of cells and the cell confluency. Lastly, we minimise the number of drug effects in the model and include only one set of drug-specific parameters for each drug. To obtain synergy from the simplified model, we include a combined Emax equation (equation 4.8).

4.2.1.1 Modelling the Cell Cycle

The compartment model used in this study (Figure 4.1 (a)) is based on previous modelling work by Hamis *et al.* [76], Checkley *et al.* [34], and work completed in Chapter 2 [147]. The model is described by a system of ODEs, in which each dependent variable $[y]$ describes the concentration of cells in compartment y. The drugs that we consider in this study target cells that are in specific phases of the cell cycle and, accordingly, each compartment represents a cell cycle phase state. We include three undamaged and proliferative cell cycle states in the model, specifically the gap 1 (G1) state, the synthesis (S) state, and the combined gap 2/mitosis (G2/M) state (Figure 4.1 (a)). This model is an abstraction of the biological cell cycle, where cells in the gap 1 phase grow and prepare for DNA replication, which occurs in the synthesis phase, and cells in the subsequent gap 2 phase prepare for cell division, which occurs in the mitosis phase [91]. We also include a damaged S state (SD), representing cells that have replication stress-induced DNA damage, a type of DNA damage that results from faulty DNA replication [137, 160]. FaDu ATM-KO cells, which are used to calibrate our model, are prone to such replication stress [113]. A non-cycling (NC) state is also included in the model. Cells in the NC state have irreparable DNA damage and are thus unable to proliferate. Cells that enter the NC state remain there throughout the entire simulation.

In the model, cells progress through the cell cycle states via unidirectional paths that are associated with rates (Figure 4.1 (a)). These rates depend on drug concentrations, as explained in more detail in Section 4.2.1.2, and the total cell concentration $N(t)$. The latter dependency is included in the model to achieve logistic growth rates of the cell populations, as are observed in the in vitro data that we use to parameterise

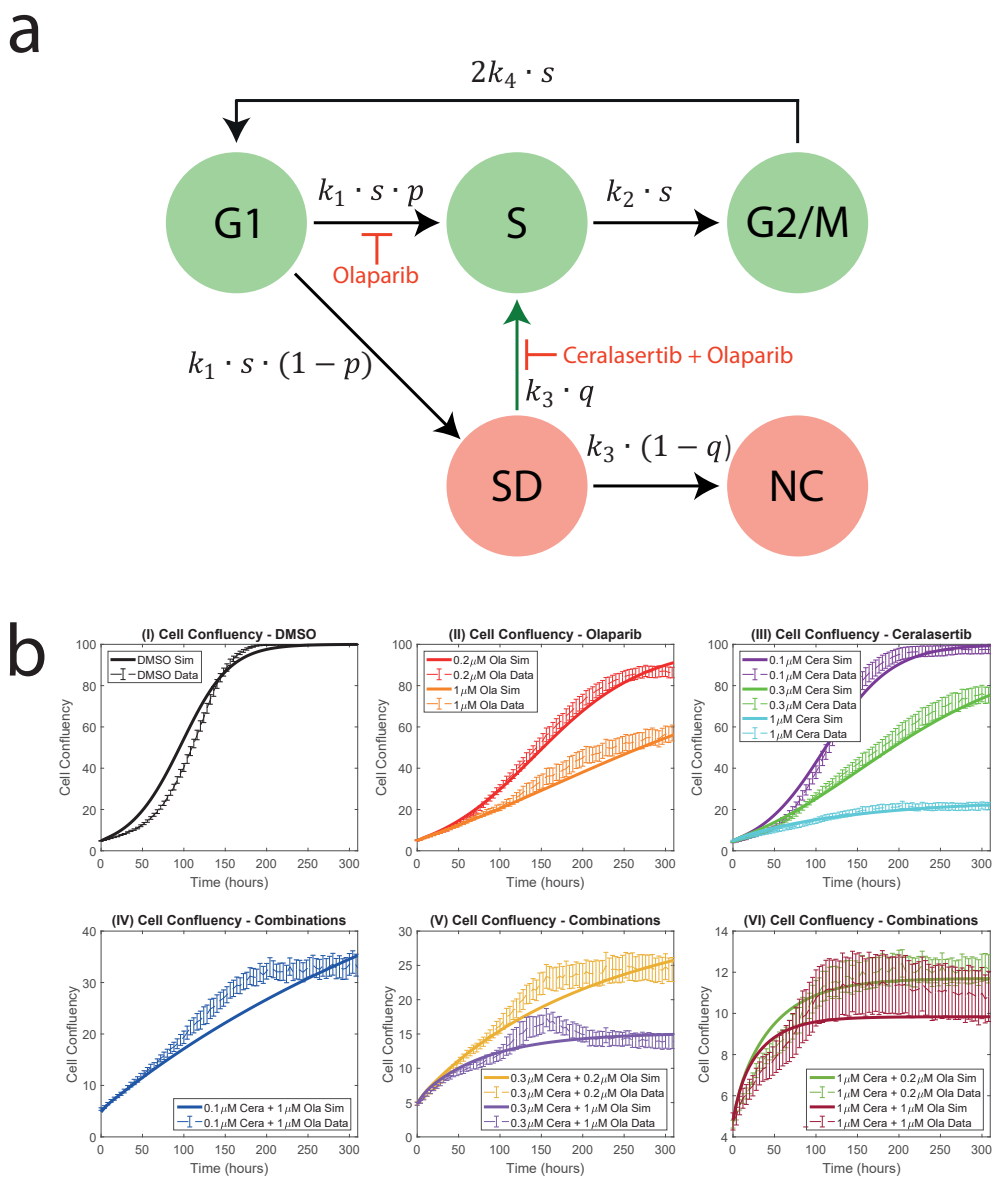

FIGURE 4.1: **The compartment model (Model MC) is parameterised and evaluated against in vitro experimental data 2.** (a) In the compartment model, cells can be in undamaged and cycling (green nodes) or damaged and/or non-cycling (red nodes) cell cycle states. Cells can progress through the undamaged states (G1, S, and G2/M) and damaged states (SD, NC). Cells in SD experience DNA replication stress and cells in NC have irreparable DNA damage. The paths show the transitions between states where $k_i(N(t))$, $i = 1, 2, 3, 4$ are rate constants and s is a scaling parameter. p and q represent drug-dependent probabilities that a particular path will be chosen at a fork. The PARPi inhibits cells from progressing from state G1 to S. The green path represents DNA damage repair, which is inhibited by both the ATRi and the PARPi. The time and drug dependencies of the parameters in (a) have been omitted for ease of presentation. (b) The plots show simulated and experimental cell confluency over 310 hours for various dose combinations of the ATRi and PARPi. Training data is used to estimate model parameters (plots I-V) and test data is used to evaluate the model (plot VI). The solid curves represent the simulation results from the compartment model. The dashed curves represent the mean in vitro data, with the standard error of the mean for 3 experiments indicated with error bars.

and evaluate our model (Section 4.2.2). Note that after the G1 state, cells enter the S state at a rate that is proportional to a weighting factor p, and cells enter the damaged SD state at a rate that is proportional to $1 - p$. The factor p decreases with increasing concentrations of the PARPi (olaparib), which captures the drug's replication stress-inducing drug effect. Note also that cells in the SD state repair their DNA damage at a rate that is proportional to the weighting factor q, which is a function of both the PARPi and the ATRi (ceralasertib). As such, q describes the fraction of cells leaving SD that enter state S. The remaining fraction of cells that leave the SD state enter the NC state. The factor q decreases with increasing drug concentrations, which captures the replication repair-inhibiting drug effects of the ATRi and PARPi. Cells that successfully progress to, and leave, the G2/M state re-renter the G1 state and produce a daughter cell that is initiated in state G1 (Figure 4.1 (a)). The compartment model is described with the following system of ODEs:

$$\frac{d[G1](t)}{dt} = 2k_4\big(N(t)\big)s[G2/M](t) - k_1\big(N(t)\big)s[G1](t), \tag{4.1a}$$

$$\begin{aligned}\frac{d[S](t)}{dt} =& k_1\big(N(t)\big)sp([\text{drug}_{\text{Ola}}])[G1](t) - k_2\big(N(t)\big)s[S](t) \\ &+ k_3\big(N(t)\big)q([\text{drug}_{\text{Cera}}], [\text{drug}_{\text{Ola}}])[SD](t),\end{aligned} \tag{4.1b}$$

$$\frac{d[SD](t)}{dt} = k_1\big(N(t)\big)s(1 - p([\text{drug}_{\text{Ola}}])[G1](t) - k_3\big(N(t)\big)[SD](t), \tag{4.1c}$$

$$\frac{d[G2/M](t)}{dt} = k_2\big(N(t)\big)s[S](t) - k_4\big(N(t)\big)s[G2/M](t), \tag{4.1d}$$

$$\frac{d[NC](t)}{dt} = k_3\big(N(t)\big)(1 - q([\text{drug}_{\text{Cera}}], [\text{drug}_{\text{Ola}}]))[SD](t), \tag{4.1e}$$

with the initial conditions:

$$[G1](0) = G1_0 \cdot N(0), \tag{4.2a}$$

$$[S](0) = S_0 \cdot N(0), \tag{4.2b}$$

$$[SD](0) = SD_0 \cdot N(0), \tag{4.2c}$$

$$[G2/M](0) = G2/M_0 \cdot N(0), \tag{4.2d}$$

$$[NC](0) = NC_0 \cdot N(0). \tag{4.2e}$$

In equations 4.1a-e and 4.2a-e, $N(t)$ is the total concentration of the cell population at time t,

$$N(t) = [G1](t) + [S](t) + [SD](t) + [G2/M](t) + [NC](t). \tag{4.3}$$

The drug effects $p([\text{drug}_{\text{Ola}}])$ and $q([\text{drug}_{\text{Cera}}], [\text{drug}_{\text{Ola}}])$ are described in Section 4.2.1.2. In our model, we assume that cell cycle progression is halted when cells are in the SD state. Therefore, to fit the model to cell doubling time data, we multiply the rate parameters $k_1\big(N(t)\big), k_2\big(N(t)\big)$, and $k_4\big(N(t)\big)$ with a scaling parameter s in equations 4.1a-e. To achieve logistic growth of $N(t)$, all rates $k_1\big(N(t)\big)$ to $k_4\big(N(t)\big)$ depend on $N(t)$ and the carrying capacity C_{MC} such that,

$$k_i\big(N(t)\big) = k_i'\left(1 - \frac{N(t)}{C_{\text{MC}}}\right) \quad \text{for } i = 1, 2, 3, 4, \tag{4.4}$$

where the values of k_i' are estimated from in vitro data and are given in Table 4.2.

4.2.1.2 Modelling DDR Inhibitor Drugs

The effects of the ATRi (ceralasertib) and the PARPi (olaparib) are implicitly modelled by inhibition of the rates at which cells progress in the cell cycle model where

paths are weighted by factors $p([\text{drug}_{\text{Ola}}])$ and $q([\text{drug}_{\text{Cera}}], [\text{drug}_{\text{Ola}}])$ (Figure 4.1 (a)). The drug effects are modelled by:

$$p([\text{drug}_{\text{Ola}}]) = p_0(1 - E_2([\text{drug}_{\text{Ola}}])) \tag{4.5}$$

and

$$q([\text{drug}_{\text{Cera}}], [\text{drug}_{\text{Ola}}]) = q_0(1 - E_{1,2}([\text{drug}_{\text{Cera}}], [\text{drug}_{\text{Ola}}])), \tag{4.6}$$

where p_0 and q_0 are the baseline weighting factors that represent the system in the absence of drugs, and $[\text{drug}_{\text{Cera}}]$ and $[\text{drug}_{\text{Ola}}]$ denote the concentration of ceralasertib and olaparib respectively. The functions E_1 and E_2 are calculated using the sigmoid Emax model [82, 76] and are introduced to achieve drug effects that match in vitro data (Section 4.2.2). We thus set:

$$E_1([\text{drug}_{\text{Cera}}]) = E_{\max,1} \frac{[\text{drug}_{\text{Cera}}]^{h_1}}{[\text{drug}_{\text{Cera}}]^{h_1} + \text{EC}_{50,1}^{h_1}}, \tag{4.7a}$$

$$E_2([\text{drug}_{\text{Ola}}]) = E_{\max,2} \frac{[\text{drug}_{\text{Ola}}]^{h_2}}{[\text{drug}_{\text{Ola}}]^{h_2} + \text{EC}_{50,2}^{h_2}}, \tag{4.7b}$$

where $E_{\max,i}$ is the maximal drug effect, h_i is the Hill coefficient, $\text{EC}_{50,i}$ is the concentration of the drug that results in half the maximal drug effect, and i = 1, 2 to represent ceralasertib and olaparib respectively. To model the combined effect of the two drugs, we use the Bliss independence synergy model [101] so that:

$$\begin{aligned} E_{1,2}([\text{drug}_{\text{Cera}}], [\text{drug}_{\text{Ola}}]) = {} & E_1([\text{drug}_{\text{Cera}}]) + E_2([\text{drug}_{\text{Ola}}]) \\ & - E_1([\text{drug}_{\text{Cera}}]) \cdot E_2([\text{drug}_{\text{Ola}}]). \end{aligned} \tag{4.8}$$

4.2.2 Model Parameterisation

The compartment model parameters are estimated from an in vitro experiment in which FaDu ATM-KO cells were subjected to one or two DDR inhibitor drugs (experimental data 2, Section 1.3) [113]. Cell confluency and cell death data were

reported for 0-310 hours, and pulse-chase data were reported for 0-24 hours. To parameterise the compartment model, we first directly read some model parameters ($N(0), C_{\mathrm{MC}}, G1_0, S_0, SD_0, G2/M_0, k_1', k_2', k_4', q_0$) from the in vitro data. We thereafter estimate the remaining parameters ($p_0, k_3', s, E_{\mathrm{max},1}, E_{50,1}, h_1, E_{\mathrm{max},2}, E_{50,2}, h_2$) with a global optimiser in MATLAB that minimises the sum of squares of the residuals between the model output and the in vitro data [175].

The in vitro cell confluency data gives the percentage of area in the well plates covered by cells. Based on three experimental repeats and in the absence of drugs, the initial mean cell confluency is 4.82%. Hence, in the compartment model, the initial concentration of cells is $N(0) = 4.82$. The carrying capacity is $C_{\mathrm{MC}} = 100$ which represents 100% cell confluency in the in vitro experiments. We calculate the initial concentration of cells in each compartment based on the mean values obtained from pulse-chase experiments recorded two hours after the start of the experiments. These experiments measure the fraction of cells in G1, S, and G2/M. They also measure cells that are γH2AX positive, a marker of DNA damage [163]. We assume that cells in state SD are γH2AX positive as we associate this state with replication stress. The fractions ($G1_0, S_0, SD_0, G2/M_0$) are multiplied by the initial concentration of cells, $N(0)$, to estimate the respective initial concentration of cells in compartments G1, S, SD, and G2/M. We assume that all initial cells in the system

Parameter Name	**Parameter Value**	**Parameter Description**
$G1_0$	0.36	The fraction of cells in state G1 at the start of the simulation.
S_0	0.14	The fraction of cells in state S at the start of the simulation.
SD_0	0.04	The fraction of cells in state SD at the start of the simulation.
$G2/M_0$	0.46	The fraction of cells in state G2/M at the start of the simulation.
NC_0	0	The fraction of cells in state NC at the start of the simulation.

TABLE 4.1: **Initial conditions are estimated from in vitro experimental data 2.** The initial fraction of cells in states G1, S, SD, and G2/M are estimated from pulse-chase data. At the start of the simulations, no cells are in the non-cycling state NC.

are cycling (G1, S, or G2/M), or have the potential to become cycling (SD). Thus, no cells are in the NC state at the beginning of the simulation.

The baseline probability q_0 is set to one based on observations from in vitro experiments which monitor cells with loss of membrane integrity by using a cell death marker, cytotox, in the absence of drug treatment. The cytotox intensity decreased over time in these experiments in experimental data 2 (Section 1.3; Figure 1.5), thus, in the mathematical model, we assume all cells will repair in the absence of the drugs.

Parameter Name	**Parameter Value**	**Parameter Description**
Parameter values that are estimated by fitting the compartment model to in vitro data.		
C_{MC}	100 (cells/A)	The carrying capacity in the compartment model (Model MC).
$N(0)$	4.82 (cells/A)	The total number of initial cells.
p_0	0.3558	The probability that cells transition from state G1 to S in the absence of drugs.
q_0	1	The probability that cells transition from state SD to S in the absence of drugs.
s	1.824	The scaling parameter that adjusts for cell cycle arrest.
k_1'	0.0678 (1/hour)	The rate at which cells leave state G1 in the absence of cell crowding.
k_2'	0.1742 (1/hour)	The rate at which cells leave state S in the absence of cell crowding.
k_3'	0.1420 (1/hour)	The rate at which cells leave state SD in the absence of cell crowding.
k_4'	0.0530 (1/hour)	The rate at which cells leave state G2/M in the absence of cell crowding.
$E_{\max,1}$	1	The maximal drug effect of ceralasertib.
$E_{50,1}$	0.2579 μM	The concentration of ceralasertib that results in half the maximal effect.
h_1	1.5187	The Hill coefficient of ceralasertib.
$E_{\max,2}$	0.5609	The maximal drug effect of olaparib.
$E_{50,2}$	0.1275 μM	The concentration of olaparib that results in half the maximal effect.
h_2	1.0962	The Hill coefficient of olaparib.

TABLE 4.2: **Parameter values are estimated from in vitro experimental data 2.** The table displays the parameter values that are used in the compartment model (Model MC). A denotes the area of the spatial domain in the in vitro experiment.

The parameters $k_i(N(t))$, $i = 1, 2, 3,$ and 4 represent the rate at which cells leave G1, S, SD, and G2/M respectively. The doubling time of FaDu ATM-KO cells is 41 hours and we assume that the initial fraction of cells in state y is also the fraction of the cells doubling time that the cell spends in state y. Since the rates are measured in units of 1/hour, we estimate the following:

$$k_1' = \frac{1}{41 \cdot G1_0}, \tag{4.9a}$$

$$k_2' = \frac{1}{41 \cdot S_0}, \tag{4.9b}$$

$$k_4' = \frac{1}{41 \cdot G2/M_0}. \tag{4.9c}$$

The parameters $(p_0, k_3', s, E_{\max,1}, E_{50,1}, h_1, E_{\max,2}, E_{50,2}, h_2)$ are estimated by using a global optimiser on MATLAB, minimising the sum of square residuals between the model output and the in vitro data.

Following the 80-20 rule of thumb, which recommends using 80% of available data to train a model, and 20% of available data to test a model [96], we use data from nine time series experiments to parameterise (or train) the model (Fig 4.1b I-V) and two time series experiments to evaluate (or test) the model (Fig 4.1b VI).

Parameter values related to the initial conditions are listed in Table 4.1 and all other parameters are listed in Table 4.2. Since the compartment model (Figure 4.1 (a)) is able to satisfactorily predict unseen time series data, we argue that the model is appropriate for our current study which aims at modelling cell population dynamics in response to 0.1-1 μM ceralasertib doses and 0.2-1 μM olaparib doses.

4.3 Conclusion

In this Chapter, we have simplified the compartment model described in Chapter 2 by reducing the number of compartments and parameters. Here, we have adapted

some of the modelling assumptions to simplify the model and calibrated the model with experimental data 2 (Section 1.3). A single model may not always adequately fit all data as these drugs given in various doses may have varying effects on the cell populations. The selection of a particular model depends on the questions that we are trying to answer and the mechanisms that we intend to study. One may need to consider complex models depending on the study, while in other cases, simplified models are sufficient. For example, the simplified model that incorporates a combined Emax model (Model MC) will suffice to predict new drug combinations and parameterise the ABM. However, when studying the individual modes of drug actions of ceralasertib and olaparib as we did in Chapter 2, a more complex model seemed more appropriate.

In Appendix A.3.1, we compare both Model MC and Model HC to experimental data 2. In the future, we could also compare both Model MC and Model HC to experimental data 1. By doing so, we can compare the model goodness of fits visually or by computing the RMSEs. In addition to this, we could perform information criteria analyses such as Akaike information criteria [144] or Bayesian information criteria [132] to balance model goodness of fit to the experimental data with model complexity. We may then select the most applicable model for further investigations on new drug dose combinations.

Chapter 5

Drug Synergy: Investigating Drug Combinations

5.1 Introduction

Anti-cancer drug treatments are commonly administered as monotherapies [16] at their maximum tolerated doses (MTDs) [122, 97]. However, giving drugs at their MTDs has been associated with drug resistance [122, 97, 102]. For instance, drugs administered at their MTDs are only cytotoxic to drug-sensitive cells. Consequently, the elimination of drug-sensitive populations causes the rapid proliferation of drug-resistant populations often due to the lack of competition between the drug-sensitive cells that have been eliminated [97, 122]. Cancer therapies can utilise the combination of multiple different anti-cancer treatments at lower doses (compared to their MTDs) to optimise cancer growth inhibition, increase cytotoxicity, and avoid drug resistance [113, 16]. Many experimental studies have found that drugs administered at doses lower than their MTDs are more effective at controlling the size of tumours compared to giving drugs at their MTDs [156, 113, 11, 176]. These combined treatments include combinations of surgery, DDR inhibitors, ionising radiation, and chemotherapy [105, 65]. Many anti-cancer drugs exist these days and have the potential to be combined to enforce such effects. However, it is difficult to

understand which drug combinations work well and which do not.

To improve the efficacy of cancer treatments, we aim to find combination doses that act synergistically to achieve a desired effect [62]. To do so, there exist reference models to determine the interaction between drug combinations [185]. The observed drug combination effect is compared to the additive effect predicted by the reference model and the combination is labelled as synergistic, additive, or antagonistic. A combination is said to be ***synergistic*** when the combination effect is greater than the expected ***additive*** effect [62, 185], i.e., if the combination achieves the effect E with lower drug doses then it is synergistic [116]. Conversely, a combination is said to be ***antagonistic*** when the combination effect is less than the expected additive effect. However, the exact definition of additive is somewhat subjective and differs for each reference model. A common misunderstanding of additivity is that you add the independent effects of the drugs to obtain the expected additivity. However, this is untrue because, for example, if drug A kills 60% of cells and drug B kills 70% of cells, it is impossible to kill 130% of cells [62]. This has made it difficult for researchers to agree on what defines a drug combination as synergistic. Instead, we observe that there is no "correct" reference model for synergism that should always be used. Many people have debated which method is the best and why different methods fit different scenarios better. For example, Greco *et al.* [67] debates between using either the Loewe additivity model or the Bliss independence model - two of the most commonly used reference models. Others have addressed the limitations of already developed reference models and have proposed their own reference models, for example, Yadav *et al.* [185] proposed the zero interaction potency model and Gevertz *et al.* [62] proposed the lowest single dose (LSD) model.

Based on the experimental evidence, Lloyd *et al.* [113] proposed that there is synergy between ATR and PARP inhibitors in ATM-deficient cancers. Gevertz *et al.* [62] developed the Multi-Objective Optimization of Combination Synergy - Dose Selection (MOOCS-DS) which can be used to find synergistic drug doses that

can be used as a guide for combination drug dose selection in experimental studies. In this Chapter, we explore the combination doses of ceralasertib and olaparib for which the compartment model described in Chapter 4, Model MC, shows synergistic effects. To do so, we use four different reference models: Bliss, highest single agent, Loewe, and LSD (Section 5.2). Also, we use the MOOCD-DS model to investigate optimal combination doses of ceralasertib and olaparib.

5.2 Method

The methods used in this Section are based on previous work by Gevertz *et al.* [62], Yadav *et al.* [185], and Greco *et al.* [67].

We compare the interactions of the drugs by comparing the drug effects to an effect, E, where $E(d_1, d_2)$ represents the effect after giving dose d_1 of drug 1 and dose d_2 of drug 2. The measure of the effect, E, is decided by the modeller and could measure the total tumour growth inhibition or the total number of dead cells, for example. Here, we define the effect E as the normalised total number of cells at the end of the simulation compared to the effect in the absence of drugs, such that:

$$E = \frac{N_0(t_{\text{end}}) - N_{\text{j}}(t_{\text{end}})}{N_0(t_{\text{end}})}, \tag{5.1}$$

where $N_j(t_{\text{end}}) = [G1]_j(t_{\text{end}}) + [S]_j(t_{\text{end}}) + [SD]_j(t_{\text{end}}) + [G2/M]_j(t_{\text{end}}) + [NC]_j(t_{\text{end}})$ is the total number of cells in the system at the end of the simulation for each drug treatment j and $j = 0$ represents the no drug treatment case.

Following Gevertz *et al.* [62], the definitions of synergy can be split into two categories: (1) the synergy of efficacy (SoE) which describes drugs as synergistic if the combination dose has a better effect compared to giving the drugs as monotherapies, or (2) the synergy of potency (SoP) which maximises combination synergy by identifying the smallest possible drug doses to reach an effect E. SoE is an effect-based approach, where the decision of whether drugs are synergistic depends on

the output of the model, i.e., the efficacy. SoP is a dose-effect approach, where the decision of whether drugs are synergistic depends on the input of the model, i.e., the drug doses.

We use four reference models to investigate synergy between ceralasertib and olaparib, namely, the Bliss independence model [19], the highest single agent (HSA) [179], the Loewe additivity model [115], and the lowest single dose (LSD) [62]. The former three are well-known reference models, and the latter was introduced by Gevertz *et al.* [62] as a similar method to HSA but potency-based rather than efficacy-based. Both Bliss and HSA are considered as SoE and both Loewe and LSD are considered as SoP.

A combination index (CI) is a number that allows the clarification of drug synergism, additivity, or antagonism [62, 56]. The calculation of the CI varies for each reference model, but the method of clarification remains consistent and is determined by:

$$\text{CI} = \begin{cases} > 1, & \text{Antagonism,} \\ = 1, & \text{Additive,} \\ < 1, & \text{Synergy.} \end{cases} \tag{5.2}$$

5.2.1 Synergy of Efficacy

For a reference model, x, the expected effect of the drug combination is $E_x(d_1, d_2)$ and the actual effect of the drug combination is $E(d_1, d_2)$. If the actual effect is the same as the expected effect (i.e., $E(d_1, d_2) = E_x(d_1, d_2)$), then we define the drug combination as additive. If the actual effect is greater than what was expected (i.e., $E(d_1, d_2) > E_x(d_1, d_2)$), then we say the drugs work better together in combination and hence, the combination is said to be synergistic. If the actual effect is less than what was expected (i.e., $E(d_1, d_2) < E_x(d_1, d_2)$), then we say the combination is antagonistic.

Therefore, for SoE reference models such as Bliss and HSA, to define a combination of drugs as synergistic, additive, or antagonistic, the CI is defined as the ratio between the expected additive effect and the actual effect [62], such that

$$\mathrm{CI} = \frac{E_x(d_1, d_2)}{E(d_1, d_2)}. \tag{5.3}$$

5.2.1.1 Bliss Independence Model

The Bliss independence model uses probabilistic theory and assumes that the two drugs in combination work independently and do not interact with one another [116]. However, the model assumes that the two drugs do contribute to a common effect. Thus, for the Bliss independence model, the expected effect of the drugs (equation 5.4) and the CI (equation 5.5) can be calculated by:

$$E_{\mathrm{Bliss}}(d_1, d_2) = E(d_1, 0) + E(0, d_2) - E(d_1, 0)E(0, d_2), \tag{5.4}$$

$$\mathrm{CI}_{\mathrm{Bliss}}(d_1, d_2) = \frac{E_{\mathrm{Bliss}}(d_1, d_2)}{E(d_1, d_2)}. \tag{5.5}$$

5.2.1.2 Highest Single Agent (HSA)

The highest single agent (HSA) method states that a combination dose (d_1, d_2) is additive if its efficacy is equal to that of the efficacy achieved from the more efficacious monotherapy, $(d_1, 0)$ or $(0, d_2)$ [62]. In other words, any additional effect over the highest monotherapy is considered synergistic. Thus, for the HSA model, the expected effect of the drugs (equation 5.6) and the CI (equation 5.7) can be calculated by:

$$E_{\mathrm{HSA}}(d_1, d_2) = \max\{E(d_1, 0), E(0, d_2)\}, \tag{5.6}$$

$$\mathrm{CI}_{\mathrm{HSA}}(d_1, d_2) = \frac{E_{\mathrm{HSA}}(d_1, d_2)}{E(d_1, d_2)}. \tag{5.7}$$

5.2.2 Synergy of Potency

The methods to calculate the CI values for the SoP models are more complicated compared to those for the SoE models.

5.2.2.1 Loewe Additivity Model

The following is based on previous work by Gevertz *et al.* [62], Yadav *et al.* [185], Lederer *et al.* [106], and Geary *et al.* [61].

The Loewe additivity model assumes that the two drugs in combination act on the same pathway with similar modes of action [62]. Following the Dose Equivalence Principle, there exist monotherapy drug doses D_1 and D_2 of drug 1 and drug 2 respectively, that produce the same effect, i.e., $(E(D_1, 0) = E(0, D_2))$ [62]. Drug A is defined to be more potent than drug B if a lower dose of drug A elicits the same effect as a higher dose of drug B.

Without loss of generality, we assume that drug 2 is just as or more potent than drug 1, i.e., a lower dose of drug 2 elicits the same effect as a higher dose of drug 1 ($E(D_1, 0) = E(0, D_2)$, where $D_2 < D_1$). Therefore, we can express the dose D_2 of drug 2 through scaling the dose D_1 of drug 1 by the fixed potency ratio $k \in (0, 1]$ such that:

$$D_2 = kD_1 \implies k = D_2/D_1. \tag{5.8}$$

Let (d_1, d_2) be a combination of drugs 1 and 2, where d_1 and d_2 represent the doses of drugs 1 and 2 respectively that are used in the combination. We consider a combination (d_1, d_2) that achieves the same effect, E, as the monotherapy doses D_1

and D_2, i.e., $E(d_1, d_2) = E(D_1, 0) = E(0, D_2)$. Loewe defines additivity when:

$$D_2 = d_2 + kd_1. \tag{5.9}$$

After division by D_2, Loewe additivity can be defined when:

$$\frac{d_1}{D_1} + \frac{d_2}{D_2} = 1. \tag{5.10}$$

If the actual dose of the combination (d_1, d_2) that achieves the same effect as the monotherapies is smaller than what is expected by Loewe, we classify the combination as synergistic [62]. If the actual effect of the combination (d_1, d_2) is bigger than what is expected by Loewe, we classify the combination as antagonistic [62]. Thus, we can express the Loewe CI as follows

$$\mathrm{CI}_{\mathrm{Loewe}}(d_1, d_2) = \frac{d_1}{D_1} + \frac{d_2}{D_2}. \tag{5.11}$$

5.2.2.2 Lowest Single Dose (LSD)

The potency-based equivalent of the efficacy-based HSA method is the lowest single dose (LSD), which was developed by Gevertz *et al.* [62]. This approach firstly defines a percent inhibition (PI), PI^i_{50}, which is the dose of drug i that achieves 50% of the desired effect compared to the control case. In our case, this is 50% of the normalised total number of cells compared to that from the no drug case (equation 5.1), i.e., $E(PI^1_{50}, 0) = E(0, PI^2_{50}) = 0.5$. Secondly, to compare the potency of multiple drugs, the relative potency is defined to be the ratio of the monotherapy dose, D_i, of a drug i to its PI, PI^i_{50}, i.e., $\frac{D_i}{PI^i_{50}}$. For example, let us assume that drug 1 and drug 2 can both reach a target effect, E, at monotherapy doses D_1 and D_2 respectively, i.e., $E(D_1, 0) = E(0, D_2)$. We can compare the potency of drug 1 and drug 2 using the relative potency ratios $\frac{D_1}{PI^1_{50}}$ and $\frac{D_2}{PI^2_{50}}$. If a combination (d_1, d_2) achieves the same

effect as both monotherapies, i.e., $E(D_1, 0) = E(0, D_2) = E(d_1, d_2)$, then the drugs are deemed additive if the relative combination dose

$$d_{\text{comb}}(d_1, d_2) = \frac{d_1}{PI_{50}^1} + \frac{d_2}{PI_{50}^2} \tag{5.12}$$

is equal to the more potent monotherapy (i.e., the relative potency of the drug that needs a lower dose to achieve the same efficacy) defined by:

$$D_{\text{pot}}(D_1, D_2) = \min\{\frac{D_1}{PI_{50}^1}, \frac{D_2}{PI_{50}^2}\}. \tag{5.13}$$

Note that $D_{\text{pot}}(D_1, D_2)$ can be seen as the additive expectation defined by the LSD model.

Hence, the CI for the LSA model can be defined as follows:

$$\text{CI}_{\text{LSD}}(d_1, d_2) = \frac{d_{\text{comb}}(d_1, d_2)}{D_{\text{pot}}(D_1, D_2)}. \tag{5.14}$$

If the relative combination dose is lower than the more potent monotherapy, then the combination is deemed synergistic. Conversely, if the relative combination dose is greater than the more potent monotherapy, then the combination is deemed antagonistic.

5.3 Results

In this section, we use the compartment model described in Chapter 4 (Model MC) to: (1) investigate how the choice of reference model impacts the combinations that we deem synergistic and (2) explore new synergistic optimal combination doses by using the MOOCS-DS method.

5.3.1 Combinations Deemed Synergistic Depend on the Reference Model

We can qualitatively compare the combination doses that are predicted as synergistic by the four reference models to those deemed synergistic in an in vitro experiment performed by AstraZeneca [113]. Note that we cannot quantitatively compare them because the methods used to define synergy in the in silico experiments and in the in vitro experiments were different. In the experimental data, excess Loewe and fitted results were used to measure synergy, whereas, in the simulations, combination indices for each of the four reference models are used.

When using the Loewe additivity model, the experimental data deems all combination doses with more than 0.03 μM of ceralasertib or less than 0.3 μM of olaparib as synergistic (Figure 5.1 (a)), with the highest doses of both drugs being the most synergistic. In the experimental data, all combination doses exhibit growth inhibition and cytotoxicity (Figure 5.1 (b)). Using Model MC described in Chapter 4, we calculate the combination indices (CI) for the model using the synergy of efficacy models (Bliss and HSA) and the synergy of potency models (Loewe and LSD). The CIs are calculated using the effect defined in equation 5.1. The results are summarised in Figure 5.2, which displays the CI values of ceralasertib up to 1 μM

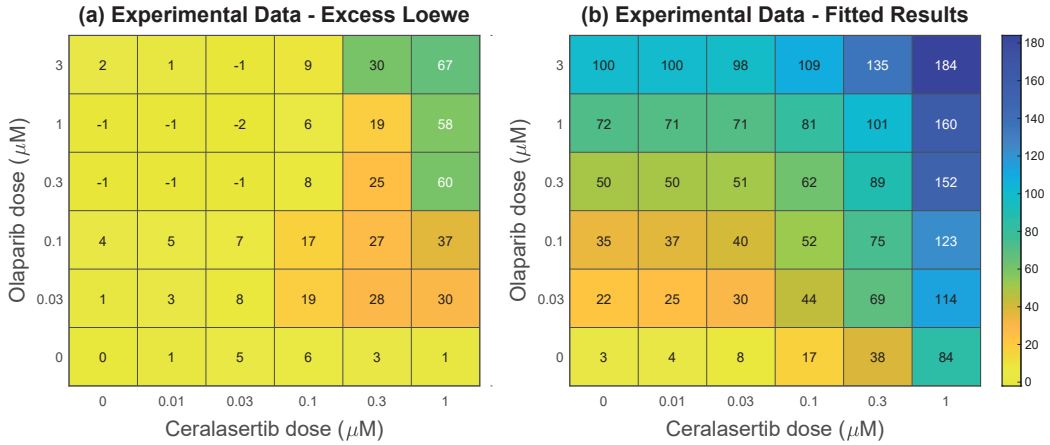

FIGURE 5.1: **In vitro data shows that ceralasertib and olaparib are synergistic in the FaDu ATM-KO cell line.** (a) Excess Loewe uses the Loewe additivity model to calculate the excess activity above what is expected from an additive combination. (b) Fitted results represent growth inhibition (0-100) and cytotoxic activity (100-200).

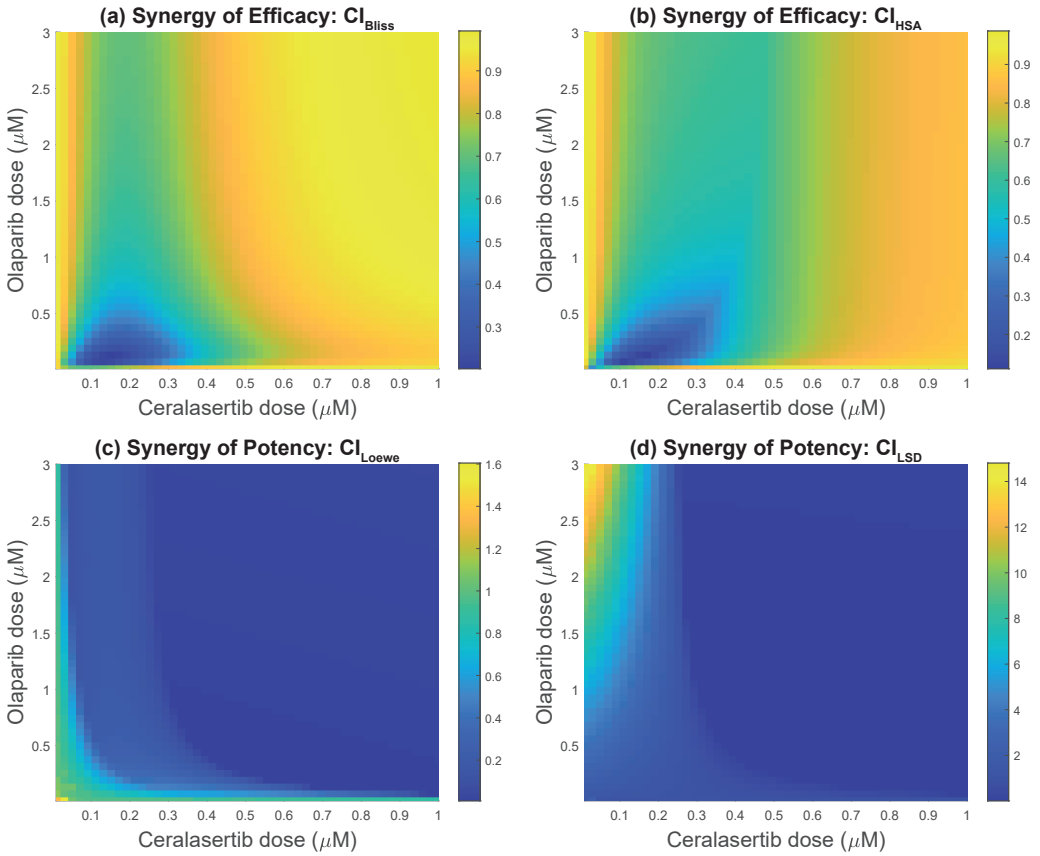

FIGURE 5.2: **The combination indices (CIs) for Model MC can deduce synergistic drug doses.** The top row shows the synergy of efficacy CI values using (a) Bliss and (b) HSA. The bottom row shows the synergy of potency CI values using (c) Loewe and (d) LSD. Drug combinations can have CI values that are greater than 1, equal to 1, and less than 1, which represent the combination being categorised as antagonistic, additive, or synergistic respectively. Note that the colour bars are different in Figures (a)-(d).

and olaparib up to 3 μM, using all four reference models. Note that the colour bars are different for each reference model.

The synergistic and antagonistic combinations can be seen more easily in Figure 5.3 which splits the drug combinations into 3 categories: (1) synergistic (CI values less than 1), (2) additive (CI values equal to 1), and (3) antagonistic (CI values greater than 1). Note that none of the CI values were exactly equal to 1, which means none of the drug combinations tested were deemed additive by the four reference models. Both the SoE models (Bliss and HSA) produced similar results and deemed all investigated combination doses as synergistic (blue colour in Figure

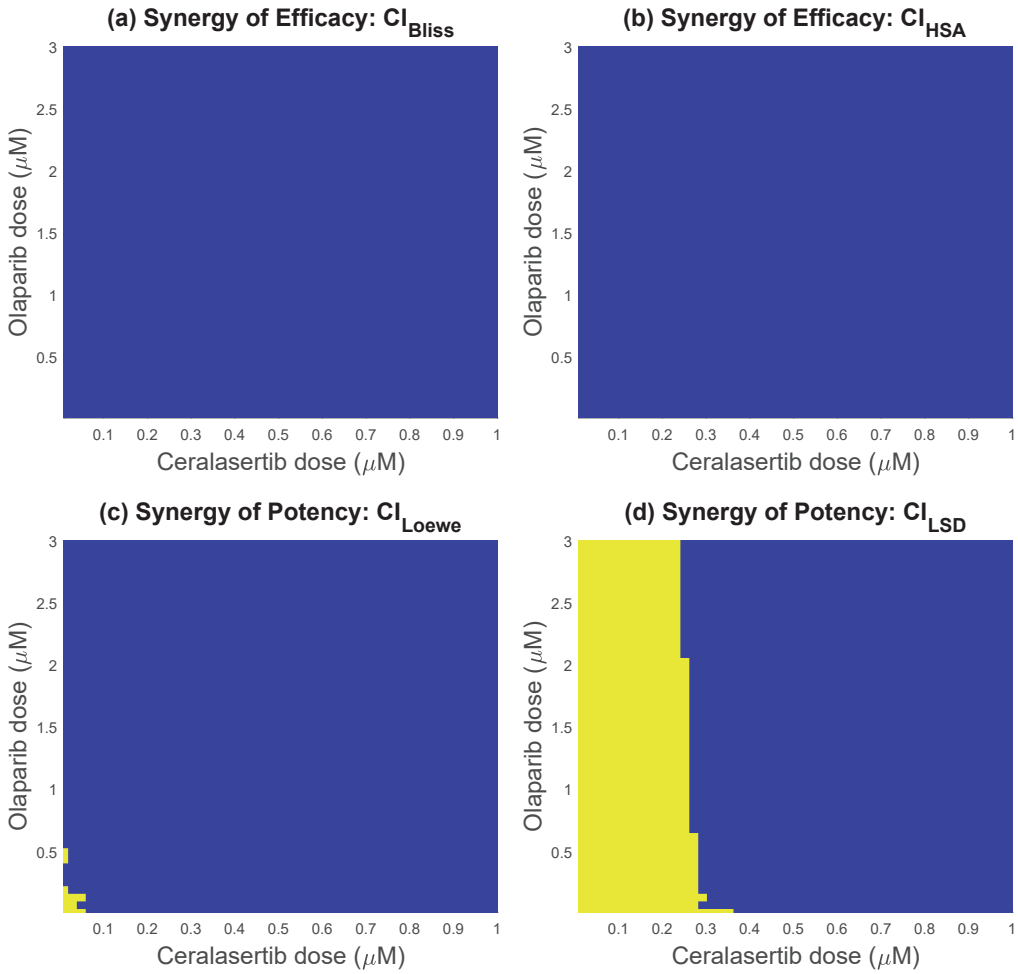

FIGURE 5.3: **The combination indices (CIs) for Model MC can deduce synergistic drug doses.** The top row shows the synergy of efficacy CI values using (a) Bliss and (b) HSA. The bottom row shows the synergy of potency CI values using (c) Loewe and (d) LSD. The CI values can be less than 1 which represents synergy (blue), or greater than 1 which represents antagonism (yellow).

5.3 (a) and (b)). The CI values for the Bliss are within the range 0.2023 to 0.993 and the CI values for HSA are within the range 0.1113 to 0.9865 (Figure 5.2 (a) and (b)). However, both SoP models (Loewe and LSD) deemed some investigated combination doses as antagonistic (yellow colour in Figure 5.3 (c) and (d)). The CI values for the Loewe additivity model are within the range 0.0075 (synergy) to 1.604 (antagonism), and the CI values for LSD are within the range 0.01 (synergy) to 14.8 (antagonism) (Figure 5.2 (c) and (d)). Loewe deemed only the very low combination doses as antagonistic, whereas LSD defined all combinations with less than 0.24

μM ceralasertib as antagonistic. LSD is the only reference model to agree with the experimental data in that combinations with low doses of ceralasertib and high doses of olaparib are antagonistic.

In summary, the combination doses that are classed as synergistic depend on how we define synergy (SoE or SoP). If we define synergy using SoE then all combination doses are defined as synergistic, but if we define synergy using SoP then some doses are deemed antagonistic. The drug interactions also depend on the reference model we use. The simulated synergy maps are very similar for Bliss and HSA, which means that the outcome is not dependent on how we define SoE. However, the reference models used in SoE (Loewe and LSD) produce significantly different synergy maps, which means that the outcome is impacted by how we define SoP. Overall, a commonality in all four reference models and the experimental data is that the highest doses of both drugs are determined as synergistic.

5.3.2 Pareto Fronts Can Find Optimal Drug Combinations

In this part of the study, we study the optimal combination doses. Following Gevertz *et al.* [62], we define four criterion spaces: Loewe-Bliss, LSD-Bliss, Loewe-HSA, and LSD-HSA. For each of the four criterion spaces, we find the Pareto fronts (Figures 5.4), which are the set of values for which one objective function cannot be improved without worsening a second objective function [62]. Here, each criterion space has two objective functions we aim to minimise, namely, the CI values for the reference models used in the criterion space. Note that we aim to minimise the CI values because synergy is defined when the CI value is less than one. The Pareto fronts are found using a grid search, which evaluates each combination of CI values and determines whether it is a Pareto optimal. From the Pareto fronts, we can find the Pareto optimal solutions (Figure 5.5), which are the set of drug doses corresponding to the CI values found using the Pareto fronts [62].

While the majority of the Pareto optimal solutions appear on only one Pareto front,

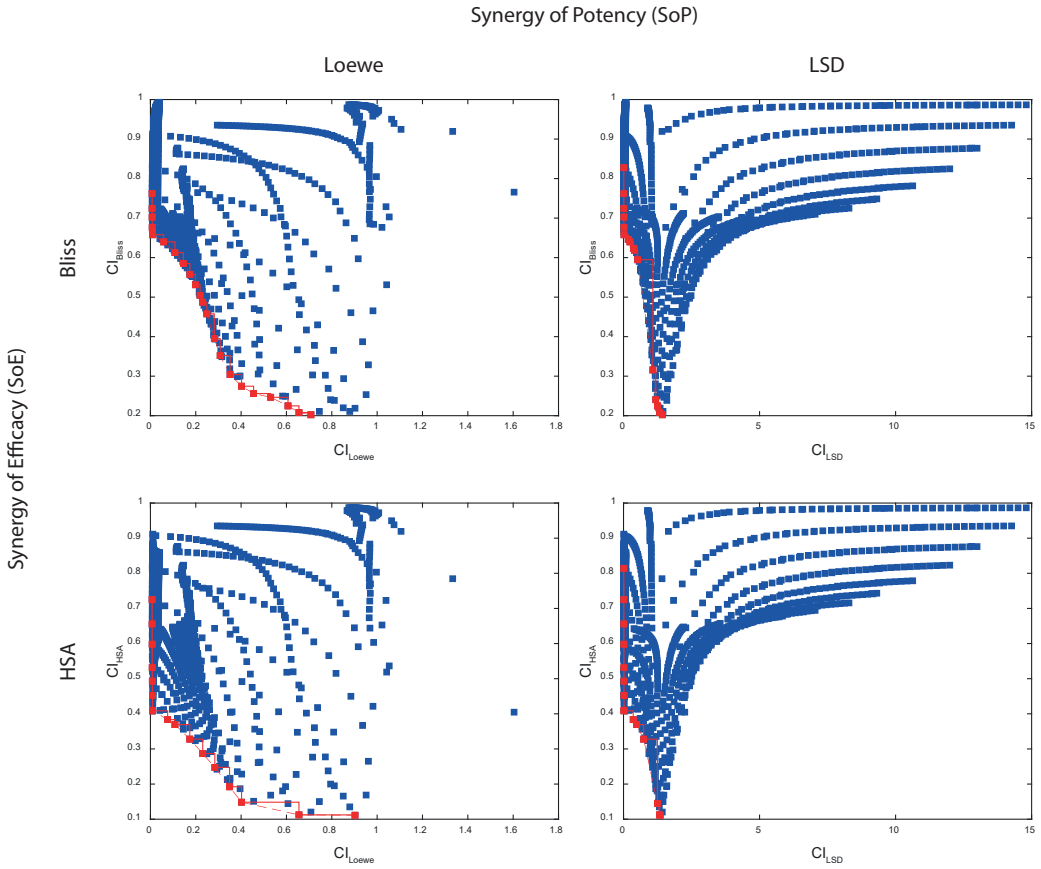

FIGURE 5.4: **The Pareto optimal solutions are the values for which you cannot improve the output of one reference model without making the result of the second reference model worse.** The Pareto fronts for Model MC are displayed in red in all four criterion spaces, with combinations that are not Pareto optimal in blue. The top row shows the Bliss model (SoE) and the bottom row shows HSA (SoE). The left column shows Loewe (SoP) and the right column shows LSD (SoP). Each scatterplot displays the CI values of the given reference models. Note that CI values less than one correspond to synergistic drug combinations.

47% of all Pareto optimal solutions appear on more than one Pareto fronts (Figure 5.5 (e)). Six Pareto optimal solutions are even deemed optimally synergistic in all four of the criterion spaces (indicated by a "4" in Figure 5.5 (e)). None of the Pareto optimal doses are equivalent to those used in experimental data (red dots in Figure 5.5 (e)). Interestingly, four out of the five combination doses investigated in vitro included drug doses that were a lot higher than the optimal synergistic doses found using the MOOCS-DS model. The highest Pareto optimal dose of ceralasertib found using the MOOCS-DS model is 0.68 μM, while the in vitro studies used doses of

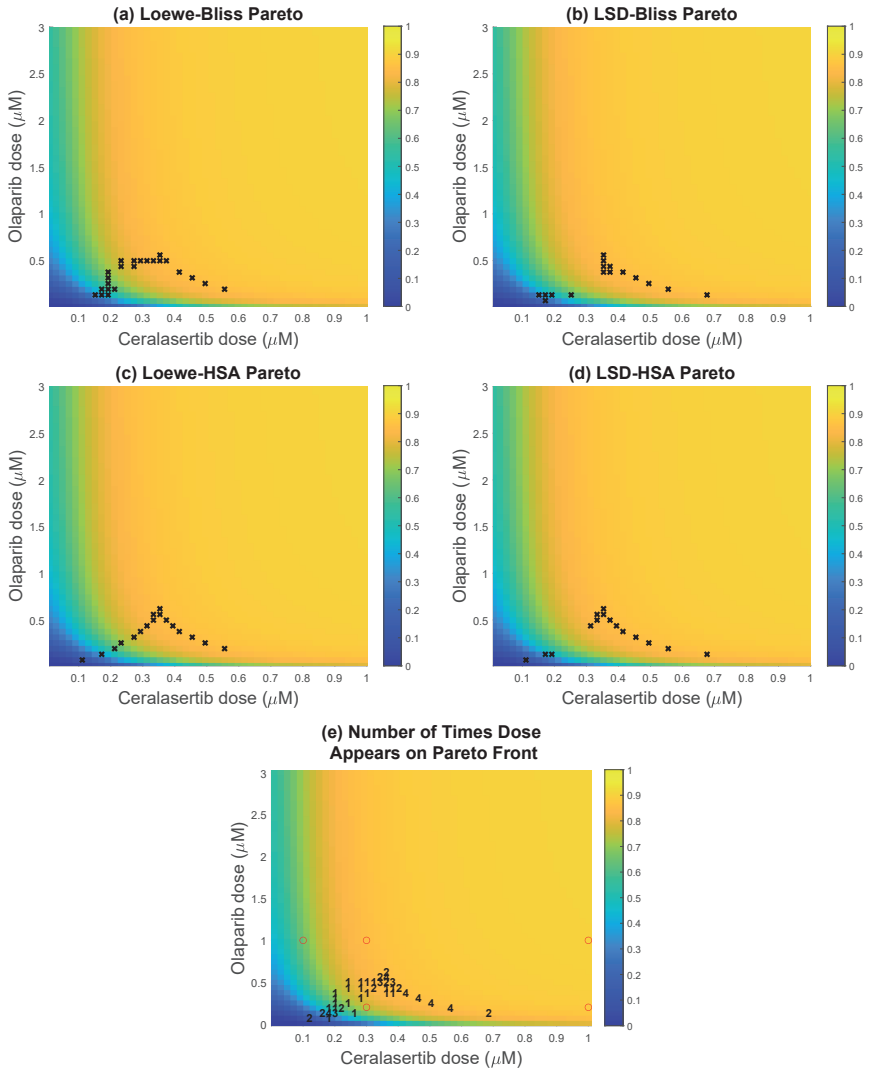

FIGURE 5.5: **The drug doses of ceralasertib and olaparib that are Pareto optimal using the four reference models can inform optimal doses for experimental validation.** Figures show the drug doses of ceralasertib (horizontal axes) and olaparib (vertical axes) of the Pareto optimal combinations. (a)-(d) The top row shows the Bliss model (SoE) and the bottom row shows HSA (SoE). The left column shows Loewe (SoP) and the right column shows LSD (SoP). (e) The number represents the number of criterion spaces that the combination is a Pareto optimal, i.e., a "4" indicates that this combination is Pareto optimal in all four criterion spaces. The red dots show the combinations used in experimental data 2. In Figures (a)-(e), the heatmap in the background shows the total growth inhibition of the combination compared to giving no drug (calculated by equation 5.1).

ceralasertib up to 1 μM. Similarly, the highest Pareto optimal dose of olaparib found using the MOOCS-DS model is 0.62 μM, while the in vitro studies used doses of olaparib up to 1 μM.

In summary, the synergistic combinations are sensitive not only to the definition of synergy (SoE and SoP) but also to the reference models within SoE and SoP.

5.4 Conclusion

In this Chapter, we have shown that the doses used in the combination treatment of ceralasertib and olaparib in the in vitro experiments are not necessarily the optimal doses. We have explored a range of combination drug doses that are within the maximal tolerated dose of each drug. We have found Pareto optimal combinations that use lower doses of both drugs compared to those used in the in vitro experiments. These Pareto optimal combinations found using the MOOCS-DS method can be used to guide the starting drug doses in future experimental studies, which may be more efficacious than those already studied in vitro.

Chapter 6

Multiscale Model: Investigating Spatio-Temporal Dynamics

6.1 Introduction

The interplay between drug-sensitive and drug-resistant cancer cells has been observed to impact treatment responses in experimental settings [47, 99, 136, 11]. This interplay is driven by cell-to-cell interactions, which, for example, are mediated by cells' ability to send and receive signalling molecules [7, 21] and compete for resources [172]. In this work, we are specifically interested in interactions between drug-sensitive and drug-resistant cancer cells that compete for one such resource: space. Cancer cells can express drug resistance in several ways. Here, we focus on two broad categories of drug resistance, namely intrinsic and inherited resistance. Intrinsic drug resistance refers to resistance that exists in cancer cells or tumours before they are subjected to treatments [181]. Inherited resistance occurs when drug-resistant parental cells pass on their drug-resistant traits to their daughter cells [57]. Cancer cells can be resistant to different types of therapies, including chemotherapy [140], radiotherapy [2], and targeted therapies, such as DDR inhibitor drugs [15] which are the focus of this thesis. Cancer cells that are resistant to multiple drugs simultaneously can be referred to as multi-drug-resistant [48].

In clinics, cancer drug treatments are commonly administered at maximum tolerated doses (MTDs). However, MTDs have been associated with rapid onsets of drug resistance [102]. As alternative treatment approaches to MTDs, drugs can be administered at low doses (i.e., lower than MTD doses) as part of single-drug or combination therapies. In fact, experimental results suggest that low-dose drug treatments can out-perform MTD strategies in certain in vitro experiments [113, 11, 176]. Beyond drug combinations and doses, another factor that may influence treatment responses is the spatial distribution of cancer cells [60, 98, 164]. With recent technological advances, there now exist methods that enable us to observe spatial organisations of different cell types within biopsied tumours. These methods include spatial transcriptomics [86] and mass spectrometry imaging [187]. Although these methods reveal spatial, intratumoural cell structures, they do not explicitly provide dynamic information about the interplay between different intratumoural cell types for example.

One way to study the dynamics of spatially structured cancer cell populations is through simulations and mathematical modelling. Indeed, several mathematical models have been developed for studying interactions between drug-sensitive and drug-resistant cancer cells. These include two-dimensional (2-D) agent-based models (ABMs) in which each agent typically represents one cancer cell [183]. For instance, Strobl *et al.* [168] used such a model to study the competition between drug-sensitive and drug-resistant cancer cell subpopulations during adaptive therapy treatments. The authors showed that not only the inter-subpopulation competition (between drug-sensitive and drug-resistant cells), but also the intra-population competition impact treatment responses in silico. Hamis *et al.* [72] also used a 2-D ABM to study the eco-evolution of cancer cell populations comprising drug-sensitive and drug-resistant cells. By including different types of drug-resistant cells in their model (e.g., cells that are drug-resistant before treatments start, and cells that become drug-resistant once they are exposed to drugs), the authors showed that the mechanisms by which cells are drug-resistant affect treatment responses

and optimal treatment strategies. In a third 2-D ABM, Bacevic *et al.* [11] simulated a cross-section through tumour spheroids with drug-sensitive and drug-resistant cells. They showed that drug-resistant cells on the periphery of the spheroid had a proliferative advantage over drug-resistant cells in the middle of the spheroid, which they attributed to a surplus of space and oxygen resources on the spheroid's periphery. A shared finding between the three aforementioned ABM studies is that the spatial composition of drug-sensitive and drug-resistant cells impacts cell population dynamics and treatment responses.

Inspired by these previous studies we, in this work, use a 2-D ABM to simulate the interplay between drug-sensitive and drug-resistant cancer cells in response to different drug combinations and doses. By including spatio-temporal dynamics in our mathematical model, we aim to understand how the spatial structure of cells, and the competition for space between drug-sensitive and drug-resistant cancer cells, impact treatment responses to drugs that inhibit a cancer cells' ability to repair DNA damage. We especially investigate how this resource competition affects the dynamic ratios of subpopulation sizes. Experimental studies have shown that cancer cells can be resistant to both ATR and PARP inhibitor drugs [138, 26, 15]. Population-level implications of cell-level resistance to the ATR inhibitor (ATRi) ceralasertib and the PARP inhibitor (PARPi) olaparib are mathematically and computationally studied in this work.

The aim of this study is to develop mathematical models to study the competition for space between drug-sensitive and drug-resistant cancer cells that are subjected to DDR inhibitor drugs. As a first step towards achieving this aim, we map the compartment model discussed in Chapter 4 (Model MC) onto a baseline, 2-D ABM (Section 6.2.1) in which all cells are fully drug-sensitive and the growth of the cell population size is minimally affected by spatial structures. The baseline ABM is calibrated by and evaluated against in vitro data (Section 6.2.2) from experimental data 2 (Section 1.3). To investigate how spatial cell structures, specifically cell

crowding effects, impact dynamics of heterogeneous cell populations in silico, we extend the baseline ABM to include spatial heterogeneity and drug-resistant cells. In this cell crowding limited ABM, drug-sensitive and drug-resistant cells are placed on the lattice in a variation of initial structures (Section 6.2.3). To ensure that our ABM-generated in silico results are based on enough simulations to mitigate uncertainty originating from intrinsic model stochasticity, we perform consistency analyses (Section 6.2.4).

6.2 Model and Method

6.2.1 Compartment Model: Incorporation Into an Agent-Based Model

As a first step towards studying spatial competition amongst cells (Section 6.2.3), we here map the compartment model (Model MC, Chapter 4) onto a baseline 2-D ABM (Figure 6.1 (a)). In the baseline ABM, cells progress through a drug-dependent cell cycle model (Sections 6.2.1.1 and 6.2.1.2) and exist on a 2-D lattice in which each lattice site can either be occupied by a drug-sensitive cancer cell or be empty (Section 6.2.1.3).

6.2.1.1 Modelling the Cell Cycle

Each agent (i.e., cell) in the ABM progresses through the cell cycle via an agent-intrinsic cell cycle model. The model consists of a set of nodes that represent cell cycle states and edges that represent paths between states (Figure 6.1 (a)). In the ABM, we include the cell cycle states in the compartment model (Chapter 4) and an additional quiescent state, G0 (Figure 6.1 (a)). The G0 state is introduced to achieve growth inhibition by spatial limitations. Cells in the ABM are equipped with a cell cycle clock that monitors their progression through the cell cycle and determines when they leave compartments according to allocation times that are estimated from in vitro data (Section 6.2.2). For each cell, cell_j, in the system, the clock starts when the cell enters the G1 state and terminates when the cell reaches its individual

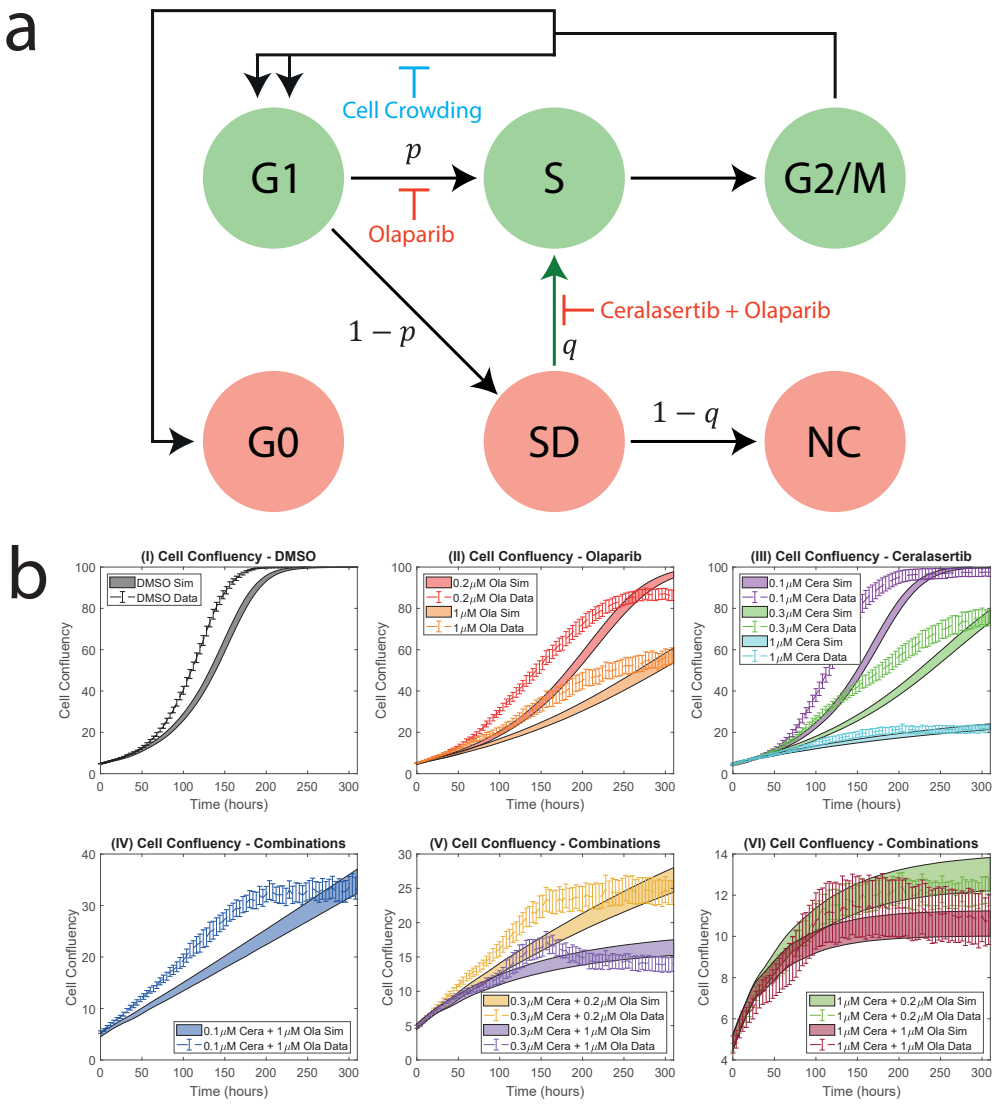

FIGURE 6.1: **The ABM is parameterised and evaluated against in vitro experimental data 2.** (a) In the ABM, cells can be in undamaged and cycling (green nodes) or damaged and/or non-cycling (red nodes) cell cycle states. Cells can progress through the undamaged states (G1, S, and G2/M) and damaged states (SD, NC). Cell-crowding may also cause cells to enter the additional G0 state that represents quiescent cells. Each cell in the ABM has an individual cell cycle clock that tracks its progression through the cell cycle. Cells in state SD experience DNA replication stress and cells in state NC have irreparable DNA damage. p and q represent drug-dependent probabilities that a particular path will be chosen at a fork. The PARPi inhibits cells from progressing from state G1 to S. The green path represents DNA damage repair, which is inhibited by both the ATRi and the PARPi. The time and drug dependencies of the parameters in (a) have been omitted for ease of presentation. (b) The parameter v_B, which denotes the neighbourhood order in which daughter cells can be placed in the ABM, is calibrated from the in vitro data. Other parameter values are read from the in vitro data and mapped from the compartment model. The plots show simulated and experimental cell confluency over 310 hours for various dose combinations of the ATRi and PARPi. Training data is used to estimate v_B (plots I-V) and test data is used to evaluate the model (plot VI). The solid curves represent the simulation results from the ABM. The dashed curves represent the mean in vitro data, with the standard error of the mean for 3 experiments indicated with error bars.

doubling time, T_j, i.e., the time cell_j takes to complete one cell cycle and divide into two daughter cells. The doubling time is chosen from a normal distribution with mean value τ and standard deviation σ. Here, τ and σ are estimated from experimental data, where σ is chosen to achieve asynchronously dividing cell populations, as observed in the regarded in vitro experiments (Section 6.2.2). Note that if $\sigma = 0$, then every dividing cell on the lattice will produce daughter cells at the same time. When a focal cell's internal cell cycle clock terminates and the cell leaves the G2/M state, it attempts to produce a daughter cell (Section 6.2.1.3). If there are no available lattice sites on which to place the daughter cell, the cell division fails and the focal cell enters the G0 state. A cell that enters G0 will remain there for the remainder of the simulation. To represent cell cycle arrest, a cell's internal cell cycle clock is paused when a cell is in the SD state.

6.2.1.2 Modelling DDR Inhibitor Drugs

As in the compartment model, the edges in the ABM are assigned weights that are functions of drug doses. The weights denote probabilities with which paths in the cell cycle model are taken. To decide which path is taken at forks, random numbers between zero and one are generated from uniform distributions. If a generated random number at the post-G1 fork is smaller than $p([\text{drug}_{\text{Ola}}])$ (equation 4.5), cells evade the effect of olaparib and enter state S. Similarly, if the random number generated at the post-SD fork is smaller than $q([\text{drug}_{\text{Cera}}], [\text{drug}_{\text{Ola}}])$ (equation 4.6), cells evade drug effects and enter state S. Drugs are administered at the start of the in silico experiments and are modelled to be constant throughout time and space in the simulations. This mimics an in vitro experiment without drug elimination.

6.2.1.3 Cells Co-exist on a Lattice

The ABM comprises 100×100 lattice sites that can be occupied by one cell or be empty. The baseline ABM has no-flux boundary conditions, which are chosen to represent a physical boundary in an in vitro experiment. No-flux boundary

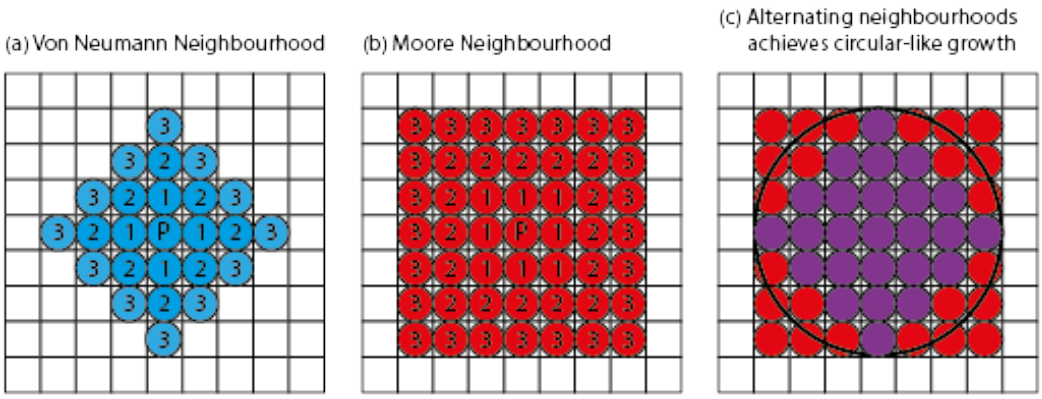

FIGURE 6.2: **Daughter cells are placed using both von Neumann and Moore neighbourhoods to achieve circular-like growth of the cancer cells.** If $v_B = 3$, when a parental cell divides, a daughter cell gets placed in the 1st, 2nd, or 3rd O.N of the parental cell using either (a) the von Neumann neighbourhood or (b) the Moore neighbourhood. The numbers in the figure indicate the order of the neighbourhood and P indicates the parental cell. (c) Every time a cell divides in the ABM, the choice of von Neumann neighbourhood or Moore neighbourhood is randomly selected to achieve a circular-like growth of the cells.

conditions ensure cells on the edge of the lattice cannot place daughter cells beyond the lattice boundary [143]. At the start of the simulations, P_0 cells are seeded on the lattice. The cells are randomly scattered across the lattice and are initiated in different cycling cell cycle states (i.e., G1, S, SD, G2/M), according to a cell cycle distribution frequency that is estimated from in vitro data (Section 6.2.2) and correspond to the factors $G1_0, S_0, SD_0, G2/M_0$ in equations 4.2a-e. When the cell population, $P(t)$, has reached a critical size P^*, the drugs are applied to the system. P^* is stochastic and estimated from in vitro data (Section 6.2.2).

In the ABM, when a cell reaches the end of its cell cycle doubling time, it divides and a daughter cell is placed on the lattice. Daughter cells can be placed using von Neumann neighbourhoods (Figure 6.2 (a)) or Moore neighbourhoods (Figure 6.2 (b)). To achieve circular-like growth of the cells, each time a cell in the model divides, the choice of which neighbourhood (von Neumann or Moore) a daughter cell is placed in is randomly selected (Figure 6.2 (c)). Note that lower order neighbourhoods (O.N.s) are prioritised over higher O.N.s. The lattice points adjacent to the parental cell consist of the 1st O.N. of the parental cell. If scheduled for division, a daughter

cell will be placed in a random location in the 1st order von Neuman/Moore neighbourhood. If all eligible lattice points in the chosen neighbourhood are occupied by cells, the daughter will be placed randomly in the 2nd O.N. Similarly, if there is no free lattice point in the 2nd O.N., the daughter cell may be placed in the 3rd O.N, and so on up to the v_Bth O.N. [76]. To simulate growth inhibition caused purely by a lack of space to divide, if all cells up to and including the v_Bth O.N. are occupied by cells, the parental cell will go into quiescence, where it will remain for the duration of the in silico simulation. Here, v_B is the number of neighbourhoods in which daughter cells can be placed and is estimated from in vitro data (Section 6.2.2).

6.2.2 Model Parameterisation

The ABM parameters are estimated from an in vitro experiment in which FaDu ATM-KO cells were subjected to one or two DDR inhibitor drugs [113]. Cell confluency and cell death data were reported for 0-310 hours, and pulse-chase data were reported for 0-24 hours. First, some ABM model parameters ($C_{\text{ABM}}, q_0, p_0, E_{\text{max},1}$,

Parameter Name	**Parameter Value**	**Parameter Description**
$G1_0$	0.36	The fraction of cells in state G1 at the start of the simulation.
S_0	0.14	The fraction of cells in state S at the start of the simulation.
SD_0	0.04	The fraction of cells in state SD at the start of the simulation.
$G2/M_0$	0.46	The fraction of cells in state G2/M at the start of the simulation.
NC_0	0	The fraction of cells in state NC at the start of the simulation.
$G0_0$	0	The fraction of cells in state G0 at the start of the simulation.

TABLE 6.1: **Initial conditions are estimated from in vitro experimental data 2.** The initial fraction of cells in states G1, S, SD, and G2/M are estimated from pulse-chase data. At the start of the simulations, no cells are in the non-cycling states NC and G0.

Parameter Name	Parameter Value	Parameter Description
Parameter values that are estimated by fitting the compartment model to in vitro data.		
p_0	0.3558	The probability that cells transition from state G1 to S.
q_0	1	The probability that cells transition from state SD to S.
$E_{\max,1}$	1	The maximal drug effect of ceralasertib.
$E_{50,1}$	0.2579 μM	The concentration of ceralasertib that results in half the maximal effect.
h_1	1.5187	The Hill coefficient of ceralasertib.
$E_{\max,2}$	0.5609	The maximal drug effect of olaparib.
$E_{50,2}$	0.1275 μM	The concentration of olaparib that results in half the maximal effect.
h_2	1.0962	The Hill coefficient of olaparib.
Parameter values that are estimated by fitting the agent-based model to in vitro data.		
C_{ABM}	10,000 cells	The carrying capacity in the agent-based model.
P_0	$N \cdot n$ cells	The number of seeded cells in the agent-based model. N and n respectively denote the number of seeded clusters and the number of cells per seeded cluster (Section 6.2.3).
$P^* \sim U(\mu_{P^*} \pm 3\sigma_{P^*})$	μ_{P^*} = 482 cells σ_{P^*} = 21 cells	The number of cells when the drugs are administered is picked from a uniform distribution.
$T_j \sim N(\tau, \sigma^2)$	τ = 41 hours σ = 8.2 hours	The doubling time of cell$_j$ is picked from a normal distribution.
τ_{G1}	0.36	The fraction of a cell's doubling time spent in state G1.
τ_S	0.18	The fraction of a cell's doubling time spent in state S.
τ_{SD}	0.04	The fraction of a cell's doubling time spent in state SD.
$\tau_{G2/M}$	0.46	The fraction of a cell's doubling time spent in state G2/M.
v_B	3 lattice sites	The neighbourhood-order in which daughter cells can be placed in the baseline agent-based model.
Parameter values that are chosen in the cell crowding limited ABM (Section 6.2.3).		
v_C	1 lattice site	The neighbourhood-order in which daughter cells can be placed in the cell crowding limited agent-based model.

TABLE 6.2: **Parameter values are estimated from in vitro experimental data 2.** The table displays the parameter values that are used in the ABMs.

$E_{50,1}, h_1, E_{\max,2}, E_{50,2}, h_2$) are directly mapped from the compartment model. Thereafter, some ABM-specific parameters ($\tau_{G1}, \tau_S, \tau_{SD}, \tau_{G2/M}, \tau, \mu_P, \sigma_P$) are directly read from the in vitro data. Lastly, the parameter v_B is estimated by matching simulation

outputs to in vitro data (see Appendix A.4.1 for more details).

The ABM-specific carrying capacity is $C_{\text{ABM}} = 10,000$, which represents the total number of lattice sites. Initially, P_0 cells are seeded on the lattice in varying cluster sizes. Since we seed the cells in one or multiple clusters, the value of P_0 depends on N (the number of clusters) and n (the number of cells in each cluster) such that $P_0 = N \cdot n$. The time, t_d, at which the total cell population $P(t_d) = P^*$ is when the drugs are administered and the in silico experiments start. To create diversity in initial cell configurations, we ensure that $P_0 < \mu_{P^*}$, which allows for cell proliferation before drug administration. The value of P^* is randomly chosen for each simulation by sampling from a uniform distribution with values in the range $[\mu_{P^*} - 3\sigma_{P^*}, \mu_{P^*} + 3\sigma_{P^*}]$. Both μ_P^* and σ_P^* are estimated using the in vitro cell confluency data in the absence of drugs. The value of μ_{P^*} is estimated to be 482, calculated by multiplying the initial mean cell confluency (4.82%) by the carrying capacity, C_{ABM}. Similarly, the initial standard deviation for the in vitro cell confluency is 0.21, thus $\sigma_{P^*} = 21$. From the in vitro data, we observe a varied standard error of margin for the initial cell confluency. Hence, to fit the ABM to data, we take the uniform distribution to be plus or minus 3 standard deviations of the mean, μ_{P^*}.

In the ABMs, a cells' doubling time is chosen from a normal distribution with mean $\tau = 41$ hours, which is the doubling time of FaDu ATM-KO cells, and standard deviation $\sigma = 8.2$ hours. We choose a standard deviation equal to 20% of the mean to achieve an asynchronous population as observed in the in vitro data. As in the compartment model, we seed the cells in different cell cycle states, estimated from the pulse-chase data. Since we assume that all initially seeded cells are either cycling or can become cycling, none of the seeded cells are in the NC state or the G0 state. We assume that $G1_0$, $S_0 + SD_0$, and $G2/M_0$ are the fraction of a cell's doubling time spent in the G1, S, and G2/M state respectively. This is because we assume that the SD state is a sub-state of S, where cells are arrested in the S phase due to

DNA damage. To represent cell cycle arrest, we assume that cell cycle progression is halted and the time spent in the SD state does not contribute towards the cell's doubling time. To account for this in the ABM, we use a separate clock to track how long a cell will spend in the SD state. The fraction of time cells spend in SD (τ_{SD}) is calculated as a fraction SD_0 of the cell's doubling time. Note that the cells are seeded at a random time during their assigned cell cycle state, chosen from a uniform distribution ranging from the start to the end time of the corresponding state.

When we calibrate the baseline ABM to the in vitro cell confluency data, we investigate various values of v_B and conclude that placing daughter cells within 3rd order-neighbourhoods can achieve a logistic growth curve most similar to that of the data (see Appendix A.4.1 for more details). When we extend the baseline ABM to the cell crowding limited ABM, we choose to limit parental cells to place daughter cells in the first order-neighbourhood to emphasise the spatial limitations of cell division caused by cell crowding. The remaining parameters (q_0, p_0, $E_{\max,1}$, $E_{50,1}$, h_1, $E_{\max,2}$, $E_{50,2}$, h_2) are taken directly from the compartment model. Parameter values related to the initial conditions are listed in Table 6.1 and all other parameters are listed in Table 6.2.

Since the ABM (Figure 6.1 (a)) is able to satisfactorily predict unseen time series data (Figure 6.1 (b)), we argue that the model is appropriate for our current study which aims at modelling cell population dynamics in response to 0.1-1 μM ceralasertib doses and 0.2-1 μM olaparib doses.

6.2.3 Spatio-Temporal Cell Population Dynamics: An Agent-Based Model

To investigate the role of space in the competition between drug-sensitive and drug-resistant cancer cells, we extend the baseline ABM (Section 6.2.1) to: (1) include both drug-sensitive and drug-resistant cells, and (2) include spatial limitations by cell crowding. In the model, drug-resistant cells can be intrinsically resistant to

ceralasertib (ATRi), olaparib (PARPi), or to both ceralasertib and olaparib. The latter case simulates multi-drug resistance. Furthermore, we incorporate inherited resistance into the model so that drug-resistant parental cells pass on their drug-resistant traits to their daughter cells. In the cell crowding limited ABM, parental cells may only place daughter cells in their immediate neighbourhoods, i.e., in first-order neighbourhoods, such that $v_C = 1$. To ensure that this spatial competition is an effect of cell crowding and not the boundary, we use periodic boundary conditions in this part of the study. This means that cells on the left edge of the lattice can place cells on the far right edge and cells on the top edge of the lattice can place cells on the far bottom of the lattice, and vice versa [143]. Note that we also repeat all of the experiments in Section 6.3 with no-flux boundary conditions and there is no significant difference in the model output compared to the periodic boundary conditions (See Appendix A.4.2).

To investigate how various cell-level and population-level properties impact the competition for space amongst cancer cells, we vary six factors in the initial cell configurations of the ABM, as listed in 1-6 below.

1. The cells are seeded in different spatial configurations on the lattice (Figure 6.3).
2. The initial fraction of drug-resistant cells is either 0.1 or 0.3.
3. The drug-resistant cells are resistant to ceralasertib, olaparib, or both ceralasertib and olaparib.
4. Cells are treated with either ceralasertib monotherapy, olaparib monotherapy, or combination therapy.
5. Drugs are given at higher doses (1 μM ceralasertib, 1 μM olaparib), or lower doses (0.3 μM ceralasertib, 0.2 μM olaparib).
6. The doubling time of drug-resistant cells is varied in relation to the doubling time of drug-sensitive cells.

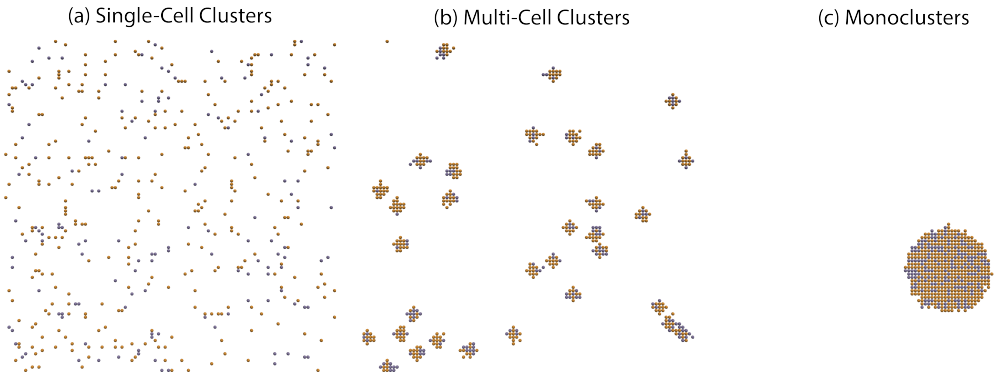

FIGURE 6.3: **In the cell crowding limited ABM, cells are initiated in (a) single-cell clusters, (b) multi-cell clusters, or (c) monoclusters.** In (a,b,c), we seed P_0 cells on the lattice, where $0.7P_0$ cells are drug-sensitive (orange) and $0.3P_0$ cells are drug-resistant (purple). The example snapshots in (a,b,c) are taken when the total cell counts have reached the critical value P^* which is chosen stochastically and determines when drugs should be applied.

LIST 6.1: To investigate the spatial competition between drug-sensitive and drug-resistant cells in response to drug treatments, we vary items 1-6 in simulation experiments.

To achieve different spatial configurations (Item 1, List 6.1), we seed the cells in different-sized clusters. We let N denote the total number of initial clusters on the lattice and n denote the total number of cells in each seeded cluster. Examples of initial cell configurations with $N = 419$, 32, and 1 cluster are shown in Figure 6.3 (a)-(c) respectively, where the fraction of drug-resistant cells is 0.3.

6.2.4 Consistency Analysis

Before proceeding to the result-generation, we note that simulation stochasticity arises from multiple sources in the ABMs: the initial cell configurations (Section 6.2.1.3), the placement of daughter cells (Section 6.2.1.3), the paths taken in the cell cycle model and the cell doubling times (Section 6.2.1.1), and drug responses (Section 6.2.1.2). Moreover, we would like to report our result with summary statistics that are averaged over multiple simulations. This begs the question: How many simulations do we need to run in order to report meaningful results that mitigate uncertainty originating from intrinsic model stochasticity? One way to answer this question is through performing a consistency analysis. The process is

described in detail by Hamis *et al.* [74] which builds on previous statistical work by Vargha *et al.* [177] and Alden *et al.* [4].

For this study, we perform a consistency analysis on the cell crowding limited ABM where cells are seeded on the lattice in single-cell clusters and no drug-resistant cells are included. We choose two output variables of interest: the cell confluency with 0.3 μM ceralasertib and 0.2 μM olaparib, both halfway through (X_1) and at the end (X_2) of the simulations. We choose this combination treatment to ensure we have stochasticity from both drugs, without non-cycling cells having a significant effect on the cell confluency output. We seek the smallest number of in silico simulations, d, needed to be run per experiment that mitigates uncertainty originating from intrinsic model stochasticity, i.e., the smallest d to produce a small statistical significance. In this study, we test values of d =1, 5, 50, 100, and 300 [74]. This can be viewed as a one-dimensional constrained optimisation problem defined as:

$$\min\{d : \hat{A}(d) \leq 0.56\}. \tag{6.1}$$

When conducting consistency analysis, one in silico simulation produces one data sample of the chosen variables X_i. We generate distributions of data samples with varying sizes, where a distribution with distribution-size d has d data samples. We produce distribution groups, g_d, each comprising 20 distributions of distribution-size d, i.e., a group, g_1, comprising 20 distributions of size $d = 1$, another group g_5 comprising 20 distributions of size $d = 5$, etc. Overall, we have to produce $20(1 + 5 + 50 + 100 + 300) = 9120$ data samples to perform the consistency analysis. In each distribution group, g_d, we compute the $\hat{A}$-measure, $\hat{A}^{g_d}_{1,k'}(X_i)$, for each variable X_i to compare the 1$^{\text{st}}$ and the k'^{th} distributions, $k' = 2, 3, \ldots, 20$ (equations 6.2 and 6.3) [74]. This deduces how stochastically equal the two distributions are.

Let B and C be two distributions comprising m_1 and m_2 data samples respectively

of some variable X such that $B = \{b_1, b_2, \ldots, b_{m_1}\}$ and $C = \{c_1, c_2, \ldots, c_{m_2}\}$. The $\hat{A}$-measure is calculated as follows:

$$\hat{A}_{BC}(X) = \frac{1}{m_1 m_2} \sum_{i=1}^{m_1} \sum_{j=1}^{m_2} H(b_i - c_j), \tag{6.2}$$

where:

$$H(x) = \begin{cases} 1 & \text{if } x > 0, \\ \frac{1}{2} & \text{if } x = 0, \\ 0 & \text{if } x < 0. \end{cases} \tag{6.3}$$

In other words, we compare all values b_i, $i = 1, \ldots, m_1$ in distribution B to values c_j, $j = 1, \ldots, m_2$ in distribution C and give them a score of 0, 0.5, or 1. To deduce how stochastically equal distributions B and C are, we calculate the $\hat{A}$-measure, $\hat{A}_{BC}(X) \in [0, 1]$, by averaging the sum of the scores by dividing by $m_1 m_2$. If all values b_i are bigger than all values c_j, the $\hat{A}$-measure value is 1. Similarly, if all values b_i are smaller than all values c_j, the $\hat{A}$-measure value is 0. The closer the value of $\hat{A}_{BC}(X)$ is to 0.5, i.e., when the values b_i are bigger than c_j half of the time, the more stochastically equal distributions B and C are with regard to the variable X. However, we are only interested in how much the distributions are equal, not which distribution is stochastically greater. Hence, to omit direction we calculate the scaled $\hat{A}$-measure, denoted $\underline{\hat{A}} \in [0.5, 1]$ [74], given by

$$\underline{\hat{A}}_{BC}(X) = \begin{cases} \hat{A}_{BC}(X_i) & \text{if } \hat{A}_{BC}(X_i) \geq 0.5, \\ 1 - \hat{A}_{BC}(X_i) & \text{if } \hat{A}_{BC}(X_i) < 0.5. \end{cases} \tag{6.4}$$

For each group, g_d, we calculate the maximal scaled $\hat{A}$-measure, $\underline{\hat{A}}^{g_d}_{\max}$, and compare it to threshold values (equation 6.5) to deduce whether the statistical significance

between the two distributions is small, medium, or large [74, 36]. These threshold values are given by:

$$\text{Statistical Significance} = \begin{cases} \text{small} & \text{if } \underline{\hat{A}}^{g_d}_{\max}(X) \in [0.5, 0.56], \\ \text{medium} & \text{if } \underline{\hat{A}}^{g_d}_{\max}(X) \in (0.56, 0.64], \\ \text{large} & \text{if } \underline{\hat{A}}^{g_d}_{\max}(X) \in (0.64, 0.71]. \end{cases} \tag{6.5}$$

We assume that if the maximal scaled $\hat{A}$-measure is greater than 0.71, the statistical significance between the two distributions is extremely large. Hence, we want to find the smallest value of d such that $\underline{\hat{A}}^{g_d}_{\max} \leq 0.56$, i.e., the smallest distribution-size d yielding a small stochastic significance for all 19 $\hat{A}$-measures [74].

We conclude from Figure 6.4 and Table 6.3 that $d = 100$ is the smallest tested value of d that has a maximum scaled $\hat{A}$-measure value under the threshold value 0.56 for both outputs X_1 and X_2. Therefore, 100 simulation runs per in silico experiment will suffice to form the basis for our reported results. Note that Figure A.18 in Appendix A.4.3 show the $\hat{A}$-values in both the initial and scaled form for each distribution size d.

Distribution Size	d=1	d=5	d=50	d=100	d=300
Output X_1 (half time)	1	0.92	0.5894	0.5539	0.5287
Output X_2 (end time)	1	0.92	0.5990	0.5569	0.5341

TABLE 6.3: **Scaled $\hat{A}$-measure calculate how stochastically equal two distributions are.** The table shows the scaled $\hat{A}$-measure values for distribution sizes d =1, 5, 50, 100, and 300 relating to both output variables; the cell confluency halfway through the experiment (X_1) and at the end of the simulation (X_2) for 0.3μM ceralasertib and 0.2μM olaparib.

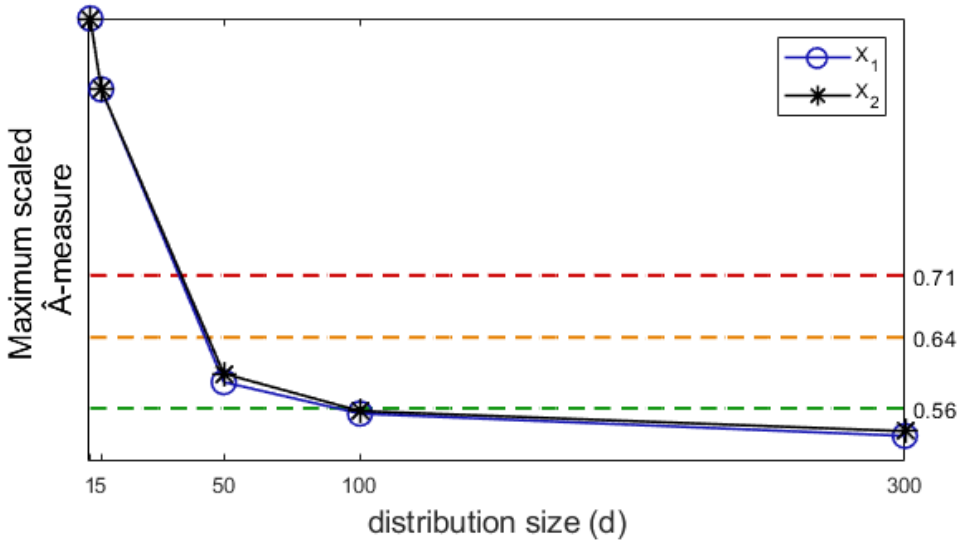

FIGURE 6.4: **A consistency analysis is performed to decide how many in silico simulations are needed to make conclusions from the ABM to mitigate any model uncertainty arising from intrinsic-model stochasticity.** The figure shows the maximal scaled $\hat{A}$-measures (vertical axis) for different distribution sizes (horizontal axis) relating to two output variables: the cell confluency for 0.3μM ceralasertib and 0.2μM olaparib half-way through (X_1) and at the end of the simulation (X_2). We generate distribution groups each comprising 20 distributions, i.e., 20 simulations of size d. To see how equal two distributions are, the $\hat{A}$-measures are calculated by comparing distributions 1 and k' for our chosen output variables, where $k' = 2, 3, \ldots, 20$. Each $\hat{A}$-measure produces a value between 0 and 1, where a value of 1 means the first distribution group is stochastically greater and a value of 0 means the second distribution group is stochastically greater. To omit which of the distributions are greater, and see only how equal the two distributions in question are, we scale these $\hat{A}$-values to generate values between 0.5 and 1. We then take the maximum value in each group to get the maximum scaled $\hat{A}$-measure. We seek the smallest d that produces a small statistical significance, i.e., scaled $\hat{A}$-values below the green line. Scaled $\hat{A}$-values between the green and orange line have a medium stochastic significance and scaled $\hat{A}$-values between the orange and red lines have a large stochastic significance.

6.3 Results

6.3.1 The Spatial Structure of Cells Impacts Cell Population Responses

We perform a series of in silico experiments that are designed to investigate the dynamics of simulated cell populations in which drug-sensitive and drug-resistant cells co-exist and compete for space. In the first experiment, we aim to elucidate how the competition between drug-sensitive cells and cells that are resistant to both ceralasertib and olaparib is impacted by spatial cell configurations. To do this, we

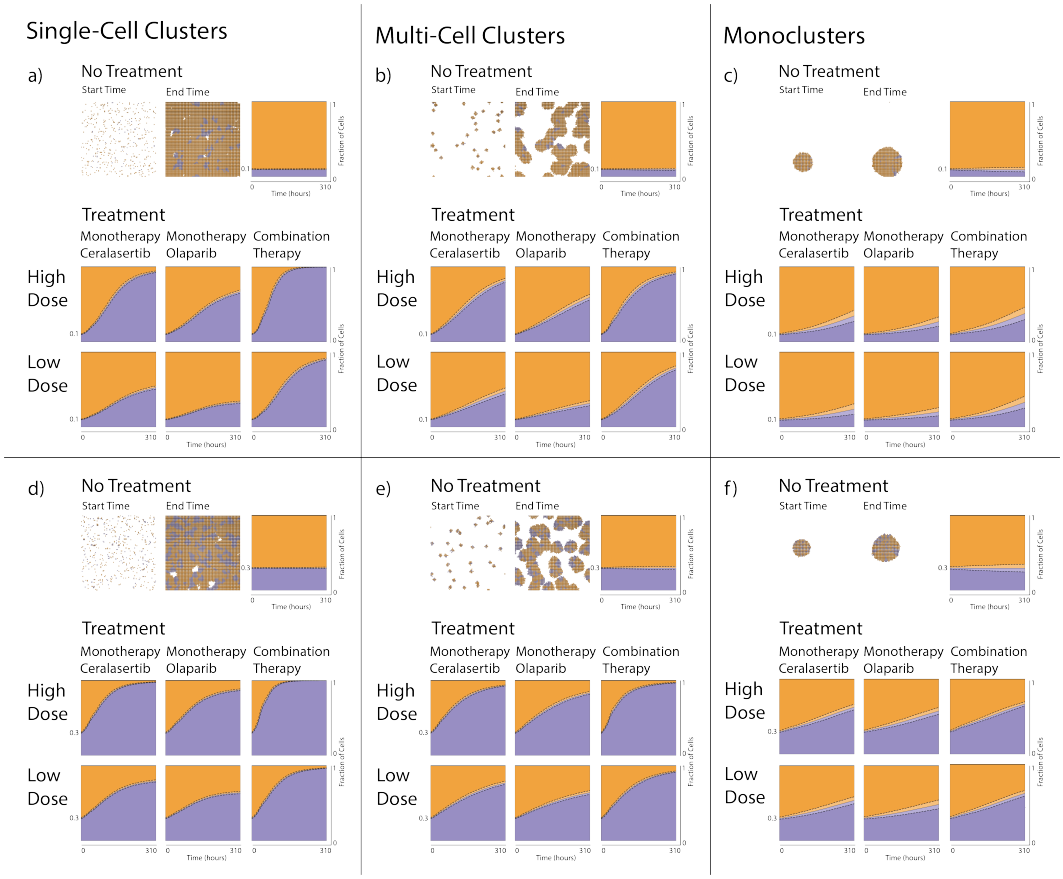

FIGURE 6.5: **Cells that are resistant to an ATRi (ceralasertib) and a PARPi (olaparib) compete for spatial resources with drug-sensitive cells.** P_0 cells are randomly seeded on the lattice in single-cell clusters (a,d), multi-cell clusters (b,e), or monoclusters (c,f), with either $0.1P_0$ (a,b,c) or $0.3P_0$ (d,e,f) drug-resistant cells. Simulations are performed with no drugs (top row in each panel a-f), ceralasertib monotherapy (left column of the treatment section in each panel a-f), olaparib monotherapy (middle column of the treatment section in each panel a-f), and combination therapy (right column of the treatment section in each panel a-f) for high (middle row in each panel a-f) and low (bottom row in each panel a-f) doses. Examples of initial and final simulation snapshots are shown in each panel a-f with drug-sensitive (orange) and drug-resistant (purple) cells. Panels a-f also include plots of the dynamic mean fraction of drug-sensitive (orange) and drug-resistant (purple) cells, and standard deviations (dashed curves) from 100 simulation runs.

initiate the silico experiments by seeding P_0 cells on the lattice in three different configurations: single-cell clusters, multi-cell clusters, and monoclusters (Item 1, 6.1; Figure 6.3). For each of these configurations, we vary the initial fractions of drug-resistant cells (Item 2, 6.1), drug treatments (Item 4, 6.1), and drug doses (Item 5, 6.1). The results from these experiments are summarised in Figure 6.5, where we

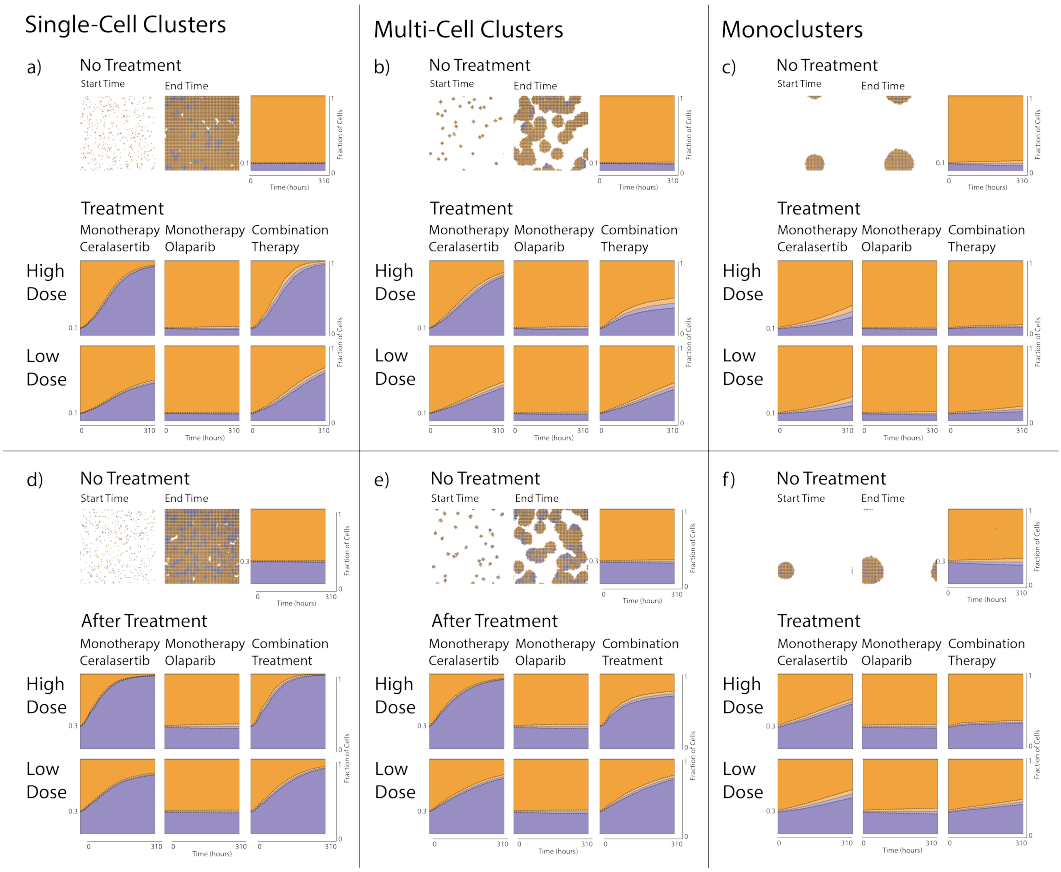

FIGURE 6.6: **Cells that are resistant to an ATRi (ceralasertib) compete for spatial resources with drug-sensitive cells.** P_0 cells are randomly seeded on the lattice in single-cell clusters (a,d), multi-cell clusters (b,e), or monoclusters (c,f), with either $0.1P_0$ (a,b,c) or $0.3P_0$ (d,e,f) drug-resistant cells. Simulations are performed with no drugs (top row in each panel a-f), ceralasertib monotherapy (left column of the treatment section in each panel a-f), olaparib monotherapy (middle column of the treatment section in each panel a-f), and combination therapy (right column of the treatment section in each panel a-f) for high (middle row in each panel a-f) and low (bottom row in each panel a-f) doses. Examples of initial and final simulation snapshots are shown in each panel a-f with drug-sensitive (orange) and drug-resistant (purple) cells. Panels a-f also include plots of the dynamic mean fraction of drug-sensitive (orange) and drug-resistant (purple) cells, and standard deviations (dashed curves) from 100 simulation runs.

plot the fraction of drug-sensitive and drug-resistant cells over the simulation time course, 310 hours. Note that in Figure 6.8, we also plot examples of initial and final simulation snapshots during drug treatment to show the morphological changes in the cell configurations in response to different drug treatments and differently seeded spatial configurations of the cells on the lattice.

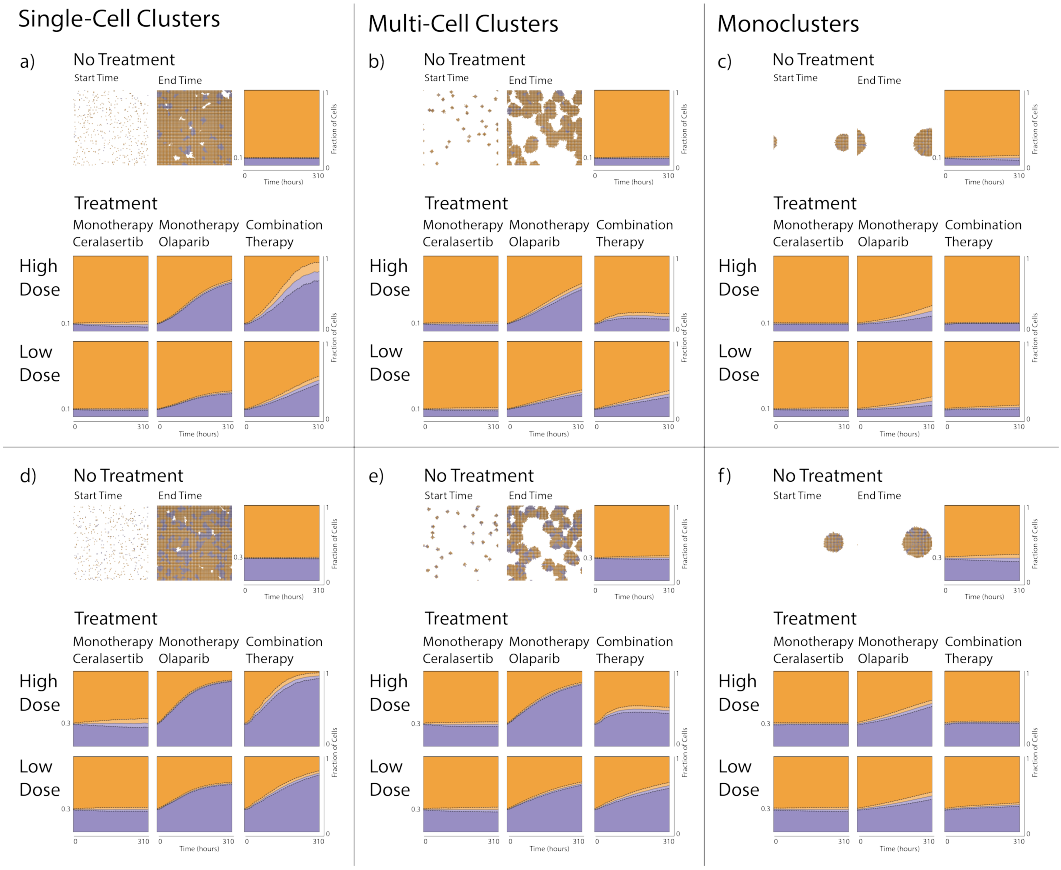

FIGURE 6.7: **Cells that are resistant to a PARPi (olaparib) compete for spatial resources with drug-sensitive cells.** P_0 cells are randomly seeded on the lattice in single-cell clusters (a,d), multi-cell clusters (b,e), or monoclusters (c,f), with either $0.1P_0$ (a,b,c) or $0.3P_0$ (d,e,f) drug-resistant cells. Simulations are performed with no drugs (top row in each panel a-f), ceralasertib monotherapy (left column of the treatment section in each panel a-f), olaparib monotherapy (middle column of the treatment section in each panel a-f), and combination therapy (right column of the treatment section in each panel a-f) for high (middle row in each panel a-f) and low (bottom row in each panel a-f) doses. Examples of initial and final simulation snapshots are shown in each panel a-f with drug-sensitive (orange) and drug-resistant (purple) cells. Panels a-f also include plots of the dynamic mean fraction of drug-sensitive (orange) and drug-resistant (purple) cells, and standard deviations (dashed curves) from 100 simulation runs.

We first note that by comparing the panels in Figure 6.8, as expected, higher drug concentrations result in fewer cells while maintaining the shape of the initial cell configuration. By comparing the panels in Figure 6.5, we can see how the different seeded cell populations lead to different population dynamics. From the results in Figure 6.5 (top rows of a-f), we see that, in the absence of drugs, the fractions of drug-sensitive and drug-resistant cells do not notably vary over the simulation

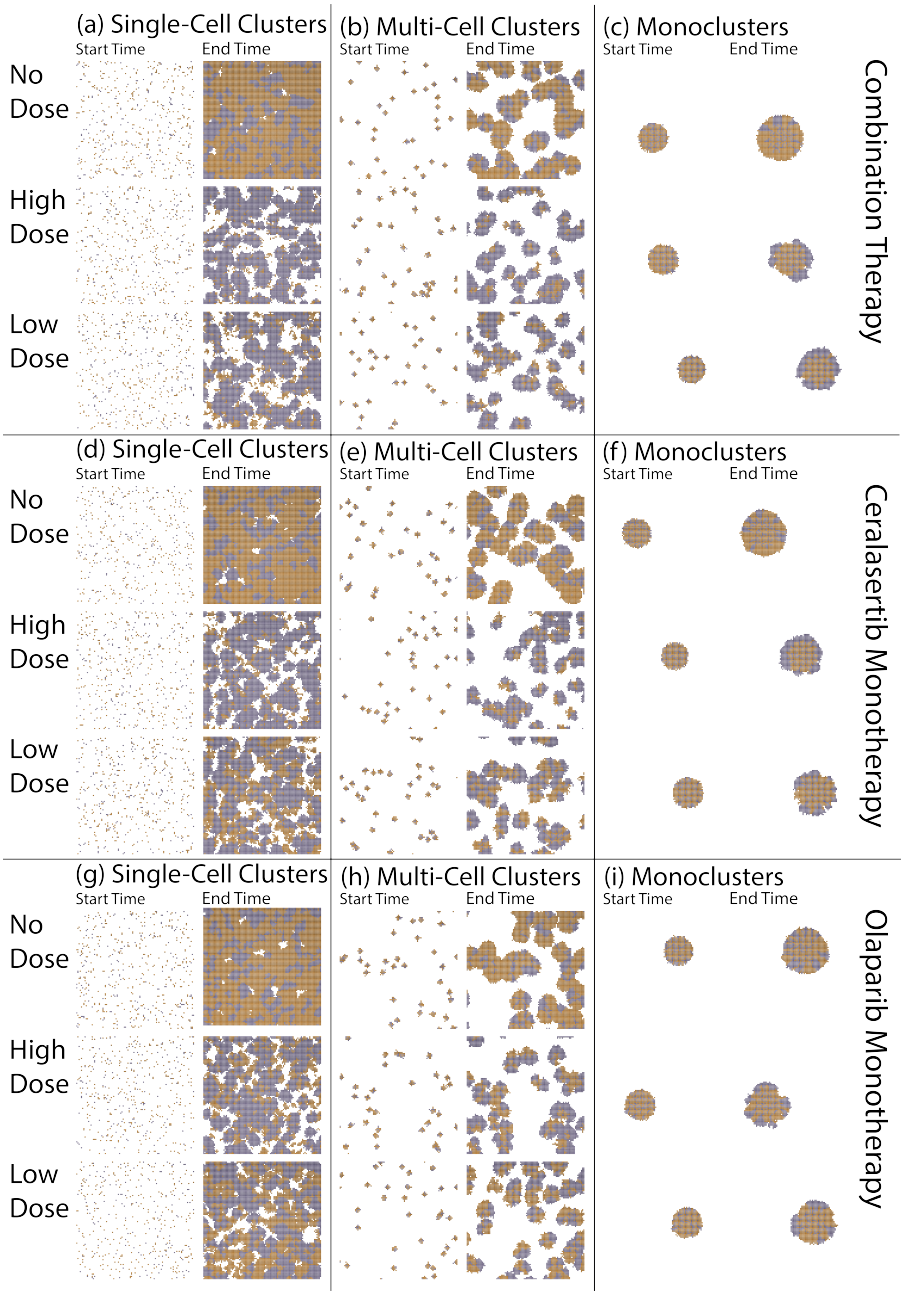

FIGURE 6.8: **The spatial organisation of cells with and without treatment.** In (a-i), we seed a total number of P_0 cells on the lattice, where $0.7P_0$ cells are drug-sensitive (orange) and $0.3P_0$ cells are drug-resistant (purple). Cells are seeded in single-cell clusters (a,d,g), multi-cell clusters (b,e,h), or monoclusters (c,f,i). Simulations are performed with no drugs (top row in each panel a-g), combination therapy (a,b,c), ceralasertib monotherapy (d,e,f), and olaparib monotherapy (g,h,i) for high (middle row in each panel a-i) and low (bottom row in each panel a-i) doses. Examples of initial and final simulation snapshots are shown in each panel.

time course for any seeded cell configuration. This is because there are no drugs to target the drug-sensitive or drug-resistant cells, which means both populations grow at the same rate. However, when drugs are applied in the in silico experiments, the fraction of the drug-resistant populations increase over time due to the drugs targeting the drug-sensitive populations only. This result is particularly significant when the cells are seeded in smaller-sized clusters. For instance, when cells are seeded in single-cell clusters and given high-dose combination treatments, the fraction of drug-resistant cells increases to the extent of dominating the population by the end of the simulations (Figure 6.5 (a) and (d)). The result that the initial cell configurations impact the dynamic composition of drug-sensitive to drug-resistant cells can be explained by the fact that cells can only proliferate if they have space to do so, i.e., are on the periphery of clusters. As such, cell crowding impedes the growth of both cell populations, whereas drugs impede the growth of drug-sensitive cell populations only. By decreasing the seeded cell cluster sizes, the space for undamaged and dividing cells to proliferate increases. This effect is exasperated when: (i) the initial fraction of drug-resistant cells is high at the start of the simulation, as can be observed by comparing panels (a,b,c) to (d,e,f) in Figure 6.5, (ii) drugs are given at high doses, as can be observed by comparing the middle to bottom rows in panels a-f in Figure 6.5, and (iii) drugs are administered in combination, as can be observed by comparing the columns in panels a-f in Figure 6.5.

In Figures 6.6 and 6.7, we have repeated the in silico experiments that are summarised in Figure 6.5, for cases where the drug-resistant cells are resistant only to either ceralasertib or olaparib. Interestingly, when cells are resistant to only one drug and are seeded in multi-cell clusters or monoclusters, low-dose combination treatments lead to higher fractions of drug-resistant cells compared to high-dose combination treatments (Figures 6.6 and 6.7 (b), (c), (e), and (f)). This is because even though one of the drugs suppresses both populations, the other drug suppresses the drug-sensitive population only. This means that low-dose combination treatments

lead to a fewer number of drug-resistant cells transitioning to the NC state compared to high-dose combination treatments. Therefore, a lower combination drug dose marginally favours the drug-resistant populations in Figures 6.6 and 6.7 (b), (c), (e), and (f).

In summary, our simulation results demonstrate that there is a complex interplay between in silico cell competition and seeded cell configurations, initial fraction of seeded drug-resistant cells, mode of drug resistance, drug treatments, and drug doses (Items 1-5, 6.1).

6.3.2 Spatial Competition and Drug Concentrations Impacts the Proliferation of Cancer Cell Subpopulations

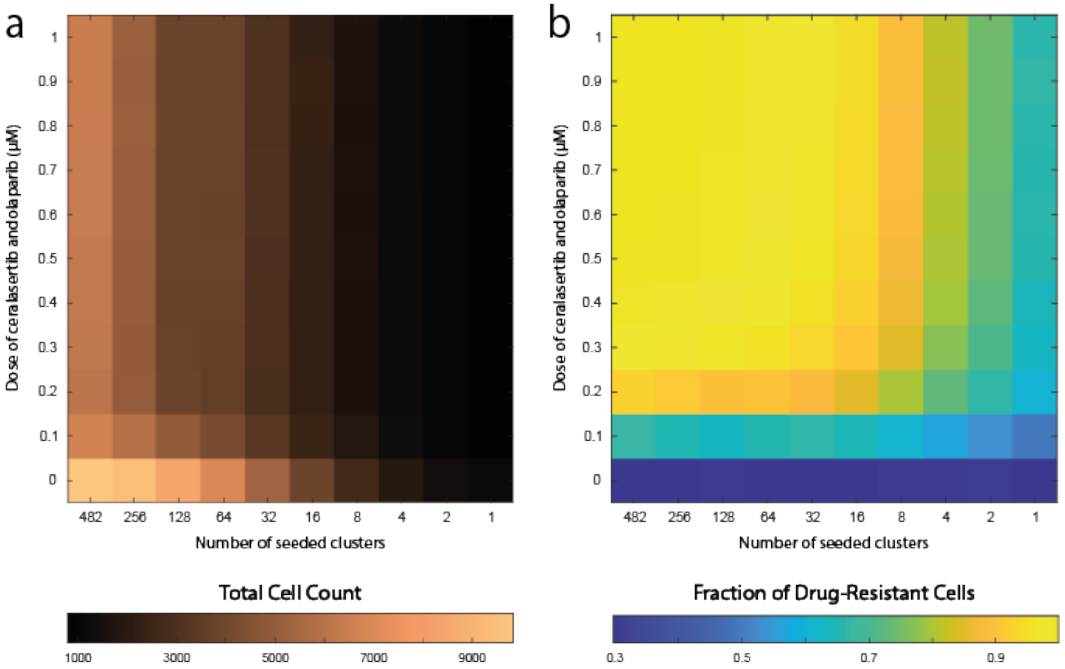

FIGURE 6.9: **Drug doses and spatial cell configurations impact the dynamics of total cell counts and the composition between drug-sensitive and drug-resistant cells.** The heatmaps show results from in silico experiments in which drug-sensitive and drug-resistant cells coexist. At the start of the experiments, P_0 cells are seeded on the lattice, where $0.3P_0$ cells are resistant to both ceralasertib and olaparib. Two inputs are varied in the simulations: (1) the number of clusters in which cells are seeded (indicated by the horizontal heatmap axes), and (2) the combination treatment drug doses (indicated by the vertical heatmap axes). The results show (a) the total cell count and (b) the fraction of drug-resistant cells at the end of the simulations. Each heatmap bin shows the mean value of 100 simulation runs.

To study how the spatial competition between cells impact not only drug-sensitive and drug-resistant subpopulation sizes, but also total cell counts, we here expand on the experiments described in Section 6.3.1. To do this, we vary two in silico inputs: the initial spatial cell configurations (Item 1, 6.1) and drug doses (Item 5, 6.1). In the experiments, we seed P_0 cells on the lattice in different number of clusters, where $0.3P_0$ cells are resistant to both ceralasertib and olaparib. Importantly, the number of seeded cells is the same for all in silico experiments, but the number of clusters in which the cells are seeded ranges between single-cell clusters to monoclusters. We also vary the combination drug dose between 0 and 1 μM, i.e., between [$\text{drug}_{\text{Cera}}$]=[$\text{drug}_{\text{Ola}}$]=0 μM and [$\text{drug}_{\text{Cera}}$]=[$\text{drug}_{\text{Ola}}$]=1 μM. Simulation results are summarised in heatmaps in Figure 6.9, where the first heatmap (a) shows the total cell count, and the second heatmap (b) shows the fraction of drug-resistant cells at the end of the simulation for different drug doses (vertical axes) and number of seeded clusters (horizontal axes). Note that in Figure 6.9, we plot the mean from 100 simulation runs. However, in Appendix A.4.4, we also plot the median, standard deviation, and variance from these 100 simulation runs.

Our simulation results show that the end time cell counts increase with the number of clusters and decrease with increasing drug doses (Figure 6.9 (a)). Drug-resistant population fractions also increase with the number of clusters but increase with increasing drug doses (Figure 6.9 (b)). From an in silico treatment perspective, this means that the treatment objective should influence the applied drug doses. Indeed, biologically relevant treatment objectives include: (i) suppressing the total cell count and (ii) suppressing the drug-resistant fraction, which might be best achieved by different doses. We exemplify this argument by considering a scenario in which the initial cell configuration (i.e., the number of seeded clusters) is fixed, but the applied drug dose is human-controllable. In this example, we start with 64 clusters and our treatment objective is to keep the end time cell count below 5000 cells. We can use Figure 6.9 (a) to see that the drug dose needs to be in the range 0.1-1 μM. From Figure 6.9 (b), we also see that dose 1 μM yields an end time drug-resistant

fraction of 0.99, whereas dose 0.1 μM yields an end time drug-resistant fraction of 0.66. Hence, one could argue that the latter drug dose is more favourable than the former drug dose from a treatment perspective.

Overall, our results suggest that different treatment objectives (e.g., suppressing cell counts, or suppressing drug-resistant cell populations) should be leveraged when designing treatment strategies (here, drug doses) since the objectives might be best achieved with different strategies.

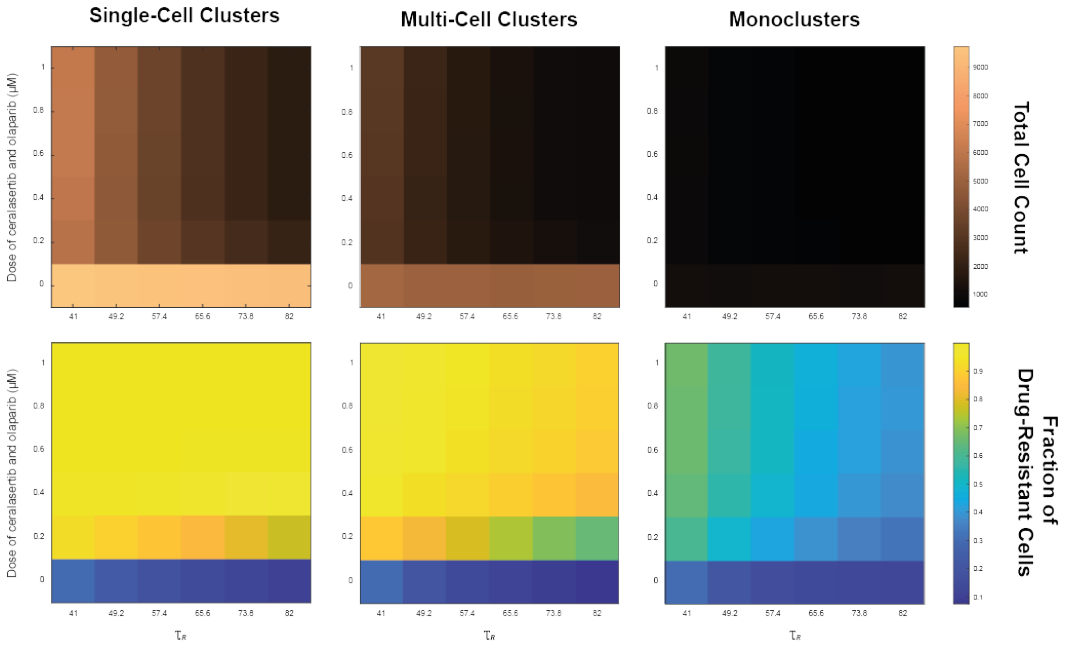

FIGURE 6.10: **Spatial cell configurations, drug doses, and cell doubling times impact the dynamics of total cell counts and the composition between drug-sensitive and drug-resistant cells.** At the start of the experiments, P_0 cells are seeded on the lattice, where $0.3P_0$ cells are resistant to both ceralasertib and olaparib. Three inputs are varied in the simulations: (1) the seeded cluster configurations (left, middle, right panel), (2) the combination treatment drug doses (indicated by the vertical heatmap axes), and (3) the mean doubling time of the drug-resistant cells (indicated by the horizontal heatmap axes). The heatmaps show the total cell count (top panel) and the fraction of drug-resistant cells (bottom panel) at the end of the simulation. Each heatmap bin shows the mean value of 100 simulation runs.

6.3.3 The Doubling Time of Drug-Resistant Cells Impacts Cell Population Dynamics

In the previous in silico experiments (Sections 6.3.1 and 6.3.2), the doubling times of drug-sensitive and drug-resistant cells are picked from the same normal distribution with mean doubling time, τ, and standard deviation σ. Now we investigate how population dynamics are affected when the mean doubling time τ_R of the drug-resistant cells are increased. As done in previous experiments, we seed P_0 cells on the lattice in single-cell clusters, multi-cell clusters, or monoclusters (Item 1, 6.1) where $0.3P_0$ cells are resistant to both ceralasertib and olaparib. We also, simultaneously, vary the ceralasertib and 2 doses (Item 5, 6.1; Figure 6.10 vertical axes), and the mean doubling time of drug-resistant cells (Item 6, 6.1; Figure 6.10 horizontal axes). The results are summarised in heatmaps in Figure 6.10, where we measure both the total cell count (top panel) and the fraction of drug-resistant cells (bottom panel) at the end of the simulations for different drug doses and drug-resistant doubling times for each seeded cell configurations.

As expected, our simulation results show that both cell counts and drug-resistant cell fractions decrease with increasing values of τ_R, due to fewer cell-divisions of drug-resistant cells. What is interesting to note, however, is that cell populations that are seeded in monoclusters are less sensitive to changes in τ_R, compared to populations that are seeded in single-cell and multi-cell clusters (Figure 6.10). This can be observed by comparing the spread in cell counts in the top heatmaps in Figure 6.10, and can be explained by the spatial limitations that follow from increased cluster sizes. On the other hand, the relationship between: (1) cell configurations, (2) drug doses, and (3) doubling times is more complicated to delineate. For instance, for the no drug treatment, the end time drug-resistant fraction varied between 0.3003-0.1029, 0.3001-0.0775, 0.3034-0.1274 when τ_R is increased from 41 to 82 hours for single-cell, multi-cell, and monoclusters, respectively. However, for the 1 uM drug dose, these fractions respectively vary between 0.9990-0.9979, 0.9691-0.9014, and

0.6661-0.3950 (Figure 6.10, bottom rows).

Together, these results indicate that spatial factors may significantly impact simulated cell populations' sensitivities to cell-extrinsic factors (e.g., drug doses) and cell-intrinsic factors (e.g., doubling times).

6.4 Conclusion

The tumour microenvironment is a complex system comprising multiple cell types. Knowing the spatial structure and location of these different cell types may help to predict treatment responses [186, 141, 171]. In this study, our focus is primarily on two specific cell types: drug-sensitive and drug-resistant cells. Nonetheless, we acknowledge that these cell-cell interactions that impact treatment responses are not limited to the interaction between drug-resistant and drug-sensitive cells. Indeed, a correlation between the spatial location of T-cells and improved treatment outcomes has also been revealed in many different cancers [59, 167, 124]. Similarly, in vitro spatial data have shown that tumour cells in close proximity to cancer-associated fibroblasts survive longer under therapy leading to resistance and worse overall survival [123, 121, 31], supported by in vivo work [121]. Another instance of spatial significance is knowing the location of immune cells within the tumour microenvironment. Studies have shown that immune cells situated in the tumour stroma can have a role in promoting angiogenesis, which can cause tumour proliferation and invasion [58].

Our in silico study demonstrates the importance of knowing the spatial location and distribution of resistant cells within a cancer cell population for cancer treatment, which is currently an understudied problem. Gathering spatial data from in vitro and in vivo experiments can be difficult, impractical, and time-consuming. Hence, we propose that mathematical models, such as the one developed in this work, can be used to guide predictions of treatment response.

The cell crowding limited ABM developed in this Chapter could be used to study tumour recurrence and previously treated cancers, where drug-resistant cells are already present. The ABM could be used to study optimal drug doses as we have with both compartment models previously discussed in this thesis (Chapters 2 and 4). To further expand on this work, instead of using a clock to track cells progression through the cell cycle, we could explore the changes to the results if we track progression by using the ODEs developed in either Chapter 2 or Chapter 4 for each individual cell.

The model developed in this paper certainly does not capture everything within a cancer cell population. The ABM could be developed further to study other forms of resistance, such as acquired resistance and communicated resistance. Despite this, the mathematical model is used to substantiate the implications of space limitations and cell-cell competition within the population and emphasise the importance of knowing the spatial structure of the cells for cancer treatment.

Chapter 7

Conclusions and Future Directions

7.1 Conclusions

In this thesis, we used two different modelling approaches to study the growth of cancer cells in response to DDRi drugs. These approaches included two compartment models and an ABM. We studied the temporal dynamics of cancer cell populations via a compartment model, and used it to explore the impact of the complex drug interactions on cancer cell proliferation and new combination doses of the drugs to maximise cell kill. Our simulation results showed that certain drug effects impact cell proliferation more than others. This indicates that although drugs target multiple DDR pathways, not all modes of action are as prominent as others. We performed both local (robustness analysis) and global (Latin hypercube analysis) sensitivity analysis techniques to study how sensitive our model output is to changes in the parameter values. Our results showed that the model output is not sensitive to certain parameters.

Motivated by the results of the sensitivity analysis, we simplified the compartment model to study the synergy between ceralasertib and olaparib. To analyse these models further, we explored the most synergistic combination doses using multiple synergy reference models, including Bliss, Highest-single agent (HSA), Loewe, and Lowest-single dose (LSD). Our simulation results demonstrated that the doses

deemed synergistic differ depending on the choice of reference model. Hence, we investigated four criterion spaces: Loewe-Bliss, LSD-Bliss, Loewe- HSA, and LSD-HSA, and found the Pareto optimal drug combinations which are deemed optimal on all four criterion spaces.

We then mapped the simplified compartment model onto a 2-D on-lattice ABM to investigate the temporal and spatial dynamics of cancer cell populations. An uncertainty analysis technique, consistency analysis, was performed on the ABM to mitigate model uncertainty from the results. Experimental studies have shown that cells can become resistant to DDR inhibitor drugs. Hence, we used the ABM to study the interplay between drug-sensitive and drug-resistant cancer cells and their impact on treatment responses to DDR inhibitor drugs. Our simulation results suggested that treatment responses to cancer drugs are simultaneously affected by: (i) different seeded spatial configurations of the cells on the lattice, (ii) the initial fraction of drug-resistant cells, (iii) the drugs to which the cells are resistant to, (iv) drug treatments (i.e., monotherapies and combinations of the drugs), (v) drug doses, and (vi) the doubling time of drug-resistant cells in relation to the doubling time of drug-sensitive cells.

7.2 Future Directions

There are many ways in which we can expand on our work. Radiotherapy is a common anti-cancer treatment that is currently used for around 50% of all cancer patients [14]. Radiotherapy induces DNA damage which triggers the DDR [149]. If the DDR is inhibited, e.g., by DDR inhibitor drugs, the likelihood of DNA damage getting repaired is lower, which could lead to an increased amount of cell death. Therefore, DDR inhibitors and radiotherapy could be combined to enhance tumour cytotoxicity [149]. Many clinical trials that study the combination of radiotherapy with DDR inhibitor drugs, many of which are PARP inhibitors, are recruiting, active, or completed. For example, the combination of radiotherapy and olaparib have

been trialled in many types of cancer such as breast cancer [39, 89, 131], pancreatic cancer [90], lung cancer [30], and head and neck cancer [88]. Following Checkley *et al.* [34] and Hamis *et al.* [75], one could add radiotherapy into both our compartment models and our ABM to further study the combination of radiation and DDR inhibitors. We could study the combination of radiation, olaparib and ceralasertib. Specifically, it would be interesting to add radiotherapy to the ABM discussed in Chapter 6 since radiotherapy breaks up the tumour, which leads to morphological changes. Hence, treating tumours with a monocluster structure using radiotherapy could result in tumours with appearances closer to the appearance of single-cell or multi-cell clusters.

Other potential expansions might be to adapt the model to study in vivo experiments. By doing so, we can investigate optimal scheduling, sequencing, and dosage of the drugs which can inform clinicians on optimal treatment for clinical trials that involve ceralasertib and olaparib. Similarly, we may incorporate other complex dynamics that might play a role in treatment outcomes. Incorporation of drug and oxygen diffusion might be realistic for studying in vitro and in vivo experiments. We could also look into performing parameter identifiability on the compartment models to see whether the experimental data is able to be used to accurately determine model parameters and which predictions we could make from the mathematical models [150, 81, 117, 104]. A structural and practical identifiability analysis could have been conducted on both the compartment models before simulating new, untested drug doses and combinations.

In conclusion, the work presented in this thesis has been used to: (1) explore the interactions of ceralasertib and olaparib on the cell cycle, (2) investigate the combined effects of ceralasertib and olaparib on cell growth and find their potential optimal doses in combination, and (3) study the competition for space between drug-sensitive and drug-resistant cancer that are subjected to DDR inhibitor drugs. We have demonstrated how in vitro experiments could benefit from mathematical

models, to inform better starting doses of the drugs that can elicit more effective cancer cell cytotoxicity. Furthermore, spatio-temporal analysis using a multiscale model showed that the spatial distribution of cancer cells affects their proliferation, even with high doses of drug combinations.

Bibliography

[1] R. Aggarwal. *Ceralasertib (AZD6738) alone and in combination with olaparib or durvalumab in patients with solid tumors. Identifier NCT03682289*. 2019. URL: https://clinicaltrials.gov/study/NCT03682289?cond=ceralasertib%20and%20olaparib&rank=2#study-plan (visited on 06/11/2023).

[2] J. C. Alamilla-Presuel et al. "Factors and molecular mechanisms of radiation resistance in cancer cells". In: *Int J Radiat Biol* 98.8 (2022), pp. 1301–1315.

[3] T. Alarcón, H. M. Byrne, and P. K. Maini. "A mathematical model of the effects of hypoxia on the cell-cycle of normal and cancer cells". In: *J Theor Biol* 229.3 (Aug. 2004), pp. 395–411.

[4] K. Alden et al. "Spartan: A comprehensive tool for understanding uncertainty in simulations of biological systems". In: *PLoS Comput Biol* 9.2 (2013), e1002916.

[5] J. C. Alfonso et al. "Estimating dose painting effects in radiotherapy: A mathematical model". In: *PLoS One* 9.2 (2014), e89380.

[6] J. F. Alhmoud et al. "DNA damage/repair management in cancers". In: *Cancers (Basel)* 12.4 (Apr. 2020).

[7] E. Armingol et al. "Deciphering cell-cell interactions and communication from gene expression". In: *Nat Rev Genet* 22.2 (Feb. 2021), pp. 71–88.

[8] A. Ashworth. "A synthetic lethal therapeutic approach: Poly(ADP) ribose polymerase inhibitors for the treatment of cancers deficient in DNA double-strand break repair". In: *J Clin Oncol* 26.22 (2008), pp. 3785–3790.

[9] AstraZeneca. *A study of ceralasertib monotherapy and ceralasertib plus durvalumab in patients with melanoma and resistance to PD-(L)1 inhibition (MONETTE). Identifier NCT05061134*. 2022. URL: https://clinicaltrials.gov/study/NCT05061134?cond=NCT05061134&rank=1 (visited on 06/11/2023).

[10] AstraZeneca. *An open-label phase 1 study of ceralasertib in Japanese patients with advanced solid malignancies. Identifier NCT05469919*. 2022. URL: https://clinicaltrials.gov/study/NCT05469919?cond=NCT05469919&rank=1 (visited on 06/11/2023).

[11] K. Bacevic et al. "Spatial competition constrains resistance to targeted cancer therapy". In: *Nat Commun* 8.1 (Dec. 2017), p. 1995.

[12] G. Balmus et al. "ATM orchestrates the DNA-damage response to counter toxic non-homologous end-joining at broken replication forks". In: *Nat Commun* 10.1 (Jan. 2019), p. 87.

[13] K. J. Barnum and M. J. O'Connell. "Cell cycle regulation by checkpoints". In: *Methods Mol Biol* 1170 (2014), pp. 29–40.

[14] R. Baskar et al. "Cancer and radiation therapy: Current advances and future directions". In: *Int J Med Sci* 9.3 (2012), pp. 193–199.

[15] J. S. Baxter et al. "Resistance to DNA repair inhibitors in cancer". In: *Mol Oncol* 16.21 (Nov. 2022), pp. 3811–3827.

[16] R. Bayat Mokhtari et al. "Combination therapy in combating cancer". In: *Oncotarget* 8.23 (June 2017), pp. 38022–38043.

[17] S. Bekisz and L. Geris. "Cancer modeling: From mechanistic to data-driven approaches, and from fundamental insights to clinical applications". In: *Journal of Computational Science* 46 (Aug. 2020), p. 101198.

[18] J. Benada and L. Macurek. "Targeting the checkpoint to kill cancer cells". In: *Biomolecules* 5.3 (Aug. 2015), pp. 1912–1937.

[19] C. I. Bliss. "The toxicity of poisons applied jointly". In: *Annals of Applied Biology* 26.3 (1939), pp. 585–615.

[20] S. Bohen, M. O'Connor, and M. Morgan. "DNA damage response – An emerging target for groundbreaking cancer therapies". In: *European Oncology & Haematology* (May 2018).

[21] S. M. Brady-Kalnay. "Molecular mechanisms of cancer cell-cell interactions: Cell-cell adhesion-dependent signaling in the tumor microenvironment". In: *Cell Adh Migr* 6.4 (2012), pp. 344–345.

[22] J. S. Brown et al. "Targeting DNA repair in cancer: Beyond PARP inhibitors". In: *Cancer Discov* 7.1 (Jan. 2017), pp. 20–37.

[23] S. Brüningk et al. "Combining radiation with hyperthermia: A multiscale model informed by in vitro experiments". In: *J R Soc Interface* 15.138 (Jan. 2018).

[24] J. Bull and H. Byrne. "The hallmarks of mathematical oncology". In: *Proceedings of the IEEE* 110.5 (2022), pp. 523–540.

[25] H. Byrne et al. "Multiscale modelling of solid tumour growth". In: *Selected topics in cancer modeling: Genesis, evolution, immune competition, and therapy*. Boston: Birkhäuser Boston, 2008, pp. 1–25.

[26] M. Cahuzac et al. "Development of olaparib-resistance prostate cancer cell lines to identify mechanisms associated with acquired resistance". In: *Cancers (Basel)* 14.16 (Aug. 2022).

[27] *Cancer Research UK, Cancer statistics for the UK*. URL: \url{//https://www.cancerresearchuk.org/health-professional/cancer-statistics-for-the-uk#heading-Three} (visited on 06/11/2023).

[28] M. C. Caron et al. "Poly(ADP-ribose) polymerase-1 antagonizes DNA resection at double-strand breaks". In: *Nat Commun* 10.1 (July 2019), p. 2954.

[29] L. Carrassa and G. Damia. "DNA damage response inhibitors: Mechanisms and potential applications in cancer therapy". In: *Cancer Treat Rev* 60 (Nov. 2017), pp. 139–151.

[30] Memorial Sloan Kettering Cancer Center. *A Study of olaparib and low dose radiotherapy for small cell lung cancer. Identifier NCT03532880*. 2018. URL: https:

//classic.clinicaltrials.gov/ct2/show/NCT03532880?term=olaparib+radiation&cond=cancer&draw=2&rank=8 (visited on 06/11/2023).

[31] N. H. Chakiryan et al. "Geospatial cellular distribution of cancer-associated fibroblasts significantly impacts clinical outcomes in metastatic clear cell renal cell carcinoma". In: *Cancers (Basel)* 13.15 (July 2021).

[32] H. H. Y. Chang et al. "Non-homologous DNA end joining and alternative pathways to double-strand break repair". In: *Nat Rev Mol Cell Biol* 18.8 (Aug. 2017), pp. 495–506.

[33] M. P. Chapman and C. J. Tomlin. "Ordinary differential equations in cancer biology". In: *bioRxiv* (2016).

[34] S. Checkley et al. "Bridging the gap between in vitro and in vivo: Dose and schedule predictions for the ATR inhibitor AZD6738". In: *Sci Rep* 5 (Aug. 2015), p. 13545.

[35] A. Chen. "PARP inhibitors: Its role in treatment of cancer". In: *Chin J Cancer* 30.7 (2011), pp. 463–471.

[36] J. Cohen. "Statistical power analysis for the behavioral sciences (2nd ed.)" In: *Routledge* (1988).

[37] M. S. Cooke et al. "Oxidative DNA damage: Mechanisms, mutation, and disease". In: *FASEB J* 17.10 (July 2003), pp. 1195–1214.

[38] A. Csikász-Nagy. "Computational systems biology of the cell cycle". In: *Briefings in Bioinformatics* 10.4 (Mar. 2009), pp. 424–434.

[39] Institut Curie. *Olaparib & radiation therapy for patients triple negative breast cancer (TNBC) (RadioPARP). Identifier NCT03109080*. 2017. URL: https://classic.clinicaltrials.gov/ct2/show/NCT03109080?term=olaparib+radiation&cond=cancer&draw=2&rank=1 (visited on 06/11/2023).

[40] A. J. Davis and D. J. Chen. "DNA double strand break repair via non-homologous end-joining". In: *Transl Cancer Res* 2.3 (June 2013), pp. 130–143.

[41] R. De Bont and N. van Larebeke. "Endogenous DNA damage in humans: A review of quantitative data". In: *Mutagenesis* 19.3 (May 2004), pp. 169–185.

[42] T. S. Deisboeck et al. "Multiscale cancer modeling". In: *Annual Review of Biomedical Engineering* 13.Volume 13, 2011 (2011), pp. 127–155.

[43] A. Dela, B. Shtylla, and L. de Pillis. "Multi-method global sensitivity analysis of mathematical models". In: *J Theor Biol* 546 (Aug. 2022), p. 111159.

[44] F. Delacôte and B. S. Lopez. "Importance of the cell cycle phase for the choice of the appropriate DSB repair pathway, for genome stability maintenance: The trans-S double-strand break repair model". In: *Cell Cycle* 7.1 (Jan. 2008), pp. 33–38.

[45] R. P. Dickinson and R. J. Gelinas. "Sensitivity analysis of ordinary differential equation systems—A direct method". In: *Journal of Computational Physics* 21.2 (1976), pp. 123–143.

[46] L. B. Edelman, J. A. Eddy, and N. D. Price. "In silico models of cancer". In: *Wiley Interdiscip Rev Syst Biol Med* 2.4 (2010), pp. 438–459.

[47] R. Emond et al. "Cell facilitation promotes growth and survival under drug pressure in breast cancer". In: *Nat Commun* 14.1 (June 2023), p. 3851.

[48] T. B. Emran et al. "Multidrug resistance in cancer: Understanding molecular mechanisms, immunoprevention and therapeutic approaches". In: *Front Oncol* 12 (2022), p. 891652.

[49] H. Enderling et al. "Paradoxical dependencies of tumor dormancy and progression on basic cell kinetics". In: *Cancer Res* 69.22 (2009), 8814–8821.

[50] M. Ensminger and M. brich. "One end to rule them all: Non-homologous end-joining and homologous recombination at DNA double-strand breaks". In: *Br J Radiol* 93.1115 (Nov. 2020), p. 20191054.

[51] N. D. Evans, R. J. Dimelow, and J. T. W. Yates. "Modelling of tumour growth and cytotoxic effect of docetaxel in xenografts". In: *Computer Methods and Programs in Biomedicine* 114.3 (2014), e3–e13.

[52] *FDA approves olaparib for gBRCAm metastatic pancreatic adenocarcinoma*. Dec. 2019. URL: https://www.fda.gov/drugs/resources-information-

approved-drugs/fda-approves-olaparib-gbrcam-metastatic-pancreatic-adenocarcinoma (visited on 08/04/2024).

[53] *FDA approves olaparib for germline BRCA-mutated metastatic breast cancer*. Jan. 2018. URL: https://www.fda.gov/drugs/resources-information-approved-drugs/fda-approves-olaparib-germline-brca-mutated-metastatic-breast-cancer (visited on 08/04/2024).

[54] *FDA approves olaparib tablets for maintenance treatment in ovarian cancer*. Aug. 2017. URL: https://www.fda.gov/drugs/resources-information-approved-drugs/fda-approves-olaparib-tablets-maintenance-treatment-ovarian-cancer (visited on 08/04/2024).

[55] *FDA approves olaparib with abiraterone and prednisone (or prednisolone) for BRCA-mutated metastatic castration-resistant prostate cancer*. May 2023. URL: https://www.fda.gov/drugs/drug-approvals-and-databases/fda-approves-olaparib-abiraterone-and-prednisone-or-prednisolone-brca-mutated-metastatic-castration (visited on 08/04/2024).

[56] J. Foucquier and M. Guedj. "Analysis of drug combinations: Current methodological landscape". In: *Pharmacol Res Perspect* 3.3 (June 2015), e00149.

[57] R. Friedman. "Drug resistance in cancer: Molecular evolution and compensatory proliferation". In: *Oncotarget* 7.11 (Mar. 2016), pp. 11746–11755.

[58] T. Fu et al. "Spatial architecture of the immune microenvironment orchestrates tumor immunity and therapeutic response". In: *J Hematol Oncol* 14.1 (June 2021), p. 98.

[59] J. Galon and A. Lanzi. "Immunoscore and its introduction in clinical practice". In: *Q J Nucl Med Mol Imaging* 64.2 (June 2020), pp. 152–161.

[60] R. A. Gatenby et al. "Eradicating metastatic cancer and the eco-evolutionary dynamics of anthropocene extinctions". In: *Cancer Res* 80.3 (Feb. 2020), pp. 613–623.

[61] N. Geary. "Understanding synergy". In: *American Journal of Physiology-Endocrinology and Metabolism* 304.3 (2013). PMID: 23211518, E237–E253.

[62] J. L. Gevertz and I. Kareva. "Guiding model-driven combination dose selection using multi-objective synergy optimization". In: *CPT Pharmacometrics Syst Pharmacol* 12.11 (Nov. 2023), pp. 1698–1713.

[63] A. Ghaffarizadeh, S. H. Friedman, and P. Macklin. "BioFVM: An efficient, parallelized diffusive transport solver for 3-D biological simulations". In: *Bioinformatics* 32.8 (2016), pp. 1256–1258.

[64] A. Ghaffarizadeh et al. "PhysiCell: An open source physics-based cell simulator for 3-D multicellular systems". In: *PLoS Comput. Biol.* 14.2 (2018), e1005991.

[65] Y. Gilad et al. "Drug combination in cancer treatment-from cocktails to conjugated combinations". In: *Cancers (Basel)* 13.4 (Feb. 2021).

[66] S. Goutelle et al. "The Hill equation: A review of its capabilities in pharmacological modelling". In: *Fundamental & clinical pharmacology* 22.6 (2008), pp. 633–648.

[67] W. R. Greco, G. Bravo, and J. C. Parsons. "The search for synergy: A critical review from a response surface perspective". In: *Pharmacol Rev* 47.2 (June 1995), pp. 331–385.

[68] S. M. Gross et al. "Analysis and modeling of cancer drug responses using cell cycle phase-specific rate effects". In: *Nat Commun* 14.1 (June 2023), p. 3450.

[69] R. Hakem. "DNA-damage repair; the good, the bad, and the ugly". In: *EMBO J* 27.4 (Feb. 2008), pp. 589–605.

[70] S. S. Hamed and C. M. Roth. "Mathematical modeling to distinguish cell cycle arrest and cell killing in chemotherapeutic concentration response curves". In: *J Pharmacokinet Pharmacodyn* 38.3 (June 2011), pp. 385–403.

[71] S. Hamis and F. Macfarlane. "A single-cell mathematical model of SARS-CoV-2 induced pyroptosis and the effects of anti-inflammatory intervention". In: *AIMS Mathematics* 6.6 (2021), pp. 6050–6086.

[72] S. Hamis, P. Nithiarasu, and G. G. Powathil. "What does not kill a tumour may make it stronger: In silico insights into chemotherapeutic drug resistance". In: *J Theor Biol* 454 (Oct. 2018), pp. 253–267.

[73] S. Hamis, G. G. Powathil, and M. A. J. Chaplain. "Blackboard to bedside: A mathematical modeling bottom-up approach toward personalized cancer treatments". In: *JCO Clin Cancer Inform* 3 (Feb. 2019), pp. 1–11.

[74] S. Hamis, S. Stratiev, and G. Powathil. "Uncertainty and sensitivity analyses methods for agent-based mathematical models: An introductory review". In: *World Scientific* (2020).

[75] S. Hamis et al. "Combining hypoxia-activated prodrugs and radiotherapy in silico: Impact of treatment scheduling and the intra-tumoural oxygen landscape". In: *PLoS Comput Biol* 16.8 (Aug. 2020), e1008041.

[76] S. Hamis et al. "Targeting cellular DNA damage responses in cancer: An in vitro-calibrated agent-based model simulating monolayer and spheroid treatment responses to ATR-inhibiting drugs". In: *Bull Math Biol* 83.10 (Aug. 2021), p. 103.

[77] L. A. Harris et al. "Modeling heterogeneous tumor growth dynamics and cell-cell interactions at single-cell and cell-population resolution". In: *Curr Opin Syst Biol* 17 (Oct. 2019), pp. 24–34.

[78] T. Helleday. "The underlying mechanism for the PARP and BRCA synthetic lethality: Clearing up the misunderstandings". In: *Mol Oncol* 5.4 (Aug. 2011), pp. 387–393.

[79] T. Helleday et al. "DNA double-strand break repair: From mechanistic understanding to cancer treatment". In: *DNA Repair (Amst)* 6.7 (July 2007), pp. 923–935.

[80] A. V. Hill. "The combinations of haemoglobin with oxygen and with carbon monoxide. I". In: *Biochemical Journal* 7.5 (1913), p. 471.

[81] R. J. W. Hill et al. "Optimizing circadian drug infusion schedules towards personalized cancer chronotherapy". In: *PLoS Comput Biol* 16.1 (Jan. 2020), e1007218.

[82] N. Holford. "Pharmacodynamic principles and the time course of immediate drug effects". In: *Transl Clin Pharmacol* 25.4 (Dec. 2017), pp. 157–161.

[83] N. Hosoya and K. Miyagawa. "Targeting DNA damage response in cancer therapy". In: *Cancer Sci* 105.4 (Apr. 2014), pp. 370–388.

[84] M. A. Hossain, Y. Lin, and S. Yan. "Single-strand break end resection in genome integrity: Mechanism and regulation by APE2". In: *Int J Mol Sci* 19.8 (Aug. 2018).

[85] C. C. Huang et al. "Combined effects of cigarette smoking, DNA methyltransferase 3B genetic polymorphism, and DNA damage on lung cancer". In: *BMC Cancer* 21.1 (Sept. 2021), p. 1066.

[86] M. V. Hunter et al. "Spatially resolved transcriptomics reveals the architecture of the tumor-microenvironment interface". In: *Nat Commun* 12.1 (Nov. 2021), p. 6278.

[87] *Incucyte live-cell analysis applications*. URL: \url{//https://www.sartorius.com/en/applications/life-science-research/live-cell-assays} (visited on 08/04/2024).

[88] The Netherlands Cancer Institute. *Olaparib and radiotherapy in head and neck cancer. Identifier NCT02229656*. 2014. URL: https://classic.clinicaltrials.gov/ct2/show/NCT02229656?term=olaparib+radiation&cond=cancer&draw=2&rank=10 (visited on 06/11/2023).

[89] The Netherlands Cancer Institute. *Olaparib and radiotherapy in inoperable breast cancer. Identifier NCT02227082*. 2014. URL: https://classic.clinicaltrials.gov/ct2/show/NCT02227082?term=olaparib+radiation&cond=cancer&draw=2&rank=3 (visited on 06/11/2023).

[90] The Netherlands Cancer Institute. *Testing the safety of the anti-cancer drugs durvalumab and olaparib during radiation therapy for locally advanced unresectable*

pancreatic cancer. Identifier NCT05411094. 2022. URL: https://classic.clinicaltrials.gov/ct2/show/NCT05411094?term=olaparib+radiation&cond=cancer&draw=2&rank=4 (visited on 06/11/2023).

[91] E. D. Israels and L. G. Israels. "The cell cycle". In: *Oncologist* 5.6 (2000), pp. 510–513.

[92] K. Janeway. *Olaparib With ceralasertib in recurrent osteosarcoma. Identifier NCT04417062*. 2022. URL: https://clinicaltrials.gov/study/NCT04417062?cond=ceralasertib%20and%20olaparib&rank=1 (visited on 06/11/2023).

[93] M. Jasin and R. Rothstein. "Repair of strand breaks by homologous recombination". In: *Cold Spring Harb Perspect Biol* 5.11 (Nov. 2013), a012740.

[94] C. Jean-Quartier et al. "In silico cancer research towards 3R". In: *BMC Cancer* 18.1 (Apr. 2018), p. 408.

[95] P. Jelinic and D. A. Levine. "New insights into PARP inhibitors' effect on cell cycle and homology-directed DNA damage repair". In: *Mol Cancer Ther* 13.6 (June 2014), pp. 1645–1654.

[96] V. R. Joseph. "Optimal ratio for data splitting". In: *Statistical Analysis and Data Mining: The ASA Data Science Journal* 15.4 (2022), pp. 531–538.

[97] I. Kareva, D. J. Waxman, and G. Lakka Klement. "Metronomic chemotherapy: An attractive alternative to maximum tolerated dose therapy that can activate anti-tumor immunity and minimize therapeutic resistance". In: *Cancer Lett* 358.2 (Mar. 2015), pp. 100–106.

[98] E. Karimi et al. "Single-cell spatial immune landscapes of primary and metastatic brain tumours". In: *Nature* 614.7948 (Feb. 2023), pp. 555–563.

[99] A. Kaznatcheev et al. "Fibroblasts and alectinib switch the evolutionary games played by non-small cell lung cancer". In: *Nat Ecol Evol* 3.3 (Mar. 2019), pp. 450–456.

[100] H. Kempf et al. "In silico analysis of cell cycle synchronisation effects in radiotherapy of tumour spheroids". In: *PLoS Comput Biol* 9.11 (2013), e1003295.

[101] Y. Koizumi and S. Iwami. "Mathematical modeling of multi-drugs therapy: a challenge for determining the optimal combinations of antiviral drugs". In: *Theor Biol Med Model* 11 (Sept. 2014), p. 41.

[102] R. D. Kouyos et al. "The path of least resistance: Aggressive or moderate treatment?" In: *Proc Biol Sci* 281.1794 (Nov. 2014), p. 20140566.

[103] M. Krajewska et al. "ATR inhibition preferentially targets homologous recombination-deficient tumor cells". In: *Oncogene* 34.26 (June 2015), pp. 3474–3481.

[104] C. Kreutz et al. "Profile likelihood in systems biology". In: *FEBS J* 280.11 (June 2013), pp. 2564–2571.

[105] E. L. Kwak, J. W. Clark, and B. Chabner. "Targeted agents: The rules of combination". In: *Clin Cancer Res* 13.18 Pt 1 (Sept. 2007), pp. 5232–5237.

[106] S. Lederer, T. M. H. Dijkstra, and T. Heskes. "Additive dose response models: Explicit formulation and the Loewe additivity consistency condition". In: *Frontiers in Pharmacology* 9 (2018). ISSN: 1663-9812. DOI: 10.3389/fphar.2018.00031.

[107] D. K. Lee, J. In, and S. Lee. "Standard deviation and standard error of the mean". In: *Korean Journal of Anesthesiology* 68.3 (2015), p. 220.

[108] K. Levenberg. "A method for the solution of certain non-linear problems in least squares". In: *Quarterly of Applied Mathematics* 2 (1944), pp. 164–168.

[109] W. H. Li et al. "PARP-1: A critical regulator in radioprotection and radiotherapy-mechanisms, challenges, and therapeutic opportunities". In: *Front Pharmacol* 14 (2023), p. 1198948.

[110] X. L. Li et al. "Integrating multiscale modeling with drug effects for cancer treatment". In: *Cancer Inform* 14.Suppl 5 (2015), pp. 21–31.

[111] C. D. Lin and B. Tang. "Latin hypercubes and space-filling designs". In: (2022). arXiv: 2203.06334.

[112] K. G. Link et al. "A local and global sensitivity analysis of a mathematical model of coagulation and platelet deposition under flow". In: *PLoS One* 13.7 (2018), e0200917.

[113] R. L. Lloyd et al. "Combined PARP and ATR inhibition potentiates genome instability and cell death in ATM-deficient cancer cells". In: *Oncogene* 39.25 (June 2020), pp. 4869–4883.

[114] E. D. Lobo and J. P. Balthasar. "Pharmacodynamic modeling of chemotherapeutic effects: Application of a transit compartment model to characterize methotrexate effects in vitro". In: *AAPS PharmSci* 4.4 (2002), E42.

[115] S. Loewe. "The problem of synergism and antagonism of combined drugs". In: *Arzneimittelforschung* 3.6 (June 1953), pp. 285–290.

[116] J. Ma and A. Motsinger-Reif. "Current methods for quantifying drug synergism". In: *Proteom Bioinform* 1.2 (July 2019), pp. 43–48.

[117] T. Maiwald et al. "Driving the model to its limit: Profile likelihood based model reduction". In: *PLoS One* 11.9 (2016), e0162366.

[118] Z. Mao et al. "DNA repair by nonhomologous end joining and homologous recombination during cell cycle in human cells". In: *Cell Cycle* 7.18 (Sept. 2008), pp. 2902–2906.

[119] A. Mardinoglu and J. Nielsen. "Systems medicine and metabolic modelling". In: *J Intern Med* 271.2 (Feb. 2012), pp. 142–154.

[120] S. Martinez-Pacheco and L. O'Driscoll. "Pre-clinical in vitro models used in cancer research: Results of a worldwide survey". In: *Cancers (Basel)* 13.23 (Nov. 2021).

[121] A. Marusyk et al. "Spatial proximity to fibroblasts impacts molecular features and therapeutic sensitivity of breast cancer cells influencing clinical outcomes". In: *Cancer Res* 76.22 (Nov. 2016), pp. 6495–6506.

[122] M. A. Masud, J. Y. Kim, and E. Kim. "Effective dose window for containing tumor burden under tolerable level". In: *NPJ Syst Biol Appl* 9.1 (May 2023), p. 17.

[123] M. A. Masud et al. "The impact of the spatial heterogeneity of resistant cells and fibroblasts on treatment response". In: *PLoS Comput Biol* 18.3 (Mar. 2022), e1009919.

[124] Y. Masugi et al. "T cells refines their prognostic utility for pancreatic cancer survival". In: *Mod Pathol* 32.10 (Oct. 2019), pp. 1495–1507.

[125] K. M. McKinnon. "Flow cytometry: An overview". In: *Curr Protoc Immunol* 120 (Feb. 2018), pp. 1–5.

[126] X. Miao et al. "Pharmacodynamic modeling of cell cycle effects for gemcitabine and trabectedin combinations in pancreatic cancer cells". In: *Frontiers in Pharmacology* 7 (2016). ISSN: 1663-9812.

[127] X. Miao et al. "Pharmacodynamic modeling of combined chemotherapeutic effects predicts synergistic activity of gemcitabine and trabectedin in pancreatic cancer cells". In: *Cancer Chemother Pharmacol* 77.1 (Jan. 2016), pp. 181–193.

[128] A. Min et al. "AZD6738, a novel oral inhibitor of ATR, induces synthetic lethality with ATM deficiency in gastric cancer cells". In: *Mol Cancer Ther* 16.4 (Apr. 2017), pp. 566–577.

[129] J. Morales et al. "Review of poly (ADP-ribose) polymerase (PARP) mechanisms of action and rationale for targeting in cancer and other diseases". In: *Crit Rev Eukaryot Gene Expr* 24.1 (2014), pp. 15–28.

[130] J. Murai et al. "Trapping of PARP1 and PARP2 by clinical PARP inhibitors". In: *Cancer Res* 72.21 (Nov. 2012), pp. 5588–5599.

[131] National Cancer Institute (NCI). *Radiation therapy with or without olaparib in treating patients with inflammatory breast cancer. Identifier NCT03598257*. 2018. URL: https://classic.clinicaltrials.gov/ct2/show/NCT03598257?

term=olaparib+radiation&cond=cancer&draw=2&rank=7 (visited on 06/11/2023).

[132] A. A. Neath and J. E. Cavanaugh. "The Bayesian information criterion: Background, derivation, and applications". In: *Wiley Interdisciplinary Reviews: Computational Statistics* 4.2 (2012), pp. 199–203.

[133] B. Novák and J. J. Tyson. "Modelling the controls of the eukaryotic cell cycle". In: *Biochem Soc Trans* 31.Pt 6 (Dec. 2003), pp. 1526–1529.

[134] B. Novák et al. "Mathematical model of the fission yeast cell cycle with checkpoint controls at the G1/S, G2/M and metaphase/anaphase transitions". In: *Biophys Chem* 72.1-2 (May 1998), pp. 185–200.

[135] G. Noël et al. "Poly(ADP-ribose) polymerase (PARP-1) is not involved in DNA double-strand break recovery". In: *BMC Cell Biol* 16 (July 2003), p. 4.

[136] A. C. Obenauf et al. "Therapy-induced tumour secretomes promote resistance and tumour progression". In: *Nature* 520.7547 (Apr. 2015), pp. 368–372.

[137] M. J. O'Connor. "Targeting the DNA damage response in cancer". In: *Mol Cell* 60.4 (Nov. 2015), pp. 547–560.

[138] P. C. O'Leary et al. "Resistance to ATR inhibitors is mediated by loss of the nonsense-mediated decay factor UPF2". In: *Cancer Res* 82.21 (Nov. 2022), pp. 3950–3961.

[139] N. J. O'Neil, M. L. Bailey, and P. Hieter. "Synthetic lethality and cancer". In: *Nat Rev Genet* 18.10 (Oct. 2017), pp. 613–623.

[140] S. Oskay Halacli, B. Halacli, and K. Altundag. "The significance of heat shock proteins in breast cancer therapy". In: *Med Oncol* 30.2 (2013), p. 575.

[141] E. R. Parra. "Methods to determine and analyze the cellular spatial distribution extracted from multiplex immunofluorescence data to understand the tumor microenvironment". In: *Front Mol Biosci* 8 (2021), p. 668340.

[142] J. Picot et al. "Flow cytometry: Retrospective, fundamentals and recent instrumentation". In: *Cytotechnology* 64.2 (Mar. 2012), pp. 109–130.

[143] J. Poleszczuk, P. Macklin, and H. Enderling. "Agent-based modeling of cancer stem cell driven solid tumor growth". In: *Methods Mol Biol* 1516 (2016), pp. 335–346.

[144] S. Portet. "A primer on model selection using the Akaike Information Criterion". In: *Infectious Disease Modelling* 5 (2020), pp. 111–128.

[145] G. G. Powathil et al. "Modelling the effects of cell-cycle heterogeneity on the response of a solid tumour to chemotherapy: Biological insights from a hybrid multiscale cellular automaton model". In: *J Theor Biol* 308 (Sept. 2012), pp. 1–19.

[146] J. H. Proost, D. J. Eleveld, and M. M. R. F. Struys. "Population pharmacodynamic modeling using the Sigmoid Emax model: Influence of inter-individual variability on the steepness of the concentration–effect relationship. A simulation study". In: *The AAPS Journal* 23.1 (2020), p. 10.

[147] K. Pugh, M. Davies, and G. Powathil. "A mathematical model to investigate the effects of ceralasertib and olaparib in targeting the cellular DNA damage response pathway". In: *J Pharmacol Exp Ther* 387.1 (Oct. 2023), pp. 55–65.

[148] G. Qian and A. Mahdi. "Sensitivity analysis methods in the biomedical sciences". In: *Mathematical Biosciences* 323 (2020), p. 108306. ISSN: 0025-5564.

[149] Y. Qiu et al. "Triple kill: DDR inhibitors, radiotherapy and immunotherapy leave cancer cells with no escape". In: *Acta Biochim Biophys Sin (Shanghai)* 54.11 (Oct. 2022), pp. 1569–1576.

[150] K. Rateitschak et al. "Parameter identifiability and sensitivity analysis predict targets for enhancement of STAT1 activity in pancreatic cancer and stellate cells". In: *PLoS Comput Biol* 8.12 (2012), e1002815.

[151] A. Ray Chaudhuri and A. Nussenzweig. "The multifaceted roles of PARP1 in DNA repair and chromatin remodelling". In: *Nat Rev Mol Cell Biol* 18.10 (Oct. 2017), pp. 610–621.

[152] B. Ribba, T. Colin, and S. Schnell. "A multiscale mathematical model of cancer, and its use in analyzing irradiation therapies". In: *Theor Biol Med Model* 3 (Feb. 2006), p. 7.

[153] R. C. Rockne and J. G. Scott. "Introduction to mathematical oncology". In: *JCO Clin Cancer Inform* 3 (Apr. 2019), pp. 1–4.

[154] R. C. Rockne et al. "The 2019 mathematical oncology roadmap". In: *Physical Biology* 16.4 (June 2019), p. 041005.

[155] R. Roe-Dale, D. Isaacson, and M. Kupferschmid. "A mathematical model of cell cycle effects in gastric cancer chemotherapy". In: *Bull Math Biol* 74.1 (Jan. 2012), pp. 159–174.

[156] A. Romiti et al. "Metronomic chemotherapy for cancer treatment: A decade of clinical studies". In: *Cancer Chemother Pharmacol* 72.1 (July 2013), pp. 13–33.

[157] A. Ghelli Luserna di Rora', I. Iacobucci, and G. Martinelli. "The cell cycle checkpoint inhibitors in the treatment of leukemias". In: *J Hematol Oncol* 10.1 (Mar. 2017), p. 77.

[158] R. Salgia et al. "Modeling small cell lung cancer (SCLC) biology through deterministic and stochastic mathematical models". In: *Oncotarget* 9.40 (May 2018), pp. 26226–26242.

[159] A. Saltelli et al. "Sensitivity analysis: A discipline coming of age". In: *Environmental Modelling and Software* 146 (Oct. 2021), p. 105226.

[160] S. Saxena and L. Zou. "Hallmarks of DNA replication stress". In: *Mol Cell* 82.12 (June 2022), pp. 2298–2314.

[161] P. Schober, C. Boer, and L. A. Schwarte. "Correlation coefficients: Appropriate use and interpretation". In: *Anesth Analg* 126.5 (May 2018), pp. 1763–1768.

[162] N. Schultz et al. "Poly(ADP-ribose) polymerase (PARP-1) has a controlling role in homologous recombination". In: *Nucleic Acids Research* 31.17 (Sept. 2003), pp. 4959–4964.

[163] M. S. Siddiqui et al. "H2AX: A promising molecular marker of DNA damage and aging". In: *Mutat Res Rev Mutat Res* 766 (2015), pp. 1–19.

[164] M. Sorin et al. "Single-cell spatial landscapes of the lung tumour immune microenvironment". In: *Nature* 614.7948 (Feb. 2023), pp. 548–554.

[165] B. Q. Spring et al. "Illuminating the numbers: Integrating mathematical models to optimize photomedicine dosimetry and combination therapies". In: *Front Phys* 7 (Apr. 2019).

[166] G. R. Stark and W. R. Taylor. "Analyzing the G2/M checkpoint". In: *Methods Mol Biol* 280 (2004), pp. 51–82.

[167] A. V. Stein et al. "High intratumoural but not peritumoural inflammatory host response is associated with better prognosis in primary resected oesophageal adenocarcinomas". In: *Pathology* 49.1 (Jan. 2017), pp. 30–37.

[168] M. A. R. Strobl et al. "Spatial structure impacts adaptive therapy by shaping intra-tumoral competition". In: *Commun Med (Lond)* 2 (2022), p. 46.

[169] M. H. Swat et al. "Multi-scale modeling of tissues using CompuCell3D". In: *Methods Cell Biol* 110 (2012), pp. 325–366.

[170] A. Sysoev. "Sensitivity analysis of mathematical models". In: *Computation* 11.8 (2023).

[171] R. W. Tothill et al. "Novel molecular subtypes of serous and endometrioid ovarian cancer linked to clinical outcome". In: *Clin Cancer Res* 14.16 (Aug. 2008), pp. 5198–5208.

[172] A. Tsuboi et al. "Competition for space is controlled by apoptosis-induced change of local epithelial topology". In: *Curr Biol* 28.13 (July 2018), pp. 2115–2128.

[173] A. Tubbs and A. Nussenzweig. "Endogenous DNA damage as a source of genomic instability in cancer". In: *Cell* 168.4 (Feb. 2017), pp. 644–656.

[174] J. J. Tyson and B. Novák. "Regulation of the eukaryotic cell cycle: Molecular antagonism, hysteresis, and irreversible transitions". In: *J Theor Biol* 210.2 (May 2001), pp. 249–263.

[175] Z. Ugray et al. “Scatter search and local NLP solvers: A multistart framework for global optimization”. In: *INFORMS Journal on Computing* 19.3 (2007), pp. 328–340.

[176] A. Vallés-Martí et al. “Phosphoproteomics guides effective low-dose drug combinations against pancreatic ductal adenocarcinoma”. In: *Cell Rep* 42.6 (June 2023), p. 112581.

[177] A. Vargha and H.D. Delaney. “A critique and improvement of the "CL" common language effect size statistics of McGraw and Wong”. In: *Journal of Educational and Behavioral Statistics* 25.2 (2000), pp. 101–132. ISSN: 10769986, 19351054. (Visited on 12/07/2023).

[178] F. P. Vendetti et al. “The orally active and bioavailable ATR kinase inhibitor AZD6738 potentiates the anti-tumor effects of cisplatin to resolve ATM-deficient non-small cell lung cancer in vivo”. In: *Oncotarget* 6.42 (Dec. 2015), pp. 44289–44305.

[179] A. H. C. Vlot et al. “Applying synergy metrics to combination screening data: Agreements, disagreements and pitfalls”. In: *Drug Discov Today* 24.12 (Dec. 2019), pp. 2286–2298.

[180] J. Wang. *A study to evaluate the safety and pharmacokinetics of ceralasertib in combination with durvalumab in Chinese patients with advanced solid tumours. Identifier NCT05514132*. 2022. URL: https://clinicaltrials.gov/study/NCT05514132?cond=NCT05514132&rank=1 (visited on 06/11/2023).

[181] X. Wang, H. Zhang, and X. Chen. “Drug resistance and combating drug resistance in cancer”. In: *Cancer Drug Resist* 2.2 (2019), pp. 141–160.

[182] Z. Wang and T. S. Deisboeck. “Mathematical modeling in cancer drug discovery”. In: *Drug Discovery Today* 19.2 (2014). System Biology, pp. 145–150.

[183] Z. Wang et al. “Simulating cancer growth with multiscale agent-based modeling”. In: *Semin Cancer Biol* 30 (Feb. 2015), pp. 70–78.

[184] *World health organization - cancer*. URL: \url{//https://www.who.int/news-room/fact-sheets/detail/cancer} (visited on 06/11/2023).

[185] B. Yadav et al. “Searching for drug synergy in complex dose-response landscapes using an interaction potency model”. In: *Comput Struct Biotechnol J* 13 (2015), pp. 504–513.

[186] Y. Yuan. “Spatial heterogeneity in the tumor microenvironment”. In: *Cold Spring Harb Perspect Med* 6.8 (Aug. 2016).

[187] H. Zhang, D. G. Delafield, and L. Li. “Mass spectrometry imaging: The rise of spatially resolved single-cell omics”. In: *Nat Methods* 20.3 (Mar. 2023), pp. 327–330.

[188] H. Zhang et al. “Mapping combinatorial drug effects to DNA damage response kinase inhibitors”. In: *Nat Commun* 14.1 (Dec. 2023), p. 8310.

[189] J. Zhang et al. “Integrating evolutionary dynamics into treatment of metastatic castrate-resistant prostate cancer”. In: *Nat Commun* 8.1 (Nov. 2017), p. 1816.

[190] X. Zhu, R. M. Straubinger, and W. J. Jusko. “Mechanism-based mathematical modeling of combined gemcitabine and birinapant in pancreatic cancer cells”. In: *J Pharmacokinet Pharmacodyn* 42.5 (Oct. 2015), pp. 477–496.

Appendix A

Appendix to Chapters

A.1 Appendix to Chapter 2

A.1.1 Transit Compartments to Represent Drug-Induced Death Delay

Cell death does not necessarily occur immediately after the drug is given. Sometimes it can occur within one to two cell divisions after the drug is given. In Chapter 2, we incorporate the delay observed in the drug-induced cell death with a transit compartment into the model to represent death delay [126, 114, 127]. This represents the ceralasertib-specific cell death from state G2D.

Adding in more transit compartments will not increase the total number of parameters, as the time spent in each transit compartment will be equal to θ [126]. We can update equations 2.7 to include more than one transit compartment accordingly:

$$\frac{d[G1](t)}{dt} = 2k_5\left(1-\frac{N(t)}{C_{HC}}\right)[G2](t) - k_1[G1](t), \tag{A.1a}$$

$$\begin{aligned}\frac{d[S](t)}{dt} =& k_1(1-p(1+\text{Effect}_{\text{Ola},1}))[G1](t) - k_2[S](t)\\ &+ k_3(1-\text{Effect}_{\text{Cera},1})[SD](t),\end{aligned} \tag{A.1b}$$

$$\begin{aligned}\frac{d[G2](t)}{dt} =& k_2(1-q)[S](t) - k_5\left(1-\frac{N(t)}{C_{HC}}\right)[G2](t)\\ &+ k_7(1-\text{Effect}_{\text{Ola},2})[G2D](t),\end{aligned} \tag{A.1c}$$

$$\begin{aligned}\frac{d[SD](t)}{dt} =& k_1 p(1+\text{Effect}_{\text{Ola},1})[G1](t) - k_3(1-\text{Effect}_{\text{Cera},1})[SD](t) \\ & - k_6[SD](t) - k_4[SD](t),\end{aligned} \tag{A.1d}$$

$$\begin{aligned}\frac{d[G2D](t)}{dt} =& k_2 q[S](t) + k_6[SD](t) - k_7(1-\text{Effect}_{\text{Ola},2})[G2D](t) \\ & - k_8[G2D](t) - [A_m](t)[G2D](t),\end{aligned} \tag{A.1e}$$

$$\frac{d[D](t)}{dt} = k_4[SD](t) + k_8[G2D](t) + [A_m](t)[G2D](t), \tag{A.1f}$$

$$\frac{d[A_1](t)}{dt} = \frac{1}{\theta}(\text{Effect}_{\text{Cera},2} - [A_1](t)), \tag{A.1g}$$

$$\frac{d[A_j](t)}{dt} = \frac{1}{\theta}([A_{j-1}](t) - [A_j](t)), \tag{A.1h}$$

where m is the number of transit compartments and $j = 2, 3, \ldots, m$. Note that we define the initial conditions of the transit compartments as $A_1(0) = A_j(0) = 0$.

Simulation results are summarised in Figure A.1, where we study the parameterisation and evaluation of the model with (a) one, (b) two, and (c) three transit compartments. Note that the total RMSE (equation 2.12) is equal to 12.2405, 12.9740, and 13.6575 when we include one, two, and three compartments into Model HC respectively. Hence, we argue that one transit compartment suffices to model cell population dynamics in response to 0.1-0.3 μM ceralasertib doses and 0.03-0.3 μM olaparib doses.

A.2 Appendix to Chapter 3

A.2.1 Latin Hypercube Analysis

We perform Latin hypercube analysis on the compartment model discussed in Chapter 2, Model HC, to study how global changes to the model parameters influence the uncertainty in the model output. Here, the model output is the RMSE of the cell confluency for each drug treatment separately. In the main part of the thesis, we include the values of the Pearson Product Moment Correlations for each parameter and drug treatment. Figures A.2-A.10 display scatter-plots where

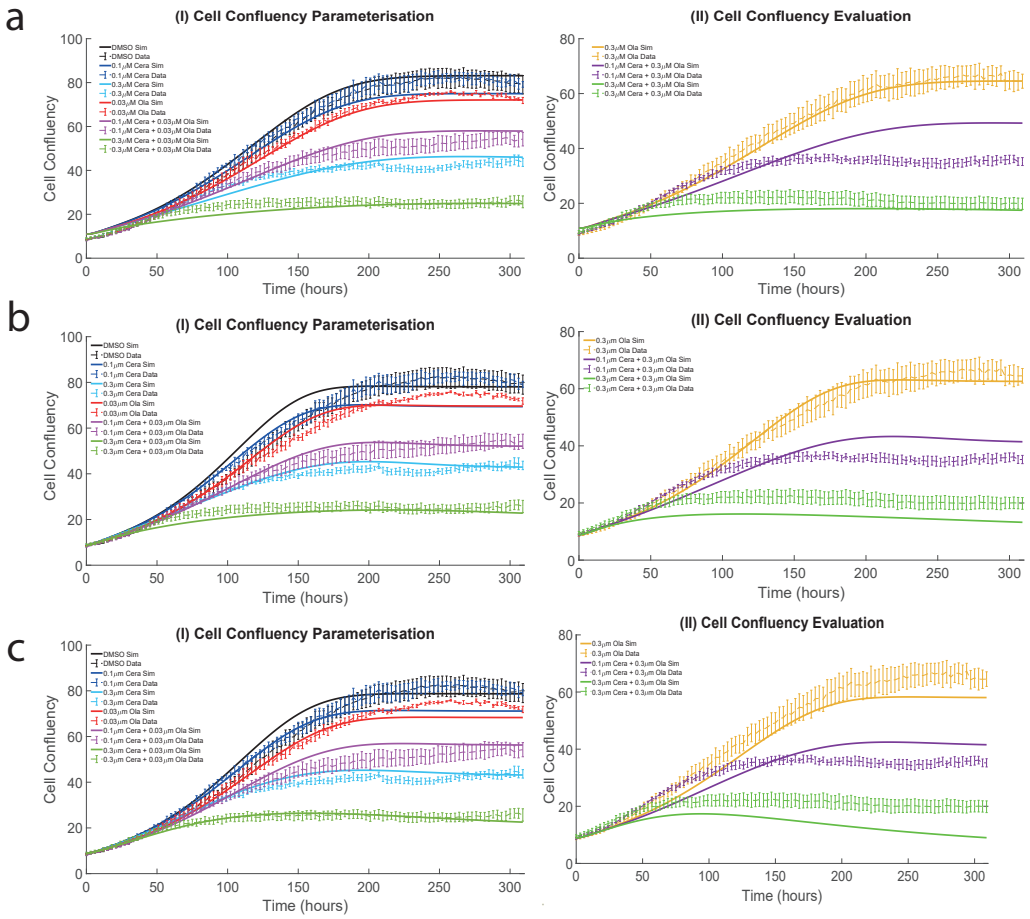

FIGURE A.1: **Cell death occurs at a delayed rate in Model HC (Chapter 2).** The plots show simulated and experimental cell confluency over 310 hours for various dose combinations of ceralasertib and olaparib with (a) one, (b) two, and (c) three transit compartments to represent death delay. Cells spend θ amount of time in each transit compartment. Training data is used to parameterise (plot I) and test data is used to evaluate the model (plot II) against experimental data 1. The solid curves represent the simulation results from the compartment model. The dashed curves represent the mean in vitro data, with standard errors for 3 experiments indicated with error bars.

we can visually see the correlations between the model parameters and the model output.

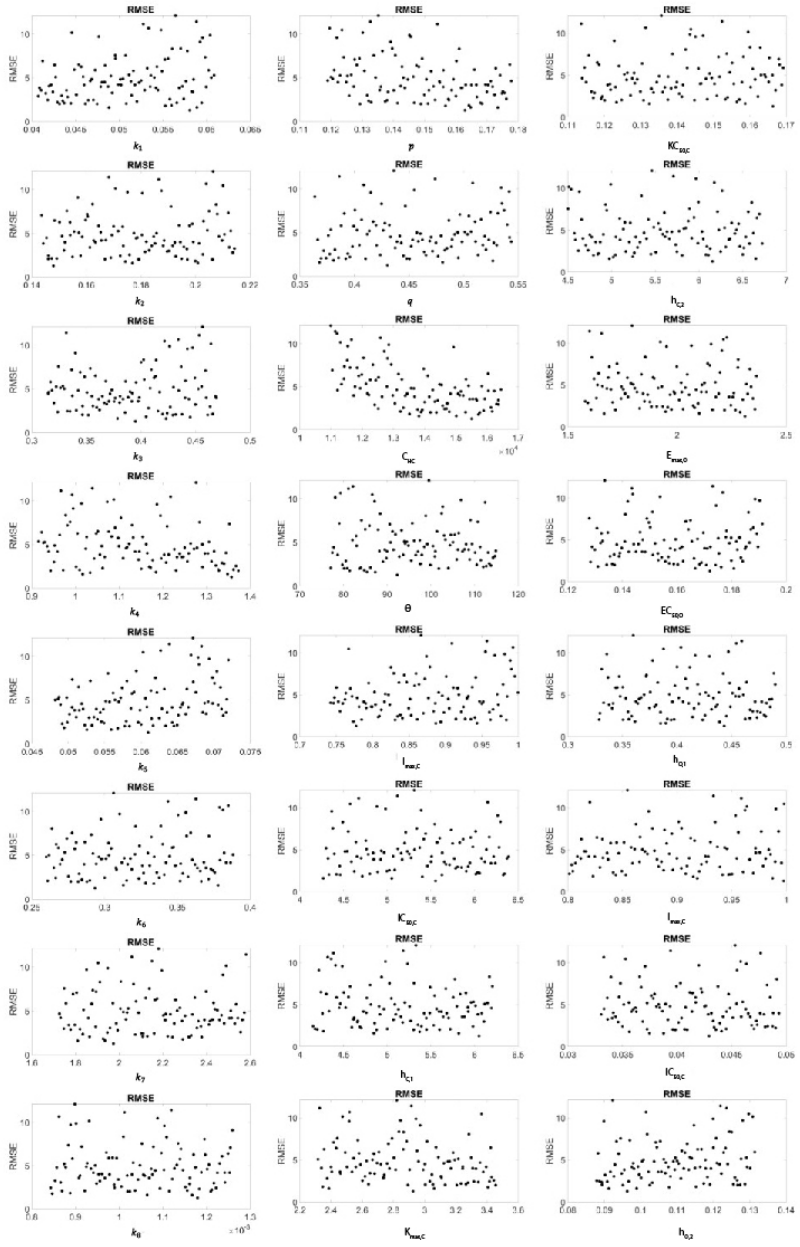

FIGURE A.2: **Latin hypercube analysis is a method to see how sensitive the model output is to global changes in parameter values.** The figure displays scatter-plots relating to the linear correlations between each parameter in its investigated range (horizontal axes) and the model output (vertical axes). Here, the model output is the RMSE of the cell confluency throughout the time-course of the simulation (equation 2.10) in response to no drug treatment.

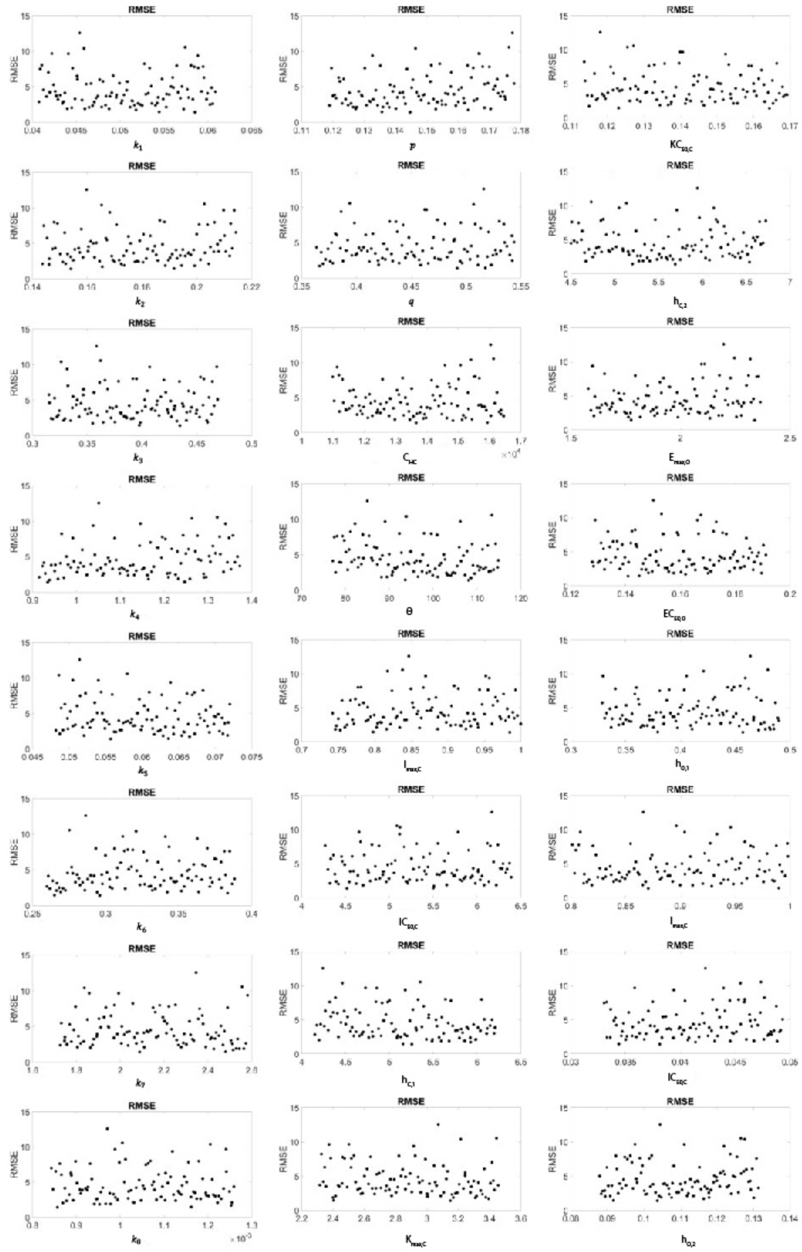

FIGURE A.3: **Latin hypercube analysis is a method to see how sensitive the model output is to global changes in parameter values.** The figure displays scatter-plots relating to the linear correlations between each parameter in its investigated range (horizontal axes) and the model output (vertical axes). Here, the model output is the RMSE of the cell confluency throughout the time-course of the simulation (equation 2.10) in response to 0.03 μM olaparib.

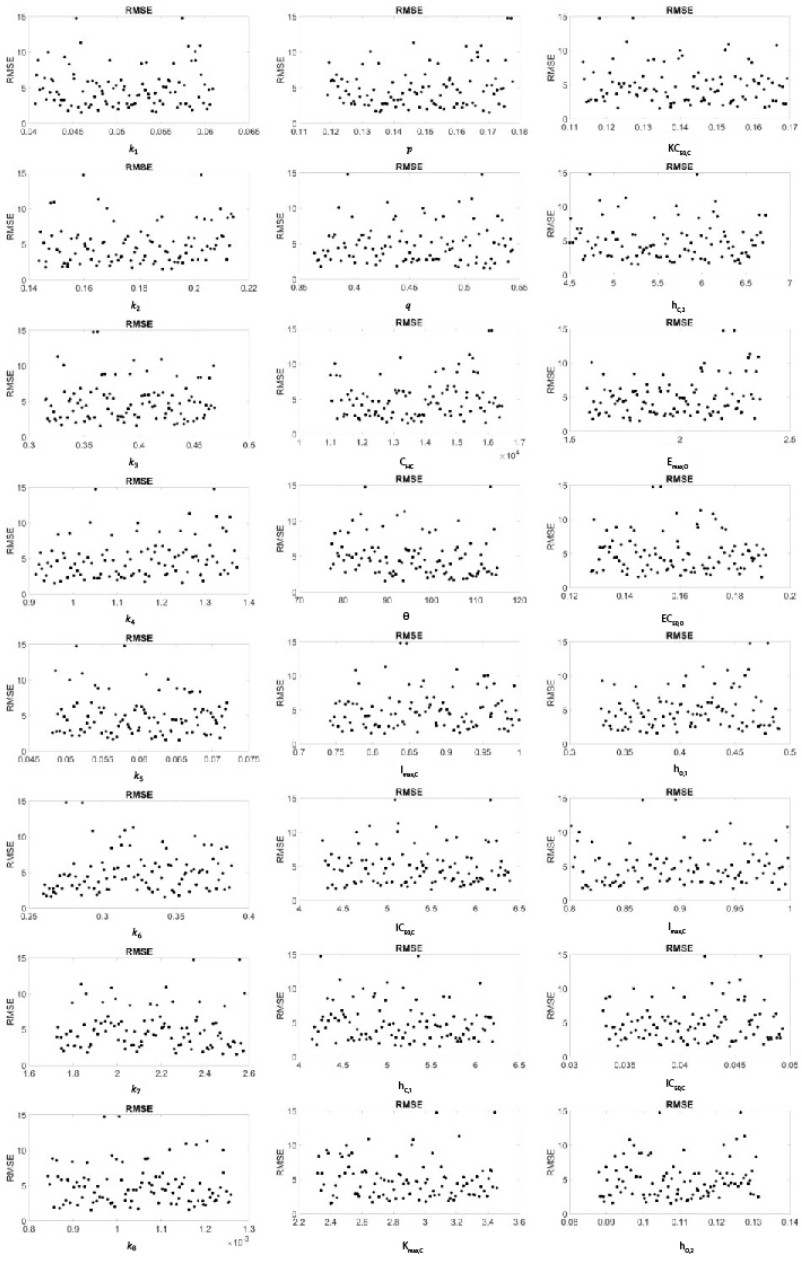

FIGURE A.4: **Latin hypercube analysis is a method to see how sensitive the model output is to global changes in parameter values.** The figure displays scatter-plots relating to the linear correlations between each parameter in its investigated range (horizontal axes) and the model output (vertical axes). Here, the model output is the RMSE of the cell confluency throughout the time-course of the simulation (equation 2.10) in response to 0.3 μM olaparib.

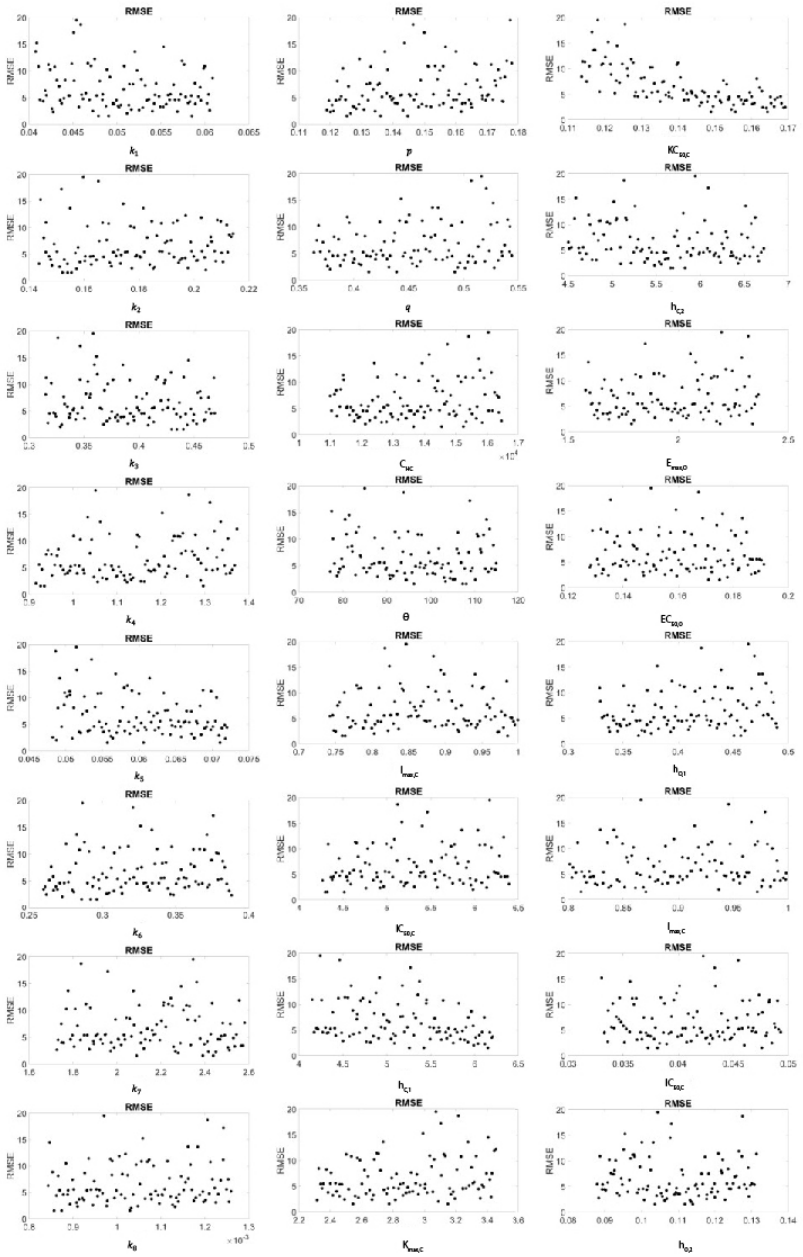

FIGURE A.5: **Latin hypercube analysis is a method to see how sensitive the model output is to global changes in parameter values.** The figure displays scatter-plots relating to the linear correlations between each parameter in its investigated range (horizontal axes) and the model output (vertical axes). Here, the model output is the RMSE of the cell confluency throughout the time-course of the simulation (equation 2.10) in response to 0.1 μM ceralasertib.

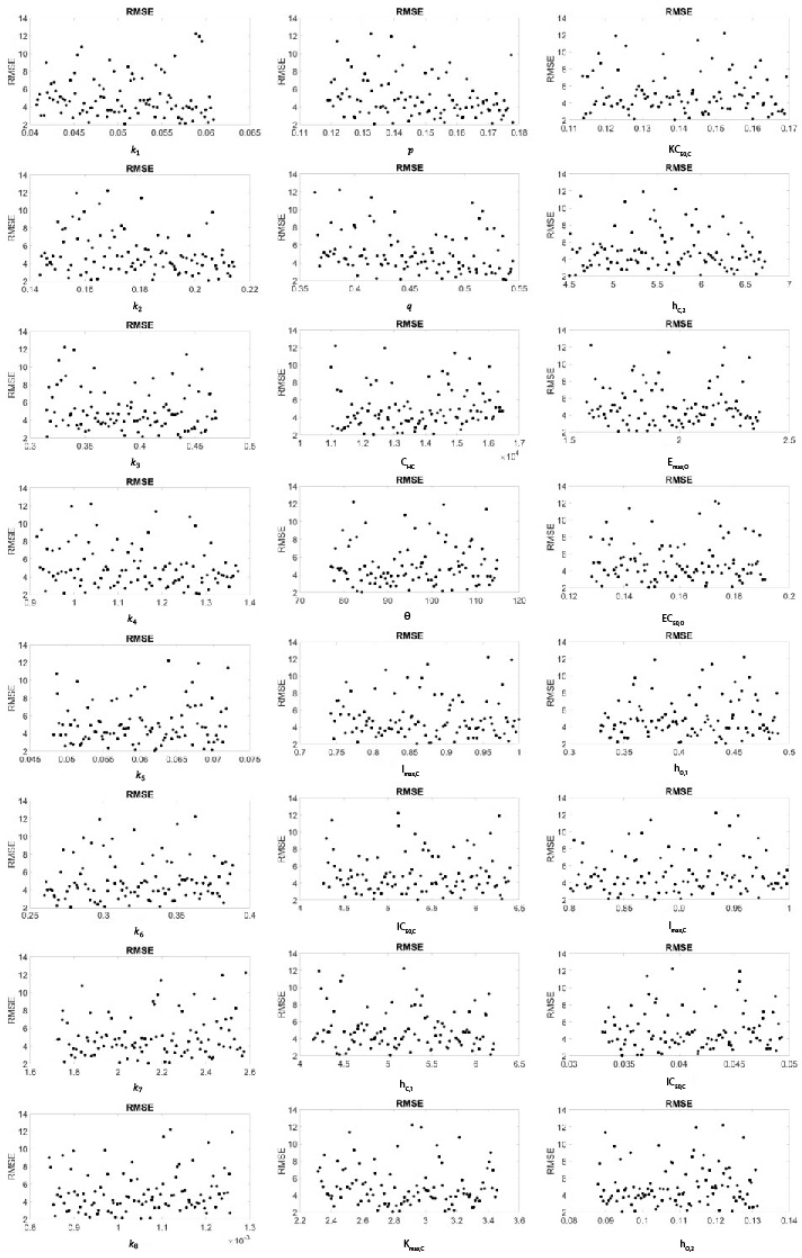

FIGURE A.6: **Latin hypercube analysis is a method to see how sensitive the model output is to global changes in parameter values.** The figure displays scatter-plots relating to the linear correlations between each parameter in its investigated range (horizontal axes) and the model output (vertical axes). Here, the model output is the RMSE of the cell confluency throughout the time-course of the simulation (equation 2.10) in response to 0.3 μM ceralasertib.

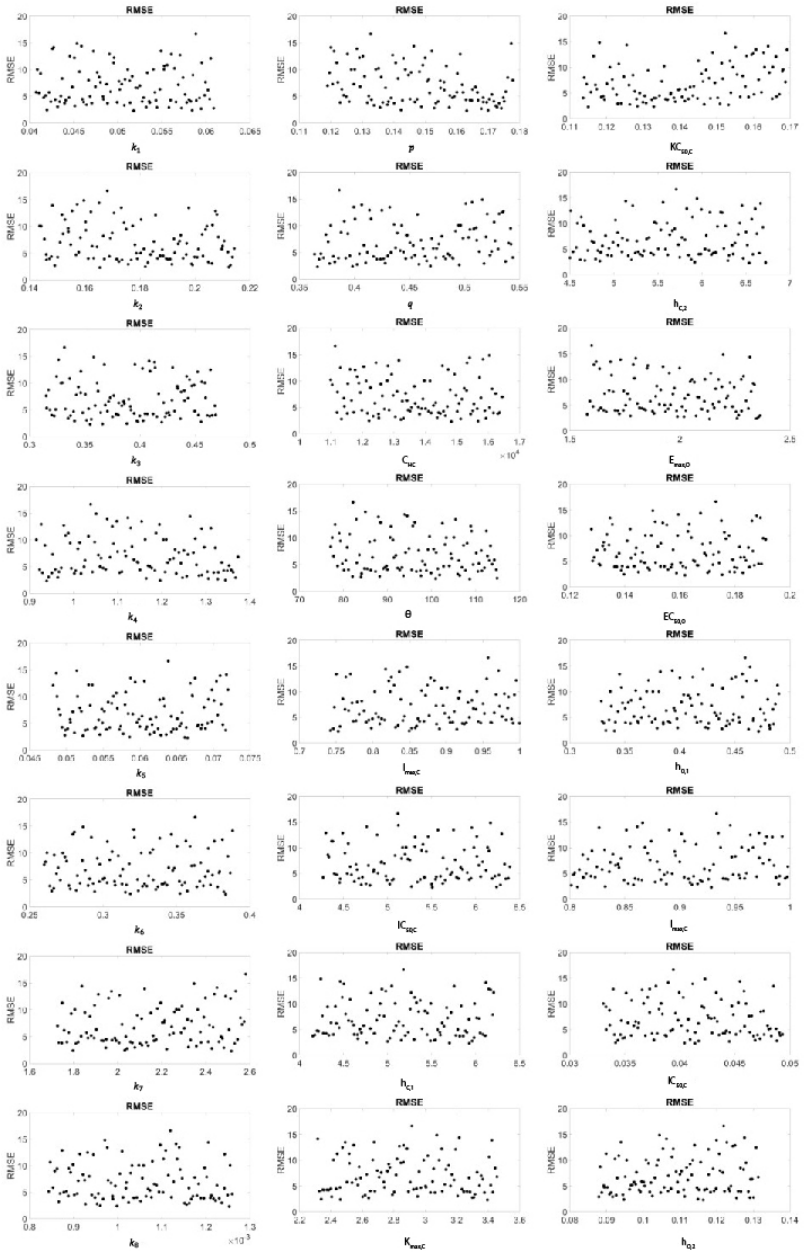

FIGURE A.7: **Latin hypercube analysis is a method to see how sensitive the model output is to global changes in parameter values.** The figure displays scatter-plots relating to the linear correlations between each parameter in its investigated range (horizontal axes) and the model output (vertical axes). Here, the model output is the RMSE of the cell confluency throughout the time-course of the simulation (equation 2.10) in response to 0.1 μM ceralasertib + 0.03 μM olaparib.

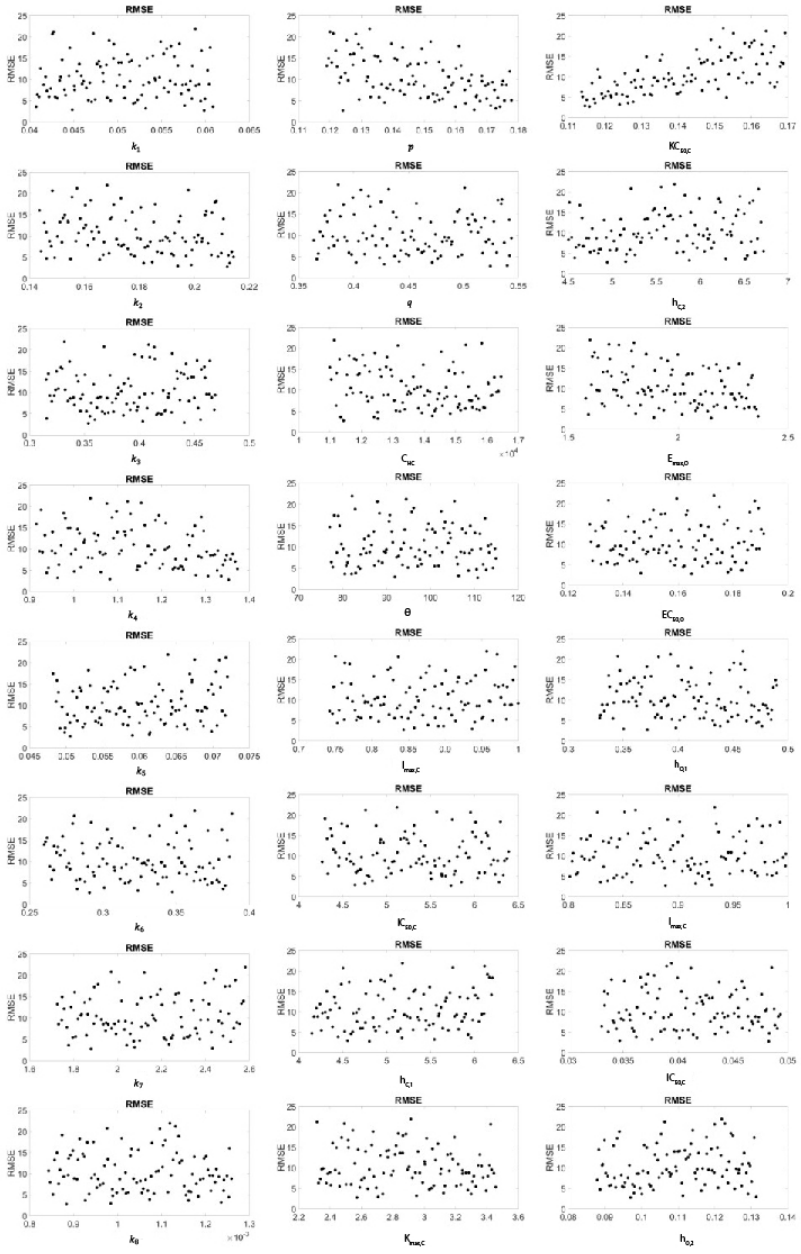

FIGURE A.8: **Latin hypercube analysis is a method to see how sensitive the model output is to global changes in parameter values.** The figure displays scatter-plots relating to the linear correlations between each parameter in its investigated range (horizontal axes) and the model output (vertical axes). Here, the model output is the RMSE of the cell confluency throughout the time-course of the simulation (equation 2.10) in response to 0.1 μM ceralasertib + 0.3 μM olaparib.

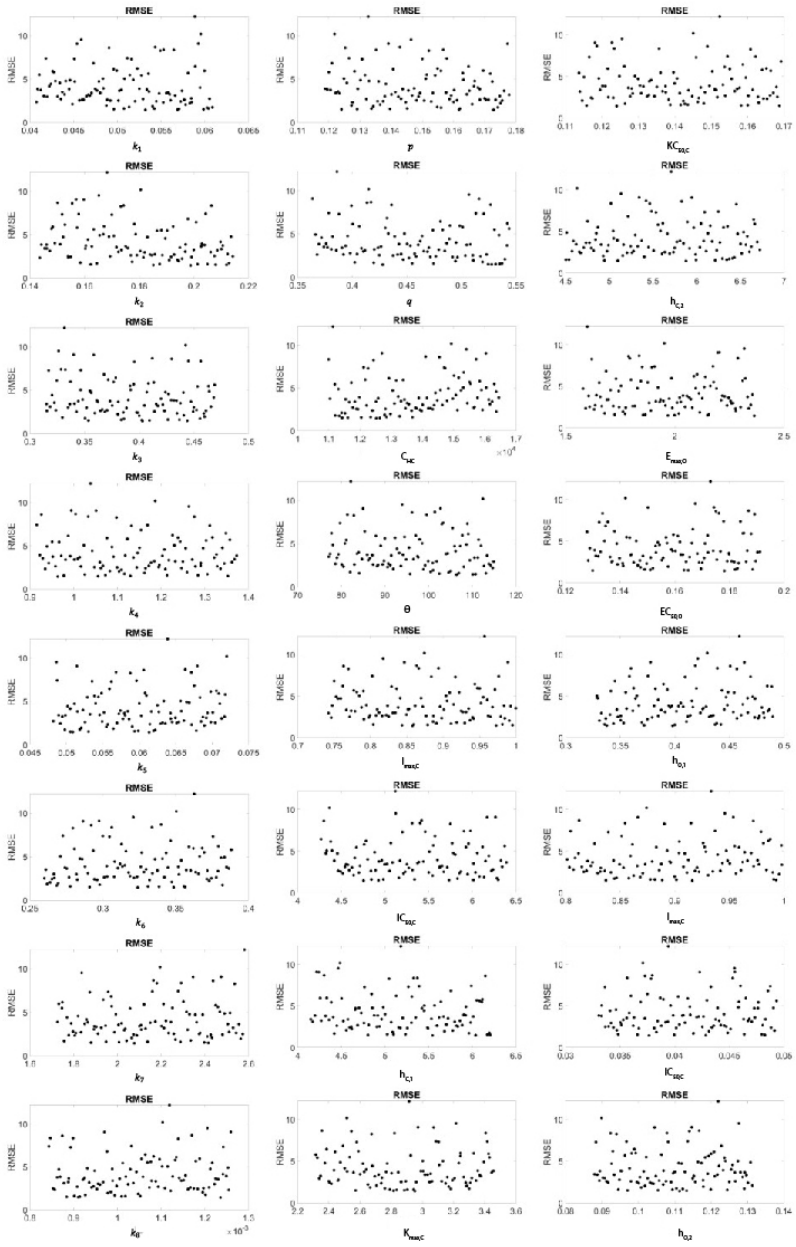

FIGURE A.9: **Latin hypercube analysis is a method to see how sensitive the model output is to global changes in parameter values.** The figure displays scatter-plots relating to the linear correlations between each parameter in its investigated range (horizontal axes) and the model output (vertical axes). Here, the model output is the RMSE of the cell confluency throughout the time-course of the simulation (equation 2.10) in response to 0.3 μM ceralasertib + 0.03 μM olaparib.

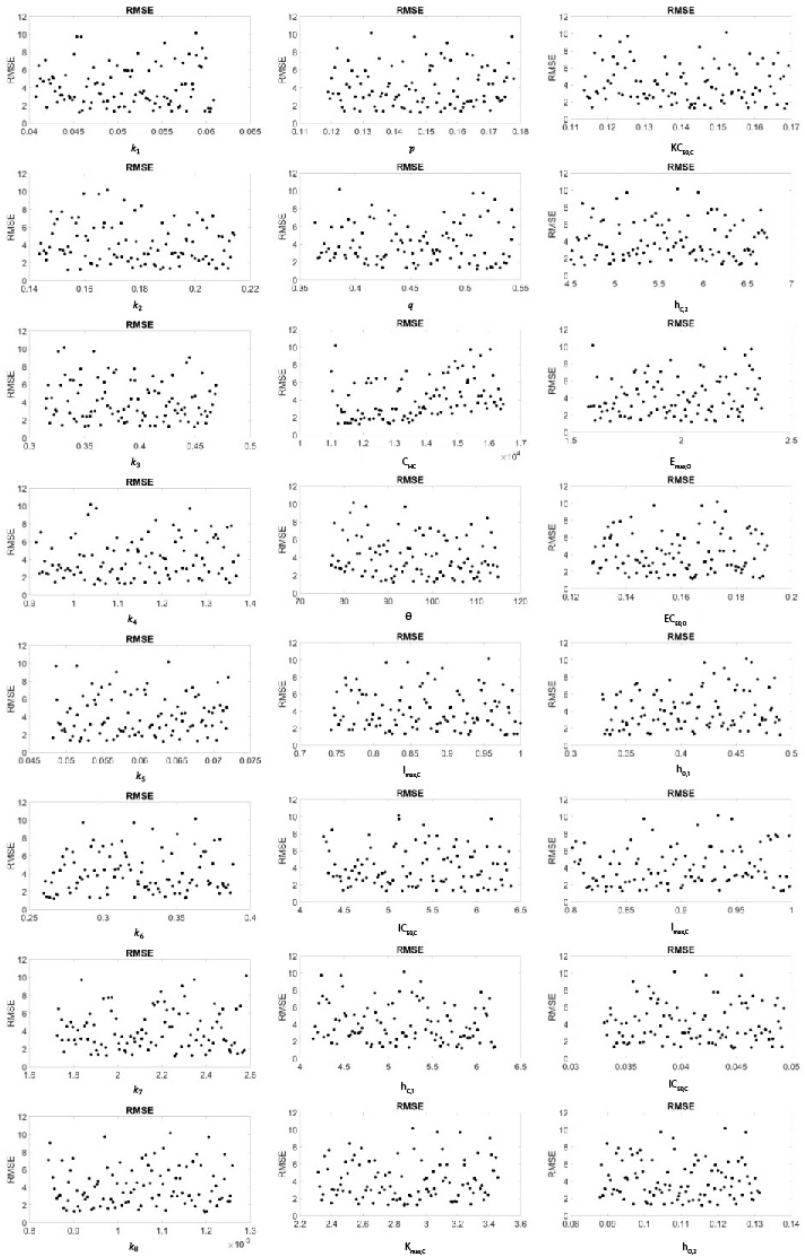

FIGURE A.10: **Latin hypercube analysis is a method to see how sensitive the model output is to global changes in parameter values.** The figure displays scatter-plots relating to the linear correlations between each parameter in its investigated range (horizontal axes) and the model output (vertical axes). Here, the model output is the RMSE of the cell confluency throughout the time-course of the simulation (equation 2.10) in response to 0.3 μM ceralasertib + 0.3 μM olaparib.

A.3 Appendix to Chapter 4

A.3.1 Model Selection

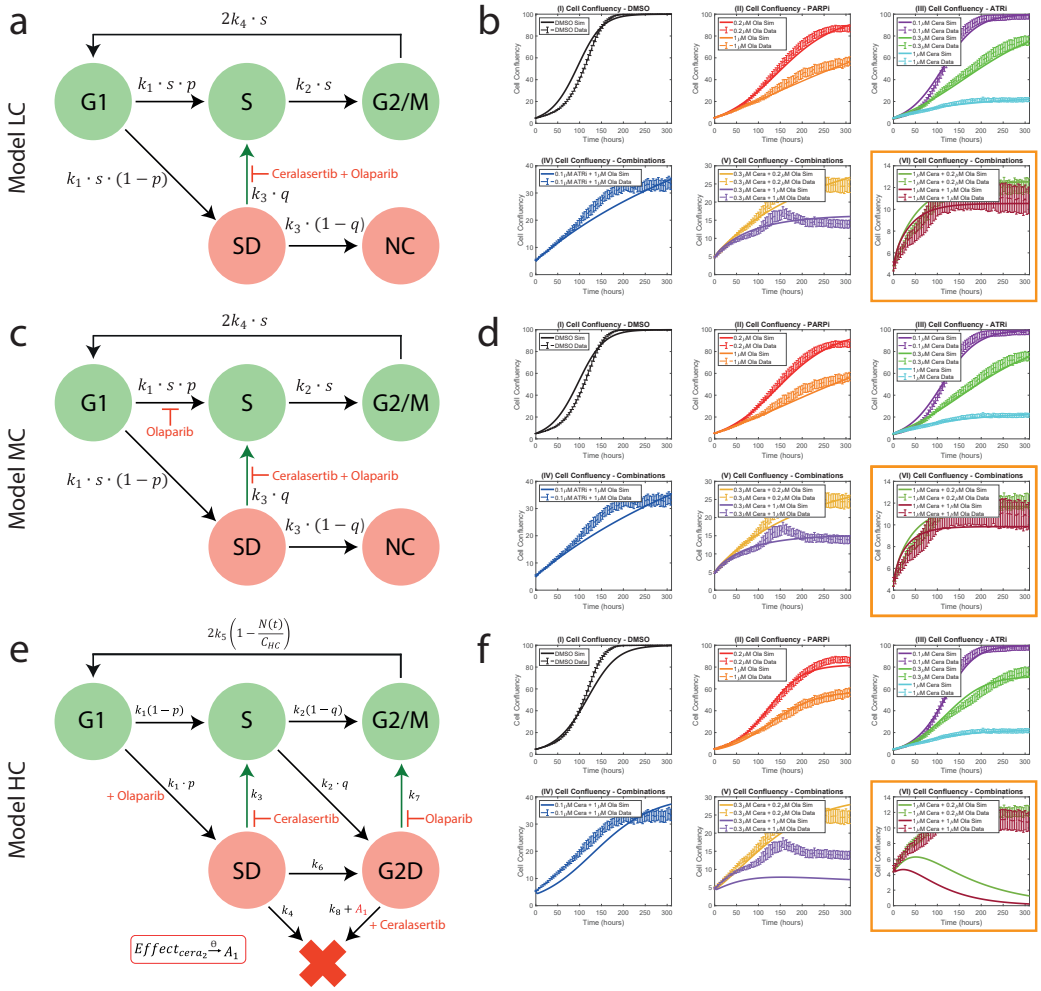

FIGURE A.11: **Three compartment models are parameterised and evaluated against in vitro data and are visually compared for the best model fit.** The plots show the schematic of the three compartment models: (a) Model LC, (c) Model MC, and (e) Model HC. The time and drug dependencies of the parameters in (a,c,e) have been omitted for ease of presentation. (b,d,f) The plots show simulated and experimental cell confluency over 310 hours for various dose combinations of ceralasertib and olaparib. Training data is used to estimate model parameters (plots I-V) and test data is used to evaluate the model (plot VI with the orange borders). The solid curves represent the simulation results from the three compartment models: (b) Model LC, (d) Model MC, and (f) Model HC. The dashed curves represent the mean in vitro data, with standard error of the mean for 3 experiments indicated with error bars.

We perform a data-driven model selection that motivates the choice of the model equations (Equations 4.1a-4.1e). We compare three compartment models: (1) a low complexity model (Model LC, Figure A.11 (a)), (2) a medium complexity model (Model MC, Figure A.11 (c)), and (3) a high complexity model (Model HC, Figure A.11 (e)). All models are described by a system of ODEs, where each dependent variable $[y]$ describes the concentration of cells in compartment y.

Low Complexity Model

Model LC (Figure A.11 (a)) is a modification of the model developed by Hamis et al. (2021). The compartments and parameters are the same as in Model MC, which is described in Chapter 4. In Model LC, we assume that both drugs act only on the path where cells transition from state SD to S. Therefore, the factor q, which represents the fraction of cells transitioning from state SD to S, decreases with increasing drug concentrations (see specifically Equation 4.6 in Section 4.2.1.2 for more details). To parameterise Model LC, we first directly read some model parameters ($U(0)$, C_{CM}, $G1_0$, S_0, SD_0, $G2/M_0$, k_1', k_2', k_4', q_0) from the in vitro data [113]. We thereafter estimate the remaining parameters (p_0, k_3', s, $E_{\text{max},1}$, $E_{50,1}$, h_1, $E_{\text{max},2}$, $E_{50,2}$, h_2) with the global optimiser GlobalSearch in MATLAB that minimises the sum of squares of the residuals between the model output and the in vitro data [175]. Model LC is described with the following system of ODEs:

$$\frac{d[G1](t)}{dt} = 2k_4\big(U(t)\big)s[G2/M](t) - k_1\big(U(t)\big)s[G1](t), \tag{A.2a}$$

$$\begin{aligned}\frac{d[S](t)}{dt} =& k_1\big(U(t)\big)sp[G1](t) - k_2\big(U(t)\big)s[S](t) \\ &+ k_3\big(U(t)\big)q([\text{drug}_{\text{Cera}}],[\text{drug}_{\text{Ola}}])[SD](t),\end{aligned} \tag{A.2b}$$

$$\frac{d[SD](t)}{dt} = k_1\big(U(t)\big)s(1-p)[G1](t) - k_3\big(U(t)\big)[SD](t), \tag{A.2c}$$

$$\frac{d[G2/M](t)}{dt} = k_2\big(U(t)\big)s[S](t) - k_4\big(U(t)\big)s[G2/M](t), \tag{A.2d}$$

$$\frac{d[NC](t)}{dt} = k_3\big(U(t)\big)\big(1 - q([\text{drug}_{\text{Cera}}], [\text{drug}_{\text{Ola}}])\big)[SD](t). \tag{A.2e}$$

In summary, including initial conditions, Model LC includes 10 parameters that are directly estimated from the data and 9 parameters that are obtained via a global optimiser in MATLAB.

Medium Complexity Model

Model MC (Figure A.11 (c)) is an expansion of Model LC and is described in Chapter 4, see especially Equations 4.1a-4.1e. See also Section 4.2.2 on how the model parameters are estimated. In summary, including initial conditions, Model MC includes 10 parameters that are directly estimated from the data and 9 parameters that are obtained via a global optimiser in MATLAB.

High Complexity Model

Model HC (Figure A.11 (e)) is an expansion of Model MC and is described in Chapter 2, see especially Equations 2.7a-2.7g. See also Section 2.2.2 on how the model parameters are estimated. In summary, including initial conditions, Model HC includes 6 parameters that are directly estimated from the data and 24 parameters that are obtained via a local optimiser in MATLAB.

Model Comparison

By visually comparing the cell confluency plots in Figure A.11 (b), (d), and (f), we observe that Model HC is overfitted to the experimental data due to the high number of parameters. Model HC is also unable to match the data for the combination 0.3 μM ceralasertib and 1 μM olaparib, most likely because a local optimiser is used to parameterise the model. We argue that both Model LC and Model MC are able to satisfactorily predict unseen time series data. The RMSE of Model LC and Model

MC are, in units of cell coverage percentages, 11.7931% and 11.4714% respectively. We also note that Model MC includes more biologically relevant drug effects of olaparib compared to Model LC. This is because Model MC includes both the SSB and DSB repair-inhibiting effects of olaparib (which was shown to be a prominent drug effect in Section 2.3.1), whereas Model LC only includes the latter effect. It is commonly believed that the main function of PARPi drugs is to inhibit the repair of SSBs which cause DSBs [35, 8]. Yet, the effect of PARP on DSB repair is heavily disputed. While some authors argue that PARP is involved in the repair of DSBs [28, 151], other authors argue that PARP is not involved in the repair of DSBs [135, 8]. Therefore, to safeguard our model, we argue that Model MC is the better model to study cell population dynamics in response to 0.1-1 μM ceralasertib doses and 0.2-1 μM olaparib doses.

A.4 Appendix to Chapter 6

A.4.1 Estimating the Value of v_B

In Chapter 6 the value of v_B represents the number of neighbourhoods in which daughter cells can be placed in the baseline ABM. The value is parameterised and evaluated against experimental data 2 (Section 1.3). In Figure A.12, we investigate multiple values of v_B and argue that $v_B = 3$ is able to capture the logistic trends in the cell confluency well.

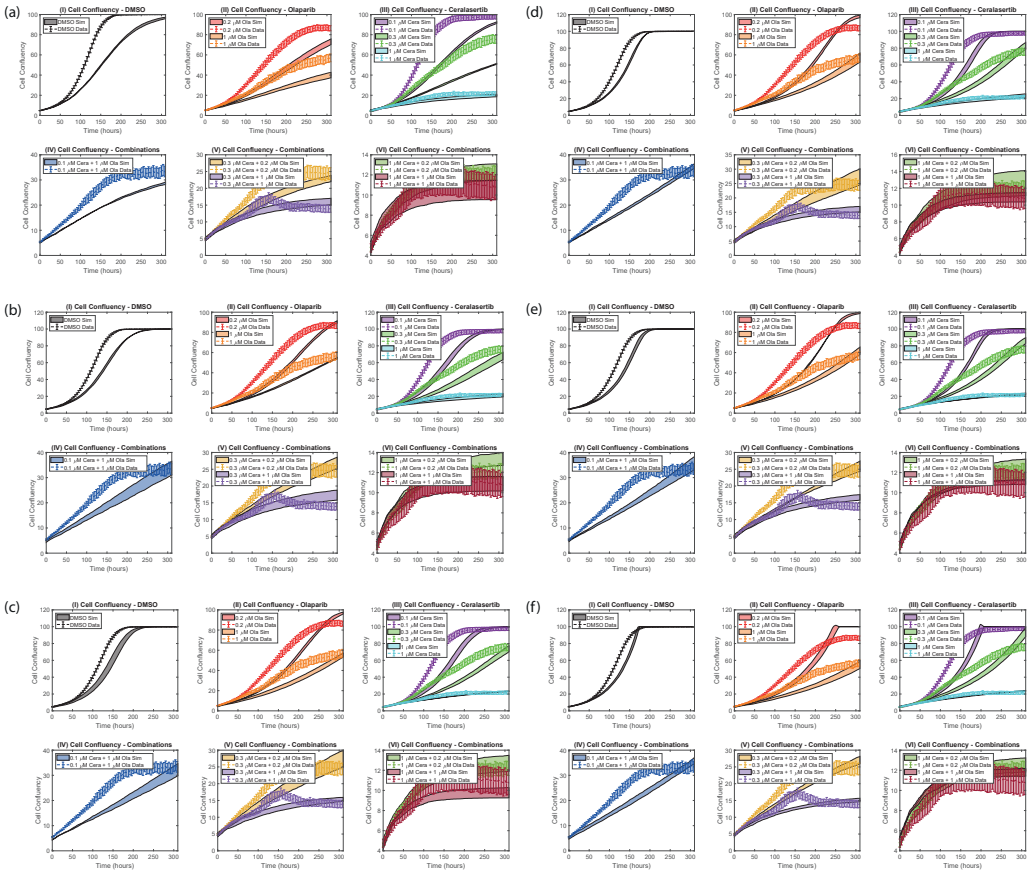

FIGURE A.12: **The parameter v_B, which denotes the neighbourhood order in which daughter cells can be placed in the ABM, is calibrated from experimental data 2.** The plots show simulated and experimental cell confluency over 310 hours for various dose combinations of ceralasertib and olaparib. Training data is used to estimate v_B (plots I-V) and test data is used to evaluate the model (plot VI). We test multiple values of v_B: (a) $v_B = 1$, (b) $v_B = 2$, (c) $v_B = 3$, (d) $v_B = 4$, (e) $v_B = 5$, and (f) $v_B = \infty$ The latter represents the case where cells can divide anywhere as long as it is within the lattice boundary. The solid curves represent the simulation results from the ABM. The dashed curves represent the mean in vitro data, with standard errors for 3 experiments indicated with error bars.

A.4.2 Multiscale Model: No-Flux Boundary Conditions

In Chapter 6, we calibrate our baseline ABM to in vitro data and assume that the boundary is a physical boundary because it represents a well plate used in the in vitro scenario. Hence, we parameterise the ABM with no-flux boundary conditions. However, when we study the spatial competition between drug-sensitive and drug-resistant cancer cells in the cell-crowding limited ABM, we ensure that the spatial

competition is an effect of the cell crowding and not the boundary by using periodic boundary conditions instead.

Figures A.13-A.17 summarise the results of the experiments described in Chapter 6 when using no-flux boundary conditions instead of periodic boundary conditions. By comparing Figures A.13-A.17 to Figures 6.5-6.10 we see that there is no significant difference in the results when using either periodic or no-flux boundary conditions.

A.4.2.1 The Spatial Structure of Cells Impacts Cell Population Responses

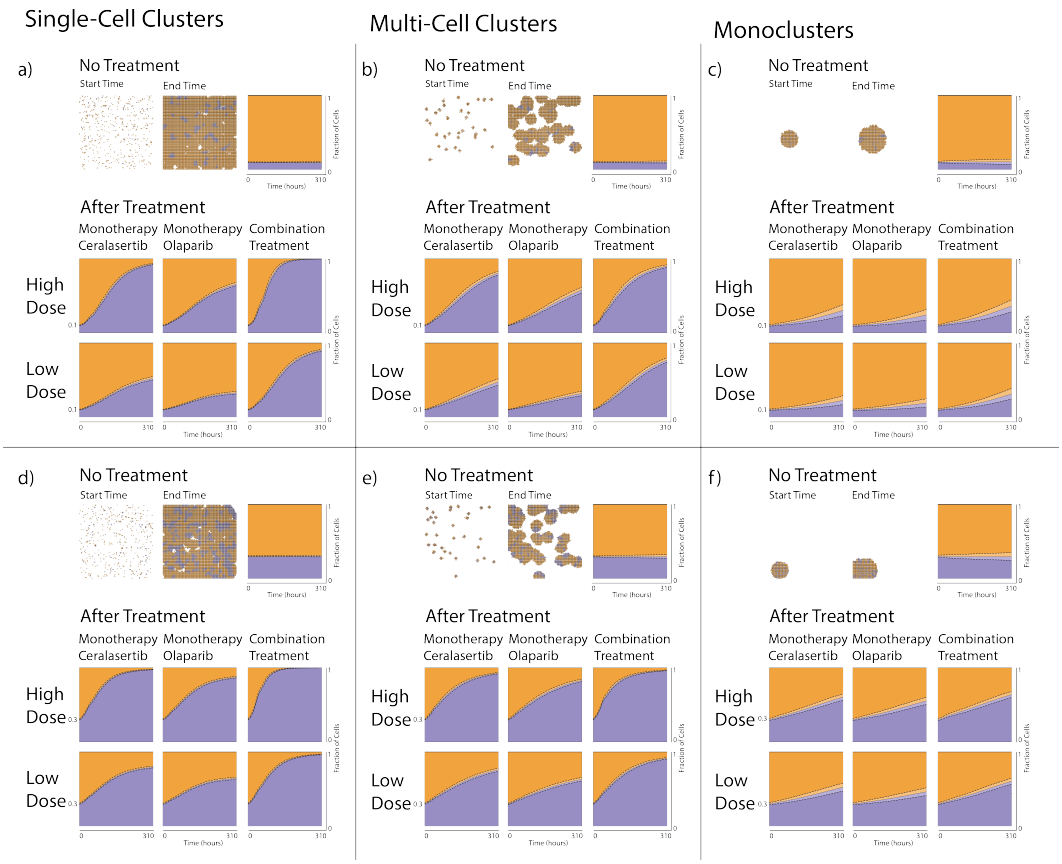

FIGURE A.13: **Cells that are resistant to an ATRi (ceralasertib) and a PARPi (olaparib) compete for spatial resources with drug-sensitive cells.** P_0 cells are randomly seeded on the lattice in single-cell clusters (a,d), multi-cell clusters (b,e), or monoclusters (c,f), with either $0.1P_0$ (a,b,c) or $0.3P_0$ (d,e,f) drug-resistant cells. Simulations are performed with no drugs (top row in each panel a-f), ceralasertib monotherapy (left column of the treatment section in each panel a-f), olaparib monotherapy (middle column of the treatment section in each panel a-f), and combination therapy (right column of the treatment section in each panel a-f) for high (middle row in each panel a-f) and low (bottom row in each panel a-f) doses. Examples of initial and final simulation snapshots are shown in each panel a-f with drug-sensitive (orange) and drug-resistant (purple) cells. Panels a-f also include plots of the dynamic mean fraction of drug-sensitive (orange) and drug-resistant (purple) cells, and standard deviations (dashed curves) from 100 simulation runs. These in silico experiments are performed with no-flux boundary conditions.

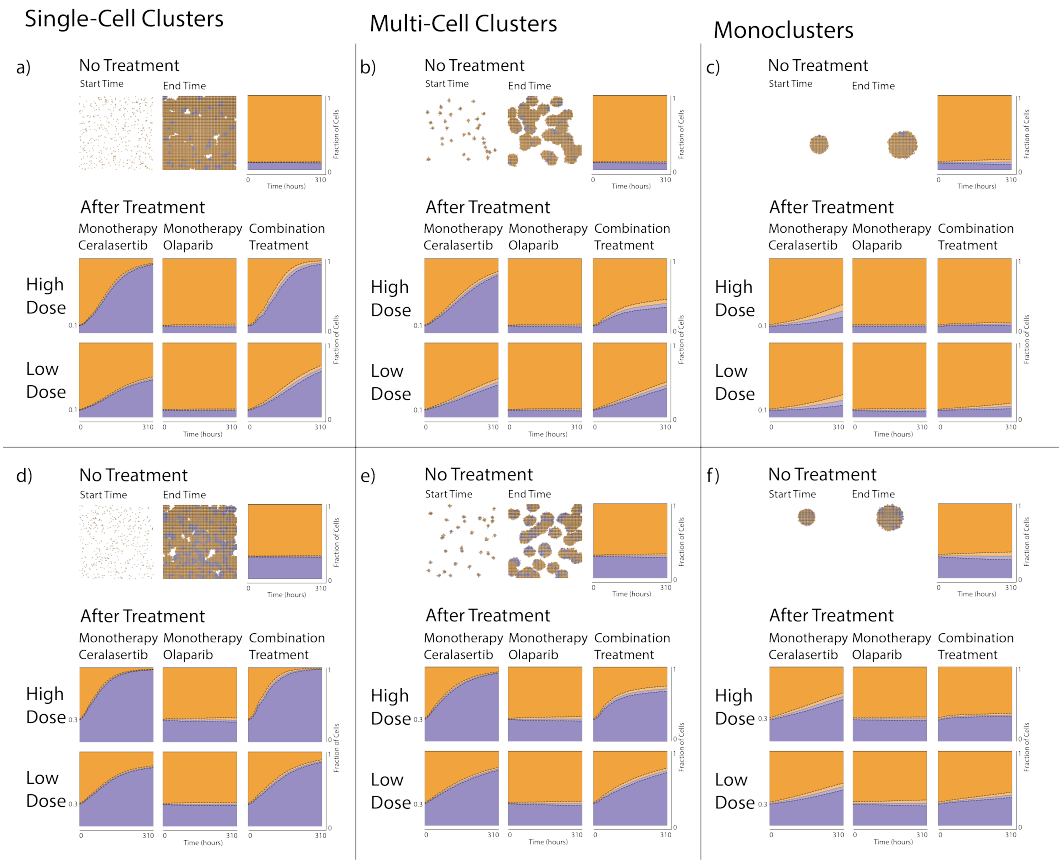

FIGURE A.14: **Cells that are resistant to an ATRi (ceralasertib) compete for spatial resources with drug-sensitive cells.** P_0 cells are randomly seeded on the lattice in single-cell clusters (a,d), multi-cell clusters (b,e), or monoclusters (c,f), with either $0.1P_0$ (a,b,c) or $0.3P_0$ (d,e,f) drug-resistant cells. Simulations are performed with no drugs (top row in each panel a-f), ceralasertib monotherapy (left column of the treatment section in each panel a-f), olaparib monotherapy (middle column of the treatment section in each panel a-f), and combination therapy (right column of the treatment section in each panel a-f) for high (middle row in each panel a-f) and low (bottom row in each panel a-f) doses. Examples of initial and final simulation snapshots are shown in each panel a-f with drug-sensitive (orange) and drug-resistant (purple) cells. Panels a-f also include plots of the dynamic mean fraction of drug-sensitive (orange) and drug-resistant (purple) cells, and standard deviations (dashed curves) from 100 simulation runs. These in silico experiments are performed with no-flux boundary conditions.

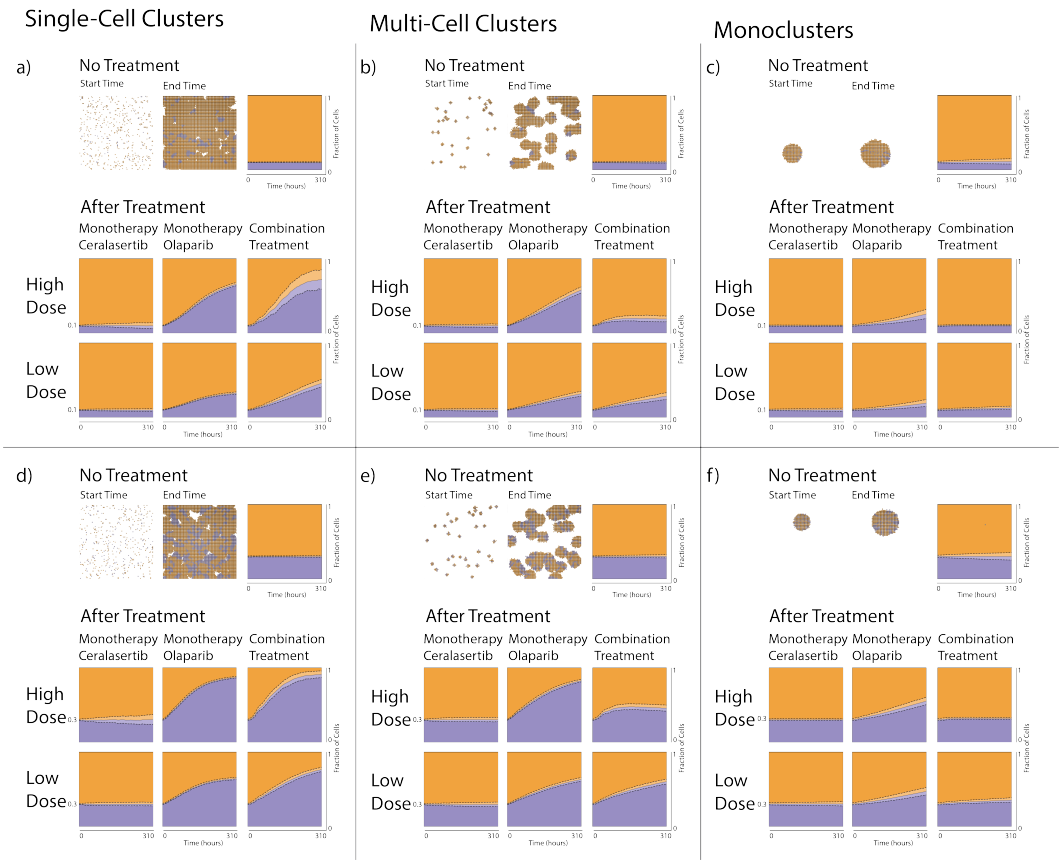

FIGURE A.15: **Cells that are resistant to a PARPi (olaparib) compete for spatial resources with drug-sensitive cells.** P_0 cells are randomly seeded on the lattice in single-cell clusters (a,d), multi-cell clusters (b,e), or monoclusters (c,f), with either $0.1P_0$ (a,b,c) or $0.3P_0$ (d,e,f) drug-resistant cells. Simulations are performed with no drugs (top row in each panel a-f), ceralasertib monotherapy (left column of the treatment section in each panel a-f), olaparib monotherapy (middle column of the treatment section in each panel a-f), and combination therapy (right column of the treatment section in each panel a-f) for high (middle row in each panel a-f) and low (bottom row in each panel a-f) doses. Examples of initial and final simulation snapshots are shown in each panel a-f with drug-sensitive (orange) and drug-resistant (purple) cells. Panels a-f also include plots of the dynamic mean fraction of drug-sensitive (orange) and drug-resistant (purple) cells, and standard deviations (dashed curves) from 100 simulation runs. These in silico experiments are performed with no-flux boundary conditions.

A.4.2.2 Spatial Competition and Drug Concentrations Impacts the Proliferation of Cancer Cell Subpopulations

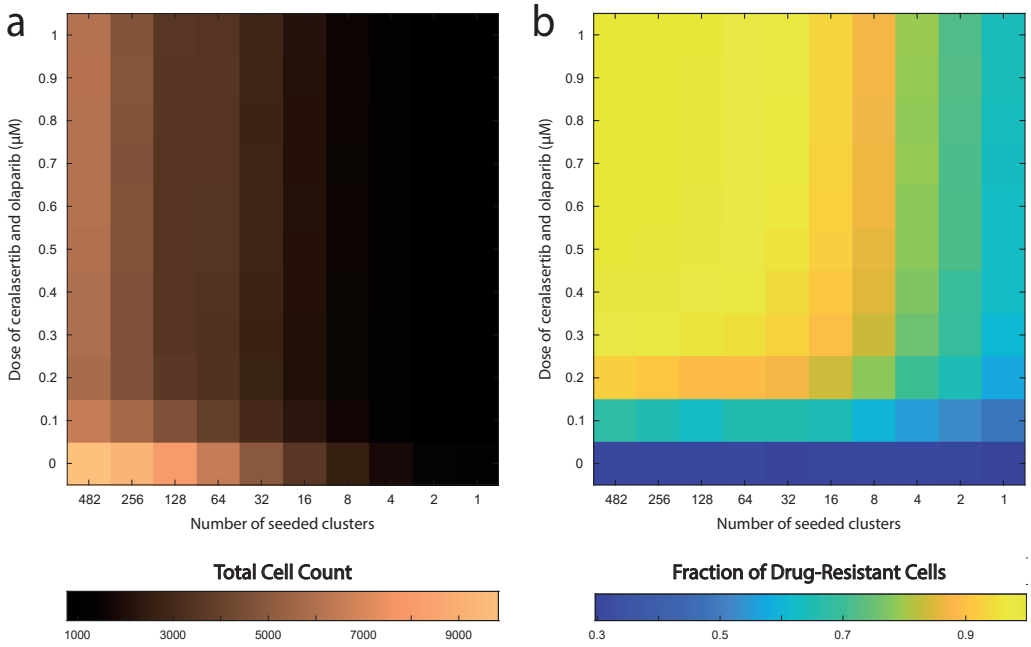

FIGURE A.16: **Drug doses and spatial cell configurations impact the dynamics of total cell counts and the composition between drug-sensitive and drug-resistant cells.** The heatmaps show results from in silico experiments in which drug-sensitive and drug-resistant cells coexist. At the start of the experiments, P_0 cells are seeded on the lattice, where $0.3P_0$ cells are resistant to both ceralasertib and olaparib. Two inputs are varied in the simulations: (1) the number of clusters in which cells are seeded (indicated by the horizontal heatmap axes), and (2) the combination treatment drug doses (indicated by the vertical heatmap axes). The results show (a) the total cell count and (b) the fraction of drug-resistant cells at the end of the simulations. Each heatmap bin shows the mean value of 100 simulation runs. These in silico experiments are performed with no-flux boundary conditions.

A.4.2.3 The Doubling Time of Drug-Resistant Cells Impacts Cell Population Dynamics

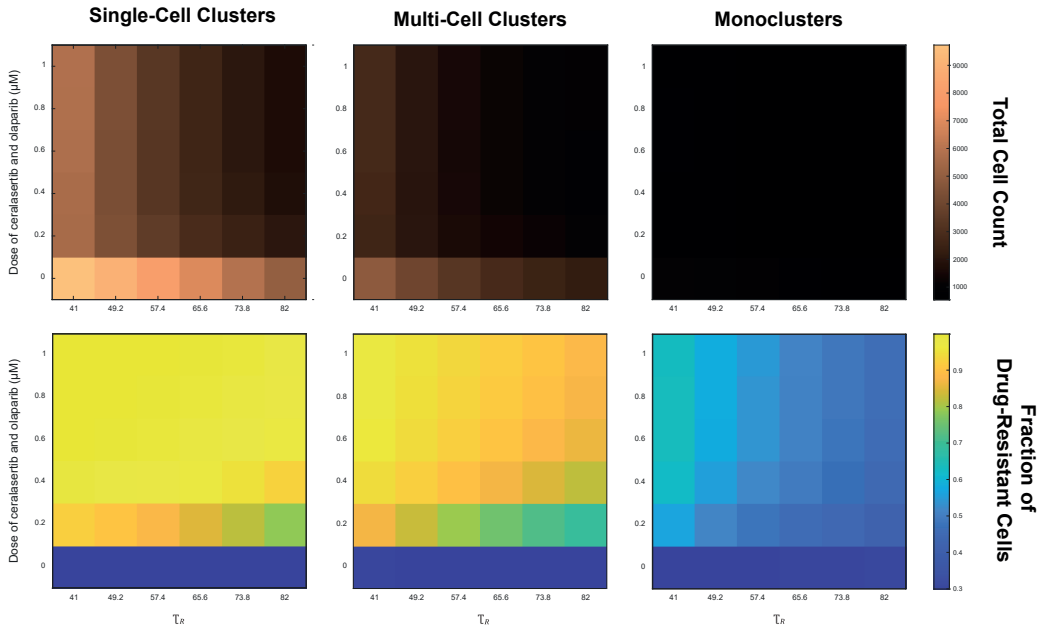

FIGURE A.17: **Spatial cell configurations, drug doses, and cell doubling times impact the dynamics of total cell counts and the composition between drug-sensitive and drug-resistant cells.** At the start of the experiments, P_0 cells are seeded on the lattice, where $0.3P_0$ cells are resistant to both ceralasertib and olaparib. Three inputs are varied in the simulations: (1) the seeded cluster configurations (left, middle, right panel), (2) the combination treatment drug doses (indicated by the vertical heatmap axes), and (3) the mean doubling time of the drug-resistant cells (indicated by the horizontal heatmap axes). The heatmaps show the total cell count (top panel) and the fraction of drug-resistant cells (bottom panel) at the end of the simulation. Each heatmap bin shows the mean value of 100 simulation runs. These in silico experiments are performed with no-flux boundary conditions.

A.4.3 Consistency Analysis

In this Section, we perform a consistency analysis on the ABM described in Chapter 6 that motivates the choice of running each in silico experiment 100 times to draw conclusions from the model. Figure A.18 show details of the $\hat{A}$-measures and the scaled $\hat{A}$-measures for all tested values of d. Note that Figure A.18 shows that smaller values of d result in a more irregular pattern in the scaled and initial $\hat{A}$-measure values. The $\hat{A}$-measure values become more consistent with a small statistical significance for values d=100 and 300. When $d = 100$, we can see that

the $\hat{A}$-measures are all between 0.44 and 0.56 (top figure in Figure A.18 (d)) and the scaled $\hat{A}$-measures below 0.56 (top figure in Figure A.18 (d)). This implies that $d = 100$ yields a small enough statistical difference, and 100 simulation runs per in silico will suffice for us to draw conclusions from the ABM.

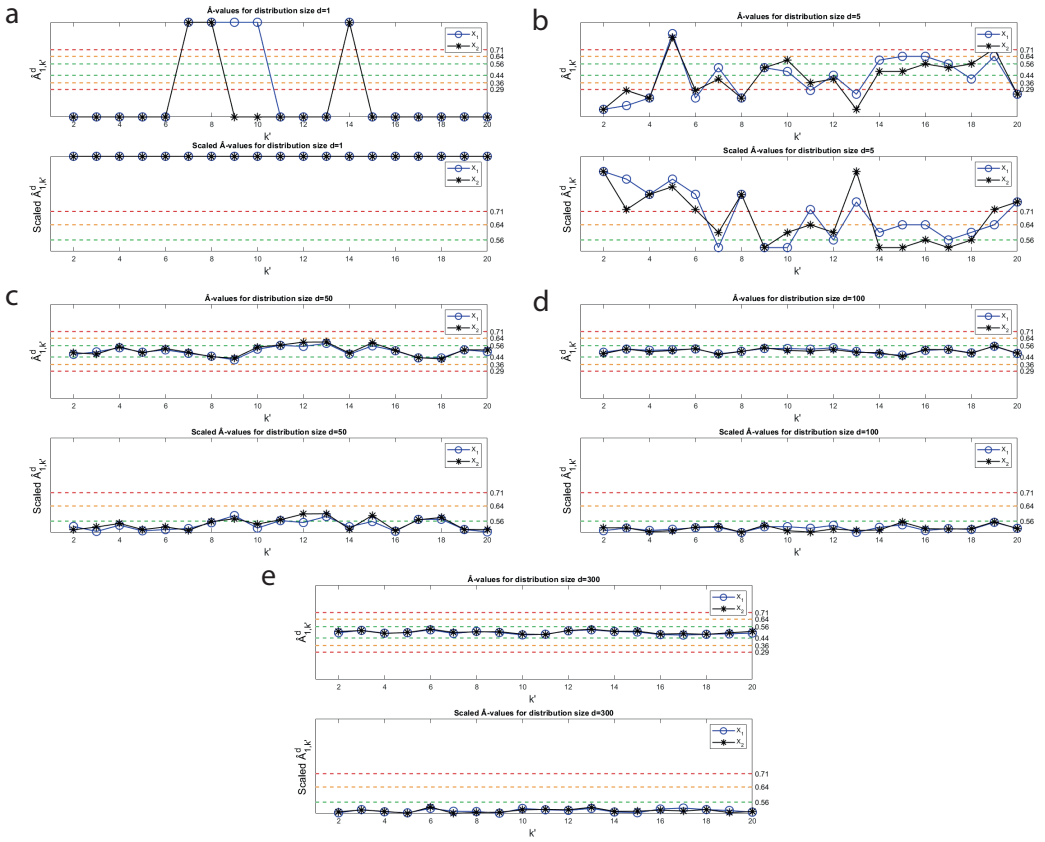

FIGURE A.18: **A consistency analysis is performed to decide how many in silico simulations are enough to draw conclusions from the ABM to mitigate any model uncertainty arising from intrinsic-model stochasticity.** Each figure displays the $\hat{A}$-measures (top) and the scaled $\hat{A}$-measures (bottom) for distribution sizes (a) $d = 1$, (b) $d = 5$, (c) $d = 50$, (d) $d = 100$, and (e) $d = 300$. X_1 represents the cell confluency halfway through the simulation and X_2 represents the cell confluency at the end of the simulation both with 0.3 μM ceralasertib and 0.2 μM olaparib.

A.4.4 Median, Standard Deviation, and Variance Heatmaps Relating to Section 6.3.2

In Chapter 6, we plot the mean values of (a) the total cell count and (b) the fraction of drug-resistant cells at the end of the simulations from 100 simulation runs (Figure

6.9). However, in Figures A.19-A.21, we also plot the median, standard deviation, and variance from the 100 simulation runs respectively.

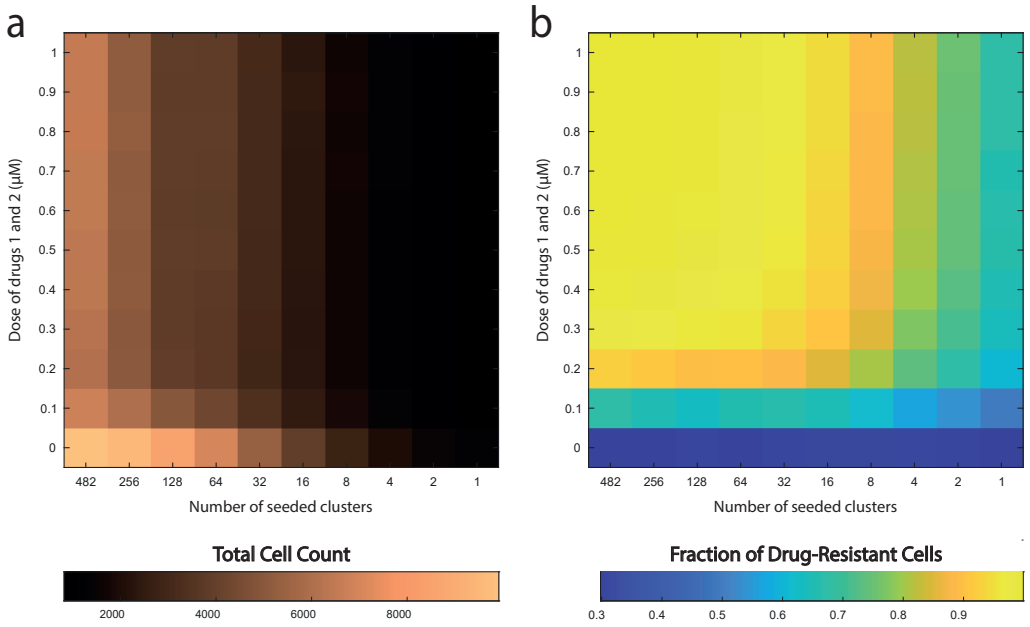

FIGURE A.19: **Drug doses and spatial cell configurations impact the dynamics of total cell counts and the composition between drug-sensitive and drug-resistant cells.** The heatmaps show results from in silico experiments in which drug-sensitive and drug-resistant cells coexist. At the start of the experiments, P_0 cells are seeded on the lattice, where $0.3P_0$ cells are resistant to both ceralasertib and olaparib. Two inputs are varied in the simulations: (1) the number of clusters in which cells are seeded (indicated by the horizontal heatmap axes), and (2) the combination treatment drug doses (indicated by the vertical heatmap axes). The results show (a) the total cell count and (b) the fraction of drug-resistant cells at the end of the simulations. Each heatmap bin shows the median value of 100 simulation runs.

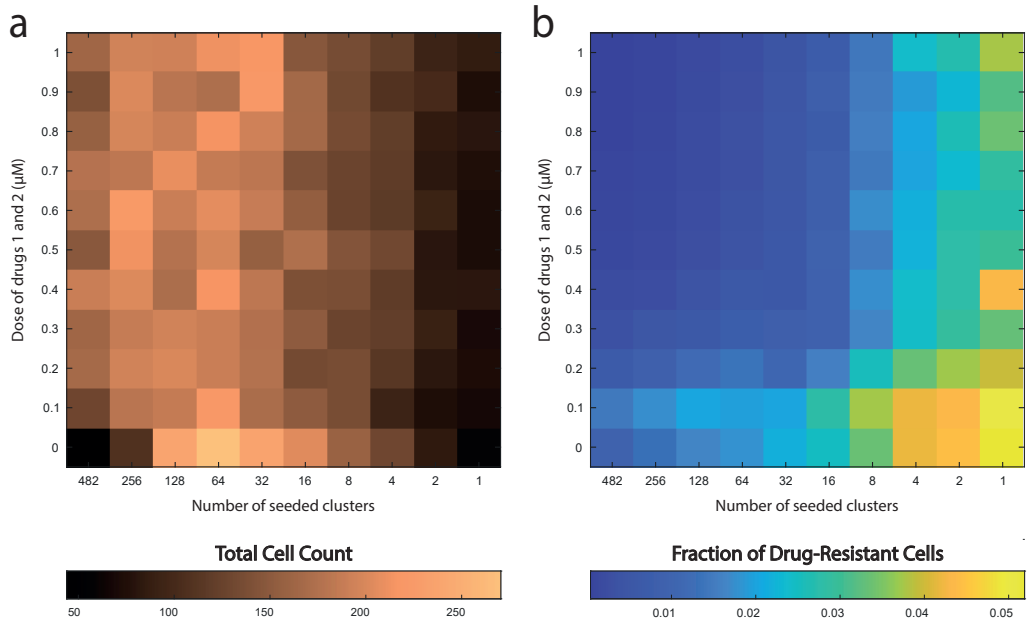

FIGURE A.20: **Drug doses and spatial cell configurations impact the dynamics of total cell counts and the composition between drug-sensitive and drug-resistant cells.** The heatmaps show results from in silico experiments in which drug-sensitive and drug-resistant cells coexist. At the start of the experiments, P_0 cells are seeded on the lattice, where $0.3P_0$ cells are resistant to both ceralasertib and olaparib. Two inputs are varied in the simulations: (1) the number of clusters in which cells are seeded (indicated by the horizontal heatmap axes), and (2) the combination treatment drug doses (indicated by the vertical heatmap axes). The results show (a) the total cell count and (b) the fraction of drug-resistant cells at the end of the simulations. Each heatmap bin shows the standard deviation value of 100 simulation runs.

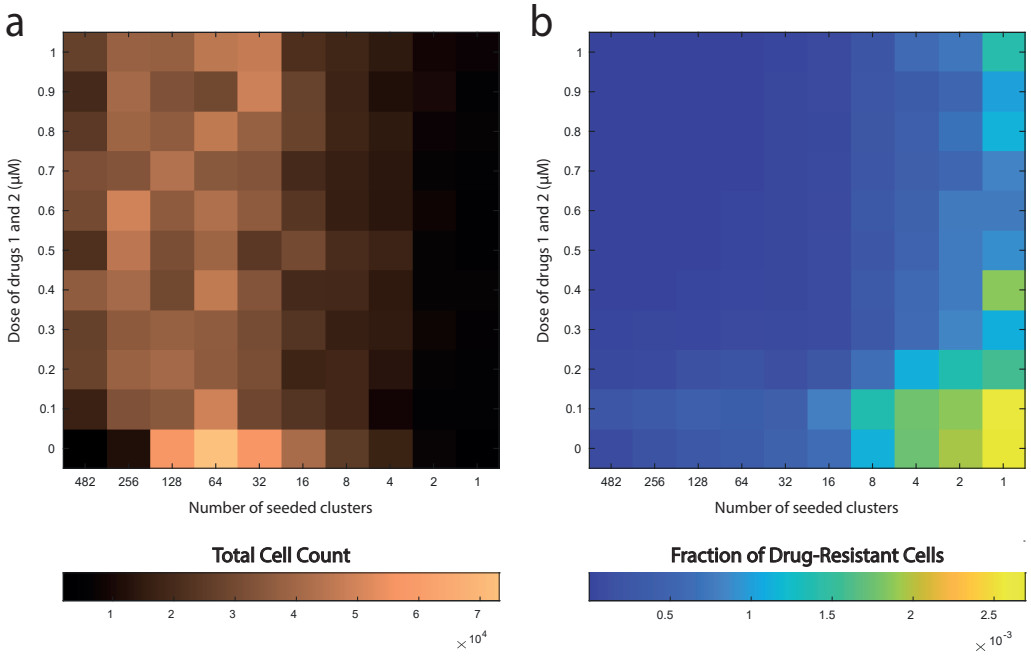

FIGURE A.21: **Drug doses and spatial cell configurations impact the dynamics of total cell counts and the composition between drug-sensitive and drug-resistant cells.** The heatmaps show results from in silico experiments in which drug-sensitive and drug-resistant cells coexist. At the start of the experiments, P_0 cells are seeded on the lattice, where $0.3P_0$ cells are resistant to both ceralasertib and olaparib. Two inputs are varied in the simulations: (1) the number of clusters in which cells are seeded (indicated by the horizontal heatmap axes), and (2) the combination treatment drug doses (indicated by the vertical heatmap axes). The results show (a) the total cell count and (b) the fraction of drug-resistant cells at the end of the simulations. Each heatmap bin shows the variance value of 100 simulation runs.